Towards a Universal Criterion for Predicting Vortex Breakdown in Swirling Jets

by

Aran Fitzgerald

A thesis submitted in fulfilment of the requirements for the
award of Master of Engineering Science of the
Department of Mechanical Engineering,
Monash University

May 2005

for Melissa

Statement of Originality

This thesis contains no material that has been accepted for the award of a degree or diploma in this or any other university. To the best of the candidate's knowledge and belief, this thesis contains no material previously published or written by another person except where due reference is made in the text of this thesis.

_____

Candidate: Aran J. Fitzgerald

12 May 2005

Abstract

Vortex breakdown in an unconfined laminar swirling jet is simulated using an in-house spectral-element code to numerically solve the incompressible, axisymmetric Navier-Stokes equations. The results show good agreement with the flow states observed in the equivalent experiments (e.g. Billant *et al.* , 1998).

The main focus of this study was to investigate the universality of the critical swirl ratio for predicting vortex breakdown in swirling jets. For conditions matched to the experimental conditions, the numerically predicted critical swirl ratios agreed to within $\pm 3\%$ of the experimentally determined values. The simulations demonstrated that the swirl ratio parameter (S) developed by Billant *et al.* (1998) did not universally describe the critical swirl ratio for different axial velocity profiles. A series of five different velocity profiles were devised, and their critical swirl ratios tested, giving a variation of 50%. Two modified formulations of the swirl ratio, using integrated parameters, were then tested and found to yield similarly large spreads of critical swirl ratios. An alternative swirl ratio (S_*) was then developed based on the conservative quantities of mass flow rate and angular momentum flow rate. The new swirl ratio parameter demonstrated greatly improved universality, resulting in a criterion for vortex breakdown of $S_* \geq 1.2$, with a maximum variation of $\pm 10\%$ over the range of Reynolds numbers tested.

The application of the new swirl ratio to the experimental velocity profiles of Farokhi *et al.* (1989) demonstrates that the new criterion may explains the difference in flow state observed by the authors. They show that two jets, with different azimuthal velocity profiles, give vortex breakdown in one case, but not in the other. Both jets were shown to have the same swirl ratio (as defined by Farokhi *et al.*, 1989). Recalculation of the swirl ratio using the new parameter gave $S_* = 1.37$ and $S_* = 1.27$, respectively, showing that the second jet may not be at a swirl ratio great enough for vortex breakdown.

Application of the swirl ratio S and the new swirl ratio S_* at a variety of downstream locations shows that the parameter S gives variable and decreasing swirl ratio with downstream distance, while the new swirl ratio remains constant.

The study also looks at the role of initial conditions in the state selection and meta-stability of the bubble and cone vortex breakdown types. This study shows that for impulsively initiated jets, the bubble-type dominates at low Reynolds numbers and the cone-type at high Reynolds numbers. The cone type is also observed at high swirl ratios in the low Reynolds number range. Further investigation described a bubble-type that is stable to finite perturbations well into the cone-type dominated region.

Acknowledgments

I would like to thank my supervisors: Kerry Hourigan and Mark Thompson, for guidance and inspiration, for supplying the computational code and technical support, and for their efforts in proof reading the manuscript multiple times; The Department of Mechanical Engineering for supplying the scholarship and the facilities; The Faculty of Engineering for providing the under-graduate computer laboratories as an after hours computing cluster, and especially Kenny Tan for setting this facility up.

I thank Justin Leontini, Karlis Atvars, Martin Griffith, Melissa Fitzgerald and Amanda Fitzgerald for each proof reading chapters of my thesis and for discussing the finer points of my research throughout the candidature. I thank Andreas Fouras for his useful advice. I would like to thank all my student colleagues for making everyday life enjoyable.

My deepest gratitude goes to Melissa for trusting and supporting this endeavor, for her friendship, guidance, criticism and love. I also thank my family for supporting me during the degree and to my parents for their efforts to understand what it is that I do.

Publications Relating to Thesis

Fitzgerald, A., Hourigan, K. & Thompson, M.C. 2005 Vortex breakdown state selection as a meta-stable process. *ANZIAM J.* **46**(E), C101–C104.

Fitzgerald, A., Hourigan, K. & Thompson, M.C. 2005 Towards a universal criterion for predicting vortex breakdown in swirling jets. *In proceedings of the 15*th *Australasian Fluid Mechanics Conference*, The University of Sydney, Sydney, Australia, December 2004.

Nomenclature

Symbol	Description
$\S$	Thesis section indicator
$\int$	Integral operator
∇	Vector gradient operator (grad)
∇^2	Del squared operator
$\sum$	Summation operator
α_q	Adams-Bashforth weighting factors of order q
β_q	Adams-Moulton weighting factors of order q
Γ	Computational boundary
θ	Azimuthal cylindrical-polar coordinate
ν	Kinematic viscosity
ξ	Real variable in the equation for the Gauss-lobatto-Legendre quadrature points
ρ	Fluid density
ω_θ	Azimuthal vorticity
Ω	Angular velocity
C	Constant used in momentum flux matching
H	Total head
J	Order of the time-stepping scheme
$\mathbf{L}(\mathbf{u})$	Linear terms of the Navier-Stokes equations

Symbol	Description
m	Order of the Legendre polynomial used in spatial discretisation
$\dot{m}$	Mass flow rate
$\dot{m}_e$	Mass flow rate for an equivalent velocity profile with constant velocity
$\dot{M}_\theta$	Angular momentum flux
$\dot{M}_{\theta e}$	Angular momentum flux for an equivalent velocity profile with constant velocity
Ma	Mach number
$\dot{M}_z$	Axial momentum flux
$\dot{M}_{ze}$	Axial momentum flux for an equivalent velocity profile with constant velocity
$\mathbf{n}$	Unit normal to the computational boundary Γ
n	total number of interpolation nodes per computational element
N	Axial velocity profile exponent
$\mathbf{N(u)}$	Non-linear terms of the Navier-Stokes Equations
p	Kinematic pressure P/ρ
P	Scalar pressure
P_m	Legendre polynomial of order m
P_0	Static pressure at the vortex centreline, located at $z = z_0$
P_1	Static pressure at the stagnation point on a vortex centreline, located at $z = z_1$
P_{ff}	Far field pressure

Symbol	Description
q	Order of the Adams-Bashforth and Adams-Moulton co-efficient
r	Radial cylindrical-polar coordinate
R	Nozzle radius
R_c	Vortex core radius
Re	Reynolds number
S	Swirl ratio as defined by Billant *et al.* (1998)
S_*	Swirl ratio based on $\bar{W}$ and $\bar{U}$
S_{*c}	Critical swirl ratio as measured using S_*
S_a	Swirl ratio based on W_0 and $\bar{U}$
S_{ac}	Critical swirl ratio as measured using S_a
S_c	Critical swirl ratio as measured using S
S_f	Swirl ratio defined in Farokhi *et al.* (1989)
S_i	Azimuthal velocity profile averaged swirl ratio as defined by Billant *et al.* (1998)
S_{ic}	Swirl ratio as measured using S_i
S_l	The swirl ratio S as applied locally
S_{*l}	The swirl ratio S_* as applied locally
t	Non-dimensional time units
$\mathbf{u}$	Vector notation for velocities U, V, W
$\hat{\mathbf{u}}$	First intermediate time-step velocity vector
$\hat{\hat{\mathbf{u}}}$	Second intermediate time-step velocity vector
U	Axial velocity
$\bar{U}$	Mass flow rate averaged axial velocity
U_0	Centreline axial velocity
$\overline{U_m}$	Axial momentum flux averaged axial velocity
V	Radial velocity

Symbol	Description
w_j	Weighting coefficients of the Gauss-Lobatto-Legendre quadrature
W	Azimuthal velocity
$\bar{W}$	Angular momentum flux averaged azimuthal velocity
W_0	Maximum azimuthal velocity
$\mathbf{x}$	Vector notation for dimensions z, r, θ
z	Axial cylindrical-polar coordinate

Contents

Chapter 1

Introduction

The first observation of the flow phenomenon dubbed *vortex breakdown* was recorded in 1957, in the vortical flow over a delta wing at high angle of attack (Althaus *et al.* , 1995). Since then, the identification and understanding of the mechanisms governing vortex breakdown have been the focus of continuous research efforts. Vortex breakdown can drastically affect the flow characteristics of a vortex core, and is generally characterised by the axial stagnation and reversal of the vortex core for a limited axial extent. Several forms of vortex breakdown have been identified in a variety of different vortex flows; including the bubble, the spiral and the cone. This chapter describes the flows in which vortex breakdown occurs, and gives a description of the various forms of vortex breakdown.

1.1   Flows Exhibiting Vortex Breakdown

The initial impetus for studying vortex breakdown came mainly from the aerodynamic characteristics of vortex breakdown in high angle of attack flight. Many military aircraft are designed to continue controlled flight in

1

a post-aerofoil-stall scenario (angle of attack $\gtrsim 15°$). Flight in this regime depends on the strong, slender vortex that is created by a delta wing to generate the majority of the lift. The slender vortex results from the shedding of vorticity from the under surface of the wing into a vortex that sits on the upper surface of the wing; providing the low pressure needed for lift (see figure 1.1 a). This vortex was found to experience vortex breakdown above a critical angle of attack that is related to the sweep-back angle of the wing (Althaus *et al.* , 1995). The resulting unsteady flow state causes loss and fluctuation of lift, due to the destruction of the coherent vortex. Additionally, the resulting turbulent wake of a vortex breakdown state has caused flutter and subsequent damage of control surfaces (e.g. Özgören *et al.* , 2002).

Figure 1.1 (b) shows an example of a leading edge vortex created by the highly swept leading edge root extension of an F/A-18 fighter jet. Here, the flow is visualised with smoke. The slender vortex core extends from the leading edge back to the trailing edge of the wing, where it experiences a rapid expansion in a roughly axisymmetric bubble. In this example, significant flutter would be experienced on the vertical stabiliser.

The early observations identified two states of vortex breakdown, dubbed *bubble* and *spiral*, due to their strong axisymmetric and asymmetric breakdown regions, respectively. These two states were also observed to co-exist at the same parameters in some flow scenarios. Figure 1.2 (a) shows a delta wing in plan view with flow from left to right, the two leading edge vortices extend downstream until breakdown occurs. The co-existence of vortex states is evident here with a bubble in the lower vortex and a spiral in the upper vortex. Figure 1.2 (b) shows turbulent vortex breakdown over a delta wing. Observations of the dynamics of vortex breakdown in delta wing applications demonstrates that the breakdown location moves upstream with
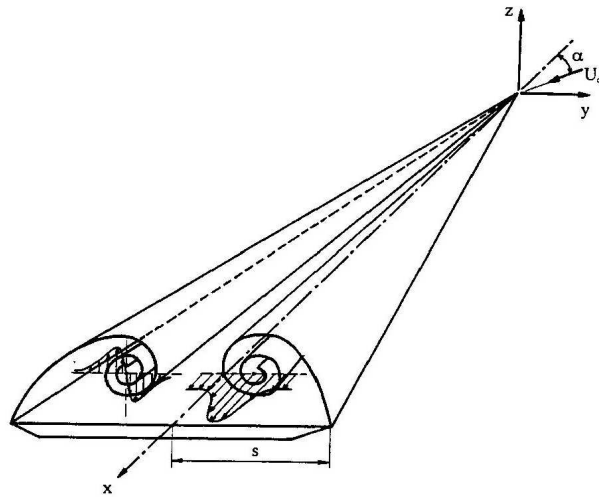
(a) Reproduced from Menke & Gursul (1997)

(b) Reproduced from Mitchell & Délery (2001)

Figure 1.1: A schematic representation of the roll-up of vorticity from the underside of a delta wing (a); and the leading edge vortex of a F/A-18 fighter jet at a high angle of attack regime, as visualised with smoke. Note that the turbulent wake of the near conical vortex breakdown impinges on the vertical stabiliser (b).

increasing angle of attack and with decreasing sweep back angle (Althaus *et al.* , 1995).

Civil aviation can also benefit from the understanding and control of vortex breakdown. Wing-tip vortices are a limiting factor in take-off timing at major airports. These vortices are observed in the wakes of all aircraft, but are especially strong for large, heavy-laden aircraft. The vortices can be present for several minutes after an aircraft has departed or landed. During this time, they pose a significant hazard to other aircraft in the vicinity. Figure 1.3 shows a landing aircraft with its wing-tip vortex being observed in the smoke from a nearby chimney. If vortex breakdown can be induced in these vortices, then the spacing between aircraft departures and landings can be decreased (Mager, 1972).

Another application for vortex breakdown is in the combustion field, where flame holding, stability, propagation and reactant mixing can be aided by ensuring that vortex breakdown persists in the combustion flow (Umemura & Tomita, 2001). Flame holding and stability is enhanced because the re-circulation region allows burning gasses to recirculate upstream where they can ignite the upstream fuel. Propagation and reactant mixing can be en-hanced by the high shear rates (folding and stretching) of fluid elements by a breakdown region. Furthermore, vortex breakdown can initiate turbulence in a flow allowing greatly increased mixing.

1.2 The Main Vortex Breakdown Types

The two main types of vortex breakdown observed in most experiments are the bubble and the spiral type. This section gives a description of the main characteristics of each type. Other types, such as the cone are discussed
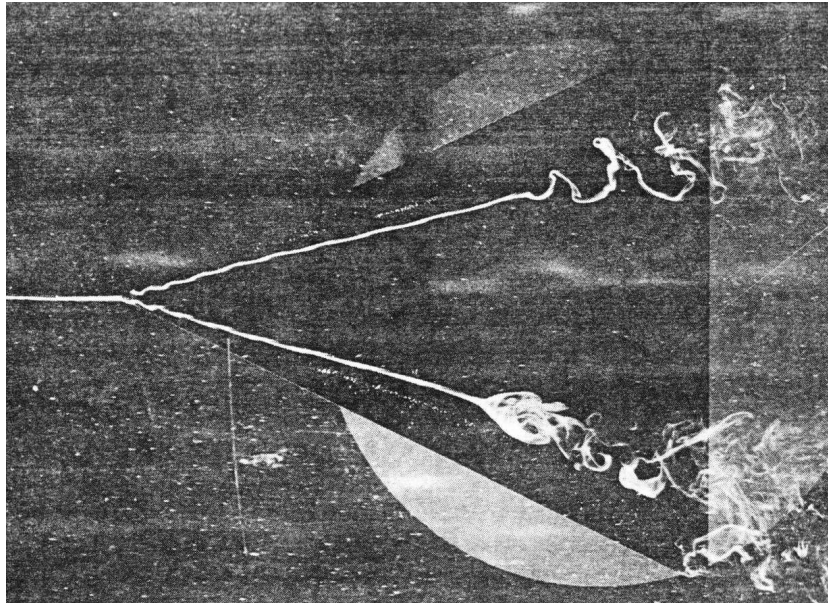
(a) Reproduced from Hall (1972)
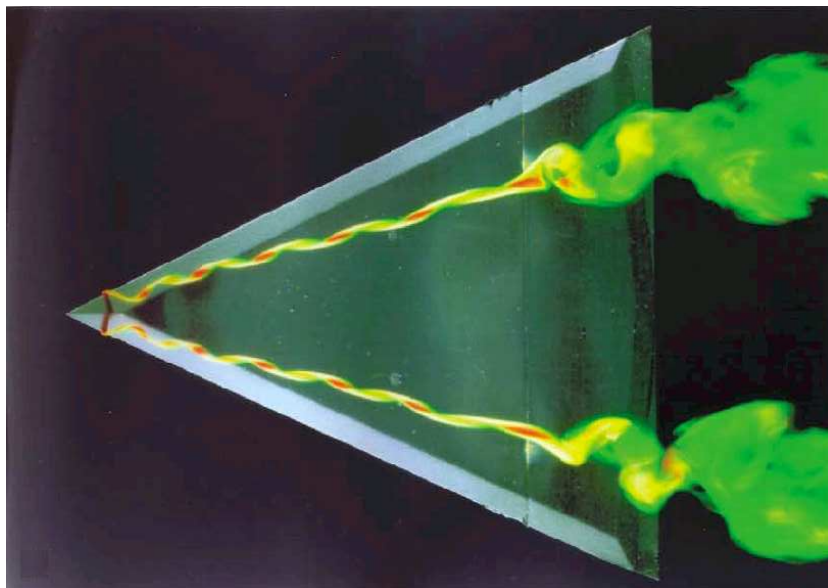
(b) Reproduced from Mitchell & Délery (2001)

Figure 1.2: Co-existence of the bubble and spiral states of vortex breakdown over a delta wing (a); and turbulent vortex breakdown at the trailing edge of a delta wing (b).

Figure 1.3: One of a pair of strong wing-tip vortices observed in chimney smoke after a landing aircraft passes. Source unknown.

briefly in §1.3.2 and §1.3.3.

1.2.1 The Bubble

The bubble type is generally characterised by an axisymmetric expansion of the vortex around a stagnation point that forms on the vortex centreline. This expansion usually has a limited axial extent, after which the vortex converges once again back toward the vortex centreline, to re-form a weaker vortical structure (Faler & Leibovich, 1977). The new vortex has been seen to subsequently undergo spiral vortex breakdown. Figure 1.4 shows the formation of the bubble type in a pipe, as visualised with fluorescein dye and a diametric light sheet. As seen here, the vortex breakdown bubble starts as a widening of the vortex core downstream (near the far right of the $t = 0s$ image). With subsequent images, a stagnation point appears then grows into a recirculation region that moves upstream to an approximate steady state location. In the final image, the internal dynamics of the bubble are evident, as is the spiralling of the wake of the breakdown. Figure 1.4 (b) shows a schematic of the internal dynamics of the observed structure in (a). Figure 1.5 (a) shows an iso-surface of constant pressure of a numerically simulated bubble with a spiral wake structure. The internal structure of the bubble

type was identified by Leibovich (1978) as having dual recirculation rings (see figure 1.5 b).

1.2.2 The Spiral

The spiral type is generally characterised by a kink in the vortex core away from the axis, followed by a spiralling of the vortex around the axis. Generally, the vortex will not reform a columnar vortex in its wake, instead it is dissipated into turbulence. The spiral rotation has been observed to be co-rotating (Sarpkaya, 1971) and counter-rotating relative to the original vortex (delta wings, e.g. Leibovich, 1984). Figure 1.6 (a) shows a schematic representation of a spiral breakdown. Note that despite the strong spiralling of the vortex core, a particle that is released on the centreline at *point A* traces an irrotational path around the spiral enclosure, probably due to the low circulation at the centreline. Figure 1.6 (b) shows the internal dynamics of a spiral vortex breakdown. The internal dynamics show a stagnation point that is offset from and precesses around the centreline. Apart from the absence of steady vortex rings, the internal dynamics are similar with those of the bubble, leading many to believe that the spiral breakdown is a bubble breakdown that is experiencing strong asymmetric perturbation. The spiral form of breakdown shows bi-stable characteristics with switching between the bubble and the spiral occurring without changing the flow parameters (Faler & Leibovich, 1977). This bi-stability is probably representative of the role of the amplification of perturbations in a complex feed-back mechanism.

(a)
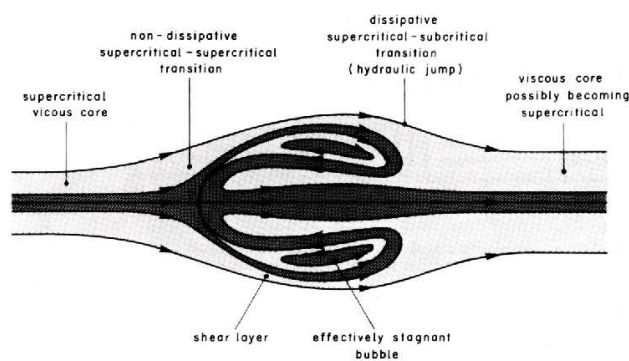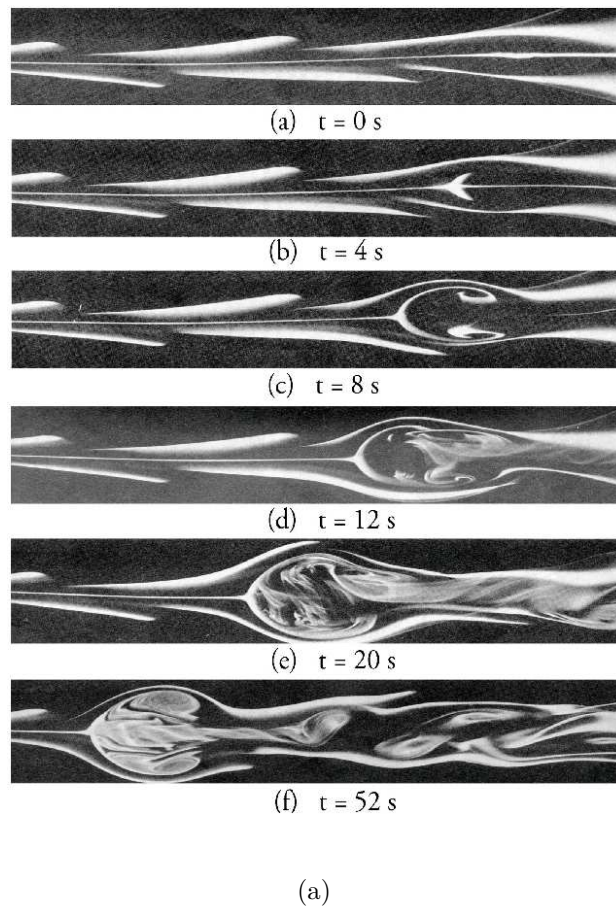
(b)

Figure 1.4: The formation of a bubble vortex breakdown in a pipe as visualised with fluorescein dye and a diametric light sheet (a). A schematic representation of the internal dynamics of the bubble recirculation region (b). Reproduced from Lucca-negro & O'Doherty (2001).
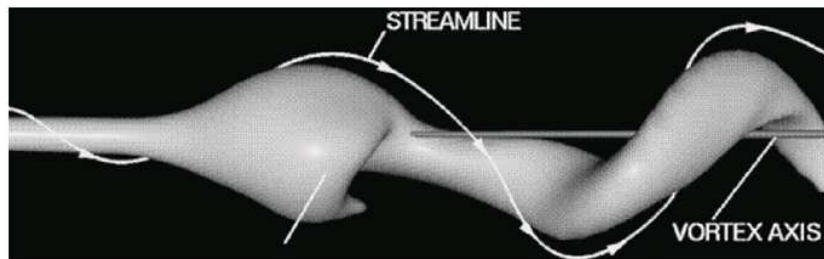
(a) Reproduced from Lucca-negro & O'Doherty (2001)
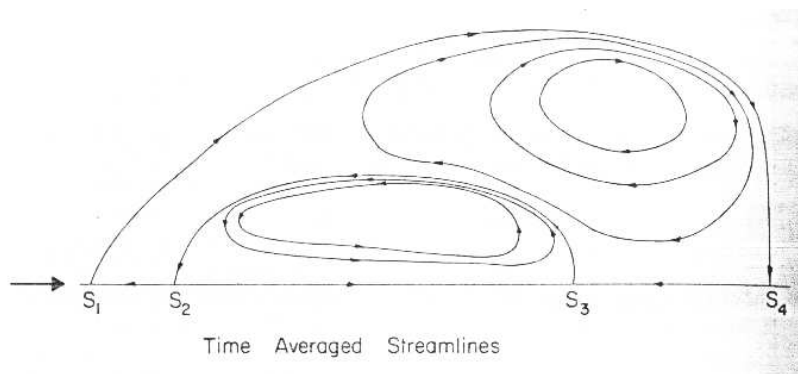
(b) Reproduced from Leibovich (1978)

Figure 1.5: Pressure iso-surface of a bubble with a spiral wake structure (a); and the internal dynamics of a bubble (b).
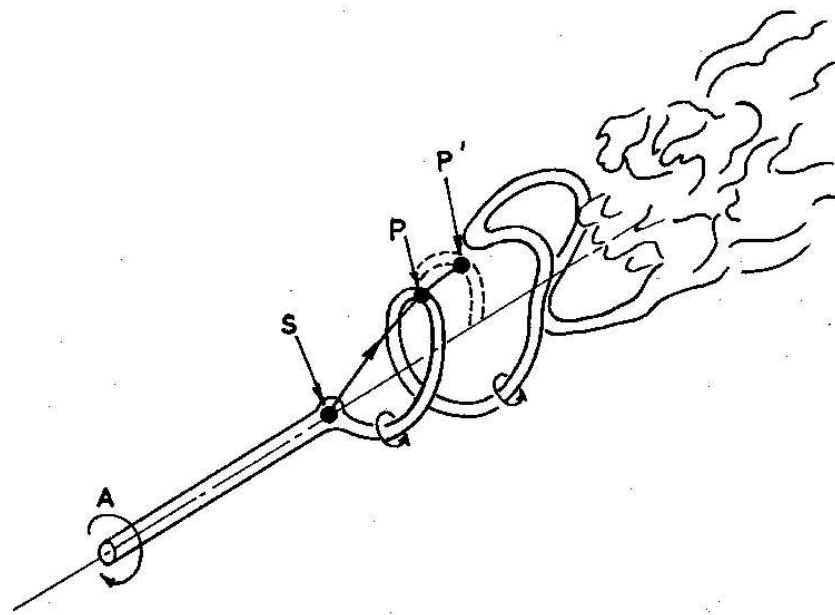
(a)
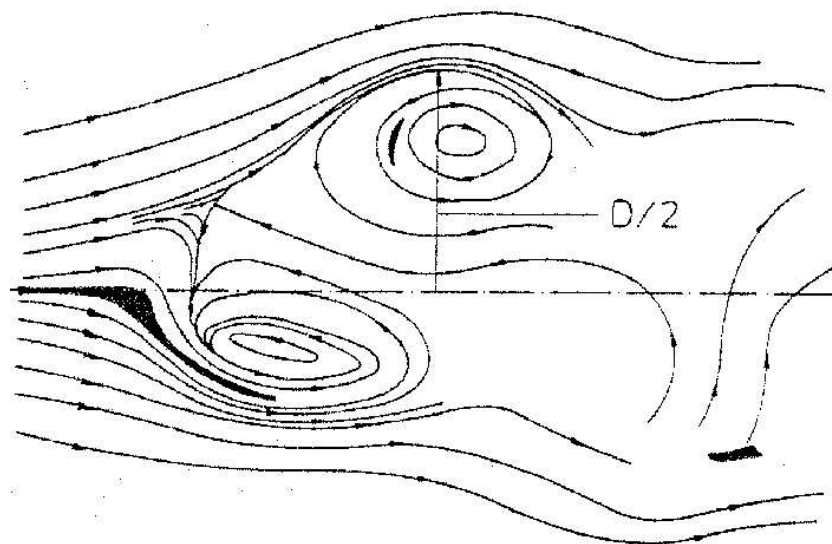
(b)

Figure 1.6: A schematic representation of a spiral breakdown including a particle trace A-S-P-P' (a); and the internal dynamics of a spiral vortex breakdown. Reproduced from Lucca-negro & O'Doherty (2001).

1.3 Other Flows Producing Vortex Breakdown

Vortex breakdown is observed in a variety of swirling flows, apart from flows over delta wings. An introduction to vortex breakdown in pipe flows, cylinders with rotating end-walls and unconfined jets, is presented. The flow in pipes generally shows similar vortex breakdown to those in delta wing flows, however cylinders with rotating end-walls and swirling jets have also shown different forms, including the cone vortex breakdown type.

1.3.1 Pipe Flows

Vortex breakdown in pipe flows was studied from an early stage (Sarpkaya, 1971; Hall, 1972) as the pipe geometry allowed a more controlled experiment than possible in delta wing geometries. The pipe flows generally used some form of vane to impart an azimuthal component on the flow and could therefore have independent control of both the axial and azimuthal velocities. The swirling flow is then redirected into a divergent pipe which serves the purpose of stopping the vortex breakdown from attaching to the inlet and supplying the adverse pressure present on the suction side of a delta wing. Diverging pipe flows show vortex breakdown of similar nature to those found over delta wings with both the bubble and spiral forms being well documented. The main difference between delta wing and pipe flow vortex breakdown is the rotational sense of the spiral type. Examples of vortex breakdown in pipes are given in figure 1.4.

1.3.2 Cylinders with Rotating End-Walls

Cylinders with a rotating end-wall were discovered to include a region of stagnation and recirculation on the centreline (Escudier, 1984). The rotat-

ing end-wall creates a primary circumferential rotation inside the cylinder, but also a secondary recirculation develops in the diametric plane. The combined flow demonstrates a vortical core of relatively high swirl level proceeding from the non-rotating end-wall down to the rotating end-wall. With sufficient rotational speed of the end-wall, vortex breakdown has been seen to occur in this vortex. Depending on the ratio of height to radius, a series of vortex breakdown bubbles are possible. Figure 1.7 shows dye visualisation in the diametric plane of a twin-bubble vortex breakdown scenario within a cylinder with a rotating end-wall (the lower wall). The vortex breakdown experienced in such an apparatus is reasonably symmetric and varies smoothly with increasing swirl, leading some to deny it as being a vortex breakdown state (see §2.2.1).

Figure 1.7: Fluorescein dye visualisations of a diametrical plane through a closed cylinder flow displaying dual recirculation bubbles. Reproduced from Sotiropolous *et al.* (2002).
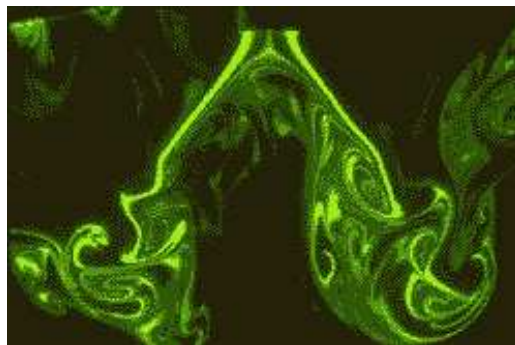
Figure 1.8: Fluorescein dye visualisations of a diametrical plane through a cone vortex breakdown. Reproduced from Billant *et al.* (1998).

1.3.3   Unconfined Jets

Unconfined jets offer a vortex breakdown scenario slightly different to those of the delta wing and the pipe flow. The absence of co-flow that is present in these flows, and the absence of a confining wall, allow the observation of a novel form of vortex breakdown only recently observed, the cone-type (Billant *et al.* , 1998). The cone represents a vortex breakdown state where the presence of the stagnation point causes a permanent expansion of the vortex core away from the centreline. The resulting conical shear layer usually thins and rolls due to shear layer instability. The cone vortex breakdown may find a useful application in wing-tip vortices for its ability to quickly dissipate a vortex core. Figure 1.8 shows a dye visualisation of a cone vortex breakdown. Here, the nozzle producing the swirling jet is located at the top of the image. The vortex quickly stagnates and expands conically. A bubble and spiral form of vortex breakdown, similar to those previously described, can also be observed in swirling jets.

Chapter 2

Literature Review

Early efforts toward determining the mechanism of vortex breakdown had some success in describing the behaviour of a vortex core, however, those based on analogies are limited in their ability to describe all the behaviour observed in experiments. Hence, more recent research is being directed into observations of a variety of simplified Navier-Stokes equations, and hydrodynamic instability as being able to provide more universal explanations for the behaviour of vortex breakdown. Despite the decades of effort, the exact mechanism of vortex breakdown has yet to be identified.

Without a mechanism, there is an increased importance in studies that identify the main controlling parameters and those that aim to predict breakdown. Other reviews of the research in the field of vortex breakdown have been completed by Hall (1966), Leibovich (1978), Althaus *et al.* (1995), Shtern & Hussain (1999) and Lucca-negro & O'Doherty (2001). More limited reviews can be found in Rösner (1995), Krause (1995) and Spall *et al.* (1987).

This chapter reviews vortex breakdown research, beginning with the initial research directed towards the mechanism of vortex breakdown, followed

by observations of the dynamics, numerical simulation and vortex breakdown control.

2.1   Theoretical Interpretations

There are three major theoretical approaches to explaining the mechanism of vortex breakdown: the analogy with hydraulic jump, the analogy with two dimensional flow separation, and hydrodynamic instability.

2.1.1   The Analogy with Hydraulic Jump

Benjamin (1962) and Benjamin (1967) proposed an axisymmetric mechanism for vortex breakdown that is analogous to two-dimensional hydraulic jump. The analogy leads to a definition of vortex breakdown as an energy dissipative structure, necessitated by a discontinuity between conjugate flow states. Benjamin bases the theory on the experimental observations of Harvey (1962), where axisymmetric undulations of the vortex were a precursor to vortex breakdown. These undulations were recognised by Benjamin as being similar to those seen in flows preceding hydraulic jump. Harvey's experiments were conducted under strict control of the main parameters, leading to a near-axisymmetric form of vortex breakdown at breakdown inception. Benjamin concluded that the near-axisymmetric breakdown form was due to minimisation of asymmetric disturbances.

Hydraulic jump is generally a larger dissipative structure involving a significant energy change between upstream and downstream, usually causing the growth and superposition of the standing waves to the point where they become turbulent. Benjamin relates this state to a vortex breakdown state with a turbulent wake region as seen in most vortex breakdown experienced

in flows over delta wings (Leibovich, 1978). Benjamin concludes that the main mechanism for vortex breakdown is steady and axisymmetric. Sarpkaya (1971) agrees with this hypothesis citing the similarities seen between the axial movement of vortex breakdown and the axial movement of hydraulic jump with changes to flow conditions.

The hypothesis formed by Benjamin (1962) is that there is a jump in the downstream flow force (the integral of the axial momentum flux plus pressure across the domain) when the vortex proceeds from a supercritical flow state upstream, to its conjugate sub-critical flow downstream. The excess downstream flow force is accounted for by the creation of standing waves in the downstream section. The process represented with the balance equation $S_1 = S_2 - R$, where S_1 and S_2 are the upstream and downstream flow forces, respectively, and R is the wave resistance. Benjamin proceeded to derive a criticality condition based on wave velocities upon idealised vortex cores with constant head and circulation over a stream-surface.

Support for Benjamin's theory included the more rigorous proof that the conjugate state of a supercritical flow can support waves of small amplitude (see Fränkel, 1967), while Randall & Leibovich (1973) extended a model of weakly non-linear waves beyond formal validity and observed flow characteristics and breakdown locations similar to those observed by Sarpkaya (1971). Maxworthy (1988) analysed and discussed three forms of waves that can be supported on vortex cores; the varicose, helicoidal and fluted forms, representing axisymmetric swelling, bending and wrinkling respectively. The varicose and helicoidal are found to propagate along the vortex core, and in the non-linear range, are known to exhibit solitary wave characteristics (as originally proposed by Benjamin, 1962). Maxworthy proposes that it is these waves that dominate vortex core behaviour and that the complexities
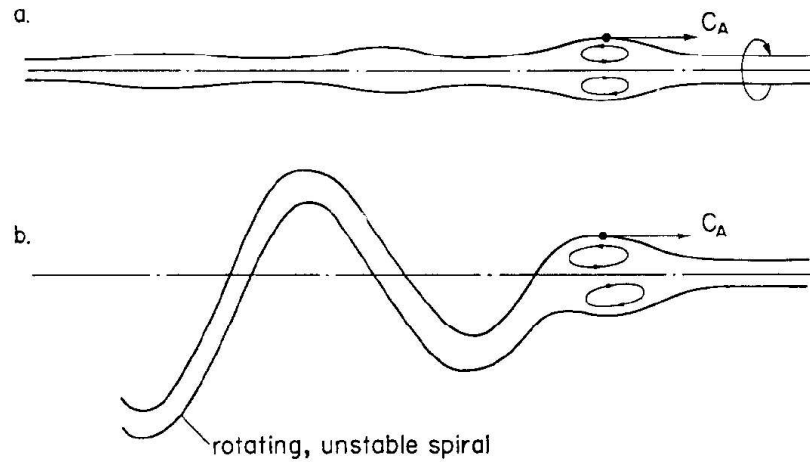
Figure 2.1: A pictorial representation of the formation of vortex breakdown due to the formation of large amplitude axisymmetric "varicose" waves and the instability to spiral disturbances. Reproduced from Maxworthy (1988).

of experiments have the effect of blurring the fundamental role of these characteristics. Figure 2.1 shows a pictorial representation of the formation of vortex breakdown from an axisymmetric (varicose) wave of large amplitude, followed by its instability to helicoidal waves.

The existence of solitary waves in the solutions of the Bragg-Hawthorne equations (see Shtern & Hussain, 1999) was shown by Leibovich (1990). These waves could have amplitudes large enough to cause flow reversal similar to vortex breakdown. Bifurcation of the solution occurs when the ratio of azimuthal to axial velocity changes. The branches of the bifurcation show multiple-columnar solutions which are found to correspond to Benjamin's conjugate states.

A quasi one-dimensional model was used by Darmofal *et al.* (2001) to show that there is a maximum far field pressure for which an unconfined vortex can remain smoothly varying. This point coincided with the transition

from supercritical to uncritical flow and the criticality condition proposed by Benjamin. For confined vortices the criticality condition is modified to include core stagnation pressure, relative to the outer flow. Revuelta (2004) notes that local criticality is a necessary condition for the appearance of vortex breakdown based on a standing wave analysis.

Recently, Rusak & Lee (2002) extended the theoretical work of Benjamin (1962) to include the effects of compressibility showing that increases in Mach number accounted for an increase in a critical swirl number (formulated using small perturbation theory). They found that the increase in critical swirl number was asymptotic at a Mach number related to the pipe diameter.

Mager (1972) shows that the solutions of the incompressible quasi-cylindrical momentum-integral equations have two distinct solution branches. Dissipations in flow force (similar to that in Benjamin, 1962) caused a jump from one branch to the other at a critical point upstream of the discontinuity.

Criticism of the Hydraulic Jump Analogy

Hall (1972) reviews the hydraulic jump analogy and refutes the theory based on measurements of the group velocity of standing waves on a vortex core, finding that they were predominantly downstream, meaning that waves could not propagate to an upstream standing wave. As there is no theoretical need for a near-critical flow to stagnate and that disturbances could not be propagated upstream, there is no need for a hydraulic jump-like state. Additionally, measurements at the time showed the upstream flow to be sub-critical and far from the critical state. Additionally, the hydraulic jump analogy – which relies on a dissipative turbulent state – does not describe observations of large scale vortex breakdown that is smooth and reversible (see Harvey, 1962).

Goldshtik & Hussain (1998a) proposes that inviscid vortex breakdown is a loss-free process, and therefore any analogy with hydraulic jump or shock like transitions should be avoided. This is based on the assertion that naturally occurring differences in flow force can be accounted for in solutions of the Stokes stream-function equation, and need not arise due to finite amplitude standing waves or shocks.

2.1.2 The Analogy with 2-Dimensional Boundary Layer Separation

Hall (1966) suggests that vortex breakdown is analogous to two-dimensional boundary layer separation. The theory stems from the nature of the two-dimensional boundary layer equations, whereby it is accepted that in simulations, boundary layer separation occurs when there is a failure of the assumptions. That is, if the flow is found to be at or near a reversed flow state at some spatial location, then the real boundary layer will experience a separation at or near that location. Hall extends this concept into an axisymmetric frame of reference. He uses the quasi-cylindrical approximation of the Navier-Stokes equations, where the model assumes that the stream surfaces are cylindrical and the axial velocity gradients are much smaller than the radial gradients. The failure of these assumptions and consequently the model, then becomes the requirement for vortex breakdown.

Hall (1966) derives a physical mechanism for the retardation of the flow, based on the boundary layer analogy. He considers that for a boundary layer, the pressure gradient along the boundary doesn't vary across the thickness of the boundary layer. For a quasi-cylindrical vortex core, he derives an equation which states that the pressure gradient along the axis will be more adverse than at the outer edge of the vortex, only if the stream surfaces

diverge.

Using this model in numerical simulations, Hall was successful at pinpointing the axial location of vortex breakdown to within 1.5 viscous core radii, as compared to previous experiments. He approximated the duct shape and included the measured azimuthal and axial velocity profiles as initial conditions. The thin boundary layer on the wall was ignored and the turbulent fluid was crudely represented by making the kinematic viscosity the eddy viscosity. Despite the assumptions made, the numerical model failed at the same time as a strong deficit in the core velocity emerged in the divergent part of the pipe. The location of the stagnation was very near the observed vortex breakdown location. Further tests showed that reductions in swirl level also moved the velocity deficit further downstream giving good agreement with the experimental observations.

The study by Reyna & Menne (1988) provides an interesting link between the analogy with hydraulic jump and the analogy with boundary layer separation. They proposed (similarly to Hall, 1966) that vortex breakdown is predicted by the failure of the assumptions used in the slender vortex approximation of the Navier-Stokes equations. They found that the critical condition based on this model corresponded to the critical condition derived by Benjamin (1962).

Criticism of the Analogy with 2-Dimensional Boundary Layer Separation

Despite the accuracy of the model in predicting the onset of breakdown, Hall admits that the analogy lacks the detail to be more than just a tool in vortex breakdown prediction (Hall, 1966).

2.1.3 Other Simplifications of the Navier-Stokes Equations

A variety of other simplifications of the Navier-Stokes equations for a variety of flow situations have been analytically studied in an effort to elucidate the mechanism of vortex breakdown. The results of such studies are explored here.

For a range of particular flow parameters, the steady, inviscid and incompressible Navier-Stokes equations as applied to a circular pipe with 'semi-infinite' length, show non-uniqueness of the solution (Goldshtik & Hussain, 1992, 1997, 1998a,b). For this range, there exists two solutions that are smooth along the length of the pipe and have the same mechanical energy. The flows represented by these solutions contain stagnation and regions of reversed flow similar to those seen in vortex breakdown. Interestingly they also found that the co-existing states have different flow forces, reflecting the hypothesis of Benjamin (1962).

Bossel (1969) proposes that vortex breakdown is a necessary feature of supercritical flows. The analysis however requires the use of a four region solution of the Navier-Stokes as shown in figure 2.2. These regions allow simplification of the equations of motion which give solutions with axial retardation, bulges and bubbles (with recirculation). However, these solutions are dependent on prescribing downstream conditions and a supercritical flow was not seen to contain a vortex breakdown region until a favourable downstream stream-function was applied. Despite the flaws, the solutions do show a range of behaviours that are commonly observed in vortex flows such as the axial positioning of the breakdown location depending on adverse pressure gradient, swirl dependence and Reynolds number independence.

The importance of viscous forces in the formation of vortex breakdown
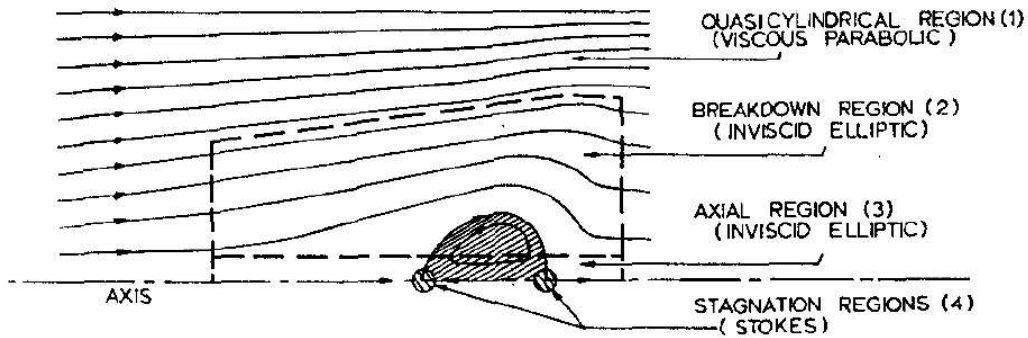
Figure 2.2: A diagrammatic representation of the four regions of solutions used in the model proposed by Bossel (1969).   Reproduced from Bossel (1969).

was shown by Krause (1985). Simplification the Navier-Stokes equations to express the pressure gradient along the centreline in the form of an integral relation revealed that one component of the frictional velocity could not be neglected. The conclusion was that viscous forces, along with inertial forces, contribute to the initiation of breakdown. The model also shows important similarities to the dynamics of observed vortex breakdown; increases in the initial axial velocity component were found to delay stagnation, as did reductions in the azimuthal velocity.

Wang & Rusak (1997b) demonstrated that a regular-expansion solution of the axisymmetric incompressible Navier-Stokes equations displays singularity. This means that a near-columnar vortex cannot exist at this point for near critical swirl. Also, beyond this point, two equilibrium states exist. Rusak *et al.* (1998) further explore the non-linear dynamics of the transition to axisymmetric breakdown. They show that their axisymmetric, unsteady and inviscid columnar flow, demonstrates the fundamental characteristics leading to vortex instability and breakdown.

Shtern & Hussain (1993) used the full Navier-Stokes equations of a swirling
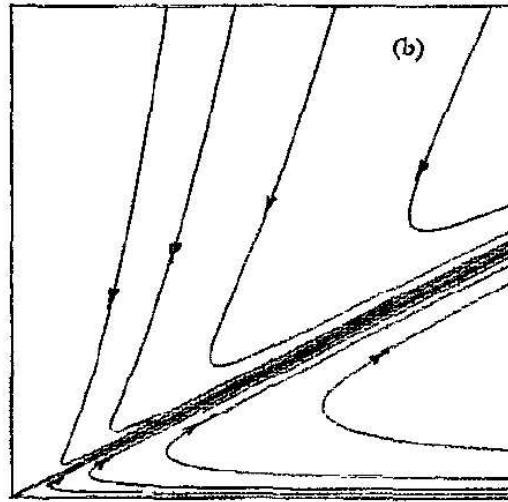
Figure 2.3: The cone form of vortex breakdown as described by one of three solution branches of the full Navier-Stokes equations. The axis of rotation is at the far left. Reproduced from Shtern & Hussain (1993).

jet emerging normal to a plane to show that three solution branches create a hysteresis loop with cusp catastrophes. They show that vortex flow similar to a tornado shows a solution with roughly conical two-celled expansion flow. This solution branch is identified as a possible vortex breakdown. For large circulations, a swirling cone (Figure 2.3) was observed. Shtern *et al.* (1997) and Shtern & Hussain (2000) then proposed a new class of solutions to the Navier-Stokes equations by considering vortex sinks on curved axisymmetric surfaces with axial flow, matching the flow with a swirling jet to avoid the singularity. These solutions displayed flow fields similar to those seen in vortex breakdown.

2.1.4   The Role of Hydrodynamic Instability

With the limited explanation of vortex breakdown provided by the theories of analogy with hydraulic jump and boundary layer separation, many studies

have supposed that hydrodynamic instabilities will give a more complete description. The following section details some of the studies focusing on stability of vortical flows.

The role of asymmetric disturbances in the vortex breakdown state selection process was recognised at an early stage; Sarpkaya (1971) found that for $1000 < Re < 2000$ the swirling flow was highly unstable to spiral disturbances. The majority of studies suppose that non-axisymmetric disturbances play only a secondary role in the mechanism of vortex breakdown (Leibovich, 1984). A predominantly axisymmetric mechanism is supported by the appearance of vortex breakdown-like states in axisymmetric simulations and in near-axisymmetric flows in closed containers. Indeed, most analytical studies assume axisymmetry and are quite successful at describing the main flow behaviours. However, the bias toward an axisymmetric model may be driven by the necessity of simplification of the governing equations.

Loss of stability to axisymmetric disturbances was shown to trigger the evolution of a near-critical base columnar flow to one representing flow around a stagnation point (Wang & Rusak, 1997a). The study examined the stability characteristics and time-asymptotic behaviour of the axisymmetric unsteady Euler equations for a swirling flow in a finite, constant area pipe. Gallaire & Chomaz (2004) extended this analysis to show that the inlet and outlet conditions can drive the instability. Their conclusions are based on an energy argument and observations of the effects of downstream and upstream disturbances upon each other. The propagation of disturbances both upstream and downstream is shown by spatial linear stability analysis, at a particular frequency range. The resulting flows in this range were stabilised or de-stabilised, depending on the ability of the inlet and outlet conditions to supply energy.

Differences in behaviour between flows in 'semi-infinite' pipes with solid body rotation and axial velocity, and those without axial velocity, were made by (Goldshtik & Hussain, 1992, 1997, 1998a,b). They found that the flows with axial velocity were inviscidly unstable to axisymmetric disturbances at large swirl numbers. Alternatively, the columnar vortex (no axial velocity) was found to be unconditionally stable.

An axisymmetric model of vortex breakdown does not explain the presence of asymmetric modes in some experiments. Some explanation for this discrepancy is given by Tromp & Beran (1997), where the condition causing the breaking of symmetry in solutions of the Navier-Stokes equations was found to be close to the onset of axisymmetric vortex breakdown. This result implies that axisymmetric forms of breakdown are quickly followed by asymmetric forms. Keller (1995) also shows that for axisymmetric forms of vortex breakdown (as defined by Benjamin, 1962), the departure from constant vortex core size and swirl ratio are surprisingly small. Keller concludes that the appearance of large departures must be due to viscous diffusion at low Reynolds numbers, and shear-layer instabilities at high Reynolds numbers. Based on the evidence in Panda & McLaughlin (1994), who found that axisymmetric instability waves were suppressed at high Reynolds numbers in swirling jets, these instabilities may be predominantly asymmetric.

Additional support for the axisymmetric mechanism for vortex breakdown is given in Tsitverblit (1993), where it is concluded that asymmetric bifurcation does not play a role in the appearance of vortex breakdown, but contributes to the transition from a steady to an oscillatory regime. Their application of the continuation method to study bifurcation of the steady Navier-Stokes equations shows good agreement for a range of parameters with steady vortex breakdown in experiments, and the geometric form of

vortex breakdown.

An important study highlighting the different modes of breakdown seen for jet- and wake-like axial velocity profiles for a range of Reynolds numbers was contributed by Ruith *et al.* (2003) and Ruith *et al.* (2004). These studies used the two-parametric velocity profile as described by Grabowski & Berger (1976) to study three-dimensionality and unsteadiness, mode selection and internal structure of vortex breakdown in three-dimensional, incompressible Navier-Stokes equations. Their findings show that low Reynolds numbers ($Re \leq 10$) showed no vortex breakdown or helical modes despite high swirl ratios. Larger Reynolds numbers ($Re \geq 10 - 100$) displayed the bubble, spiral and double helical modes. Wake-like profiles prove to allow the growth of a helical instability and therefore shows preference to asymmetric modes, while jet-like axial flow prefers axisymmetric solutions. Figure 2.4 shows streak-lines of the jet case tested by Grabowski & Berger (1976), simulated in three-dimensional flow. The three images show the axisymmetric bubble yielding to a helical instability with time. Ruith *et al.* (2003) concludes that Benjamin (1962) was correct in postulating that vortex breakdown is inherently axisymmetric. The transition to spiral modes is due to a large pocket of absolute instability in the wake of the bubble. Although this study is limited in its analysis, it highlights the dynamics in a model with minimum simplification.

Loiseleux & Chomaz (2003) observes the pre-breakdown behaviour of an unconfined swirling jet with respect to azimuthal modes of instability, finding the modes of instability with respect to swirl ratios (as defined by Billant *et al.* , 1998). They find that for swirl ratios near vortex breakdown, mode 1 instabilities persist, creating kinking and rotation of the vortex in the opposite sense to the swirling flow (spiral mode). Figure 2.5 shows the
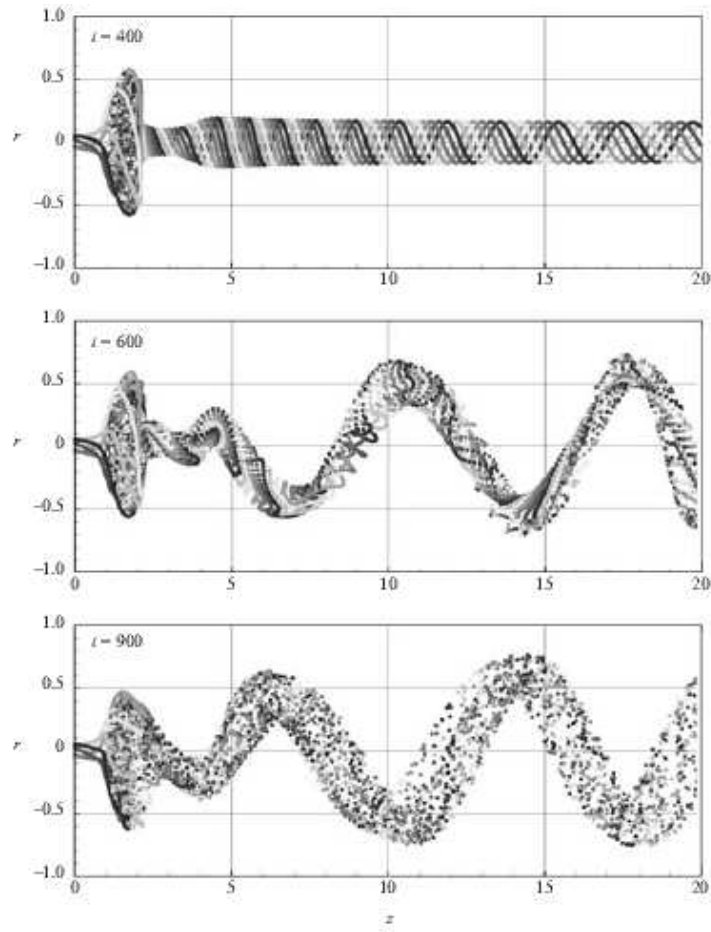
Figure 2.4: A series of streak-lines in time for the reference case tested by Ruith *et al.* (2003) showing the loss in axisymmetry and the growth in helical instabilities. Reproduced from Ruith *et al.* (2003).
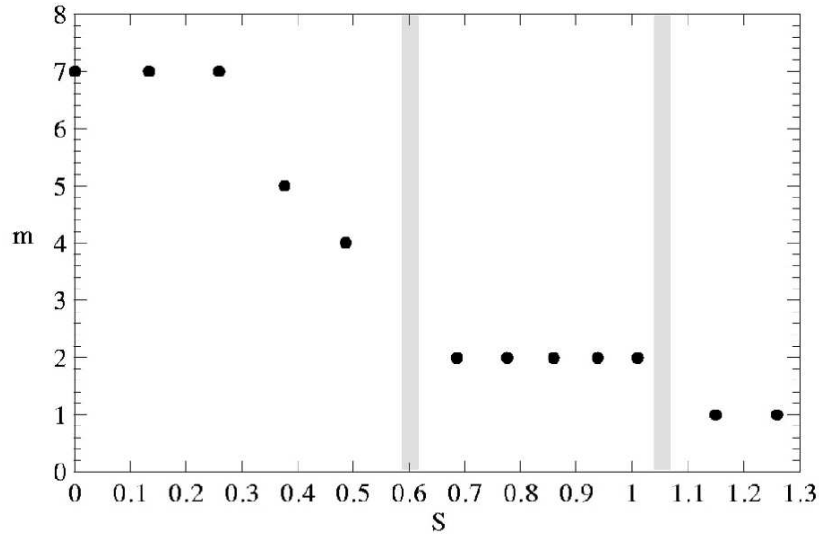
Figure 2.5: The dominant azimuthal wave numbers as a function of swirl ratio S. Reproduced from Loiseleux & Chomaz (2003)

modes plotted against swirl ratio. Gallaire *et al.* (2004) extends the work of Loiseleux & Chomaz (2003) by forcing the vortex with the use of a cam run set of syringes connected azimuthally to the nozzle. A strong response was shown to occur for $m = \pm 2$ and $m = \pm 3$, only when the frequency of forcing was an order of magnitude higher than that of the natural response. A marked resistance to disturbances was noted for the vortex core in general.

Peculiarities of Closed Cylinder Flow Vortex Breakdown

Vortex breakdown observed in closed containers with spinning lids tends to more axisymmetric than flows seen in pipes and over delta wings. In fact, suggestions of asymmetry of the base flow have in some respects been shown to be related to flaws in experimental techniques of visualisation and small geometrical misalignment of the experimental equipment (see Hourigan *et al.* , 1995; Thompson & Hourigan, 2003, respectively).

An alternative explanation for symmetry breaking in closed cylinder vortex breakdown is given by Tsitverblit & Kit (1998). This numerical study of the onset of unsteadiness reported in confined vortex flows (see Escudier, 1984) finds that the onset of axisymmetric oscillations was in fact not created by instability in the central vortex core, but that the instability mechanism originates in the wall region of the container. In this region, Taylor-Görtler vortices are migrated by the secondary motion (the diametric plane flow) induced by the spinning lid. These vortices tend to be swept away by the secondary flow before they can grow sufficiently (at $Re \approx 2000$). Increasing the Reynolds number up to $Re \approx 2550$ increased the intensity of the Taylor-Görtler vortices, however it also increased the intensity of the secondary recirculation, carrying them away quicker. The instability was found to grow at lower Reynolds number than those found for the independently considered wall region. This difference is attributed to a feedback of the instability into the start of the reversed Rayleigh region. This leads to the conclusion that exponentially growing infinitesimal disturbances, causing the unsteadiness observed by Escudier (1984) is created in the reversed Rayleigh discriminant region of the cylinder wall.

Floquet analysis was performed by Blackburn (2002) on the three-dimensional Navier-Stokes equations on the axisymmetric branch of the three possible solution branches for flow in a cylinder with a rotating end-wall. In accordance with Tsitverblit & Kit (1998), he found that the flow was unstable to rotating waves that displayed the characteristics not of circumferential instability, but of instability in the wall shear flow. Similarly, Marques & Lopez (2001) applied linear stability analysis to three-dimensional perturbations and found a Hopf bifurcation to a rotating wave leading to a $m = 4$ mode of instability (a series of four waves rotating in the same direction as the mean flow).

Type	Description
0	Axisymmetric Bubble
1	Turbulent Bubble
2	Spiral
3	Flattened Spiral Transition State
4	Flattened Bubble Transition State
5	Double Helix
6	Large Amplitude Low Re Filament Diversion

Table 2.1: List of the types of vortex breakdown described by Faler & Leibovich (1977)

Criticism of the Hydrodynamic Instability Theory

Hall (1972) denies the refutability of theories relying on hydrodynamic instability, stating that such a flow state, with large velocity gradients, is likely to have instabilities somewhere. Benjamin (1962) cites approximate axisymmetry shown by Harvey (1962), the presence of an abrupt expansion of the stream function and the steady behaviour of the breakdown state as contradictory evidence to the role of hydrodynamic instability.

2.2   Vortex Breakdown Dynamics

In this section, studies describing observations and measurements of vortex breakdown are presented. Initially the extensive observations of the dynamics of vortex breakdown in pipe flows performed by Faler & Leibovich (1977) is reviewed in detail. The seven resulting vortex breakdown types observed by Faler & Leibovich (1977) are given in table 2.1 which provides a short description of their main characteristic.

Type 0 refers to the traditional axisymmetric bubble vortex breakdown as described in §1.2.1. Apart from the early observations reported in §1.2.1, Faler & Leibovich (1977) also noted a secondary method of filling and emptying that was infrequently evident at low Reynolds numbers. The dual emptying and filling process, involved two emptying 'tails' diametrically opposed and two filling locations 90 degrees out of phase with these. The bubble type was also seen to move along the tube axis in a seemingly random fashion, sometimes settling on a single location for a short time before restarting oscillatory behaviour. Type 1 is a turbulent bubble where turbulence ensues at the bubble's widest point, giving a turbulent wake of approximately the same diameter as the bubble.

Type 2 refers to the spiral vortex breakdown as described in §1.2.2. The rotational sense of the spiral was confirmed as being in the same direction as the vortex core. The spiral form was seen to move randomly along the tube axis and increased in rotation speed and closeness of the spiral turns with upstream movement. Additionally, the Type 2 was also seen to spontaneously change into a Type 0 or Type 1 with a corresponding upstream displacement. With increases of circulation or Reynolds number, the Type 2 was seen to move upstream and become turbulent sooner. The frequency of rotation of the spiral filament also increases, along with the frequency of bi-stability switching between the spiral and bubble.

Type 3 and 4 are specialised cases found in transition between Types 5 and 6 and Types 0, 1 and 2 which represent a quasi-bubble or quasi-spiral that is flattened onto a meridional plane. The flattened spiral periodically sheds only on a preferred plane – similar to Kármán vortices. Increase of circulation leads to a morphing into the Type 0 or Type 2 variants.

The Type 5 and Type 6 breakdowns were observed to have distinct but

less abrupt movement of the vortex core away from the axis. The Type 5 being a double helix shearing of the vortex filament, while Type 6 is represented by a large amplitude divergence of the vortex filament away from the centreline. Both of these forms do not display a stagnation point and are therefore not usually considered to be vortex breakdown examples.

2.2.1 Mode Selection

This section describes, studies that deal with vortex breakdown mode selection.

Early observations of the spiral, bubble and the double helix types as seen in pipe flows (e.g. Sarpkaya, 1971) show that Reynolds number flows in the region $1000 \lesssim Re \lesssim 2000$ were less stable to asymmetric disturbances, and therefore more likely to experience the spiral and double helix form. Sarpkaya (1971) also observed a well defined bi-stability region where both the spiral and the bubble were observed for the same parameters.

Brücker (2002) devised an experimental apparatus that could force axisymmetry in a pipe flow. This was achieved by the rotation of the divergent pipe section. The vortex breakdown bubble achieved in this case was a long conical bubble that was near-axisymmetric and had a characteristic outer radius of 0.8 of the tube radius. Despite the fact that the form of the bubble region was significantly different to those seen in most other experiments, their results show that for conditions that normally favour asymmetric (spiral) forms, the bubble form only exists. They conclude that mode selection is influenced by the propagation of asymmetric disturbances upstream. Kurosaka *et al.* (2003) applied axisymmetric and asymmetric azimuthal waves to a pipe flow and achieved complete control over mode selection for a limited range of results. More limited success was achieved over a broader
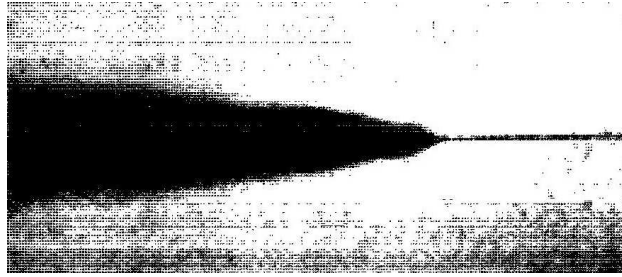
Figure 2.6: The turbulent conical state observed by Sarpkaya (1995) where the bubble and its turbulent wake have merged into one structure. Reproduced from Sarpkaya (1995)

range of forcing frequencies and Reynolds numbers (see §2.3.2 for the details of this study).

Spall (1996) studied the transition from spiral to bubble using numerical simulations of the three-dimensional, incompressible Navier-Stokes equations. He showed that transition from a spiral to a bubble could be initiated by a small increase in the magnitude of the free-stream velocity deceleration (the adverse pressure gradient). The resultant single recirculation region bubble state eventually becomes unstable and transitions back to an even stronger spiral.

Sarpkaya (1995) extended pipe flow observations into the turbulent flow region ($50 \times 10^3 \leq Re \leq 225 \times 10^3$) observing an acute angled conical turbulent wake after a bubble (beginning at $Re = 50 \times 10^3$) that merges with the bubble to form a turbulent conical form of vortex breakdown at $Re = 100 \times 10^3$ (see figure 2.6). These flows qualitatively compare with those observed in smoke visualisations of flows over in-flight F/A-18 fighter jets (see figure 1.1 lower). Although claims were made that these flows represented a new conical form of vortex breakdown, the form seen more likely describes a bubble type vortex breakdown with a large turbulent wake.

The mode selection of the wake of a simulated pipe flow with a central body (similar to a vortex breakdown bubble) was studied by Ortega-Casanova & Fernández-Feria (1999). The study highlighted the effect of inlet azimuthal velocity profile on the downstream structures of such pipe flows. They found a strong dependence on pipe geometry and azimuthal profile and an abrupt change in downstream structure above a threshold value of swirl. The downstream structures represented flows similar to those seen in the wakes of vortex breakdown, such as reformation of the vortex and subsequent breakdown.

The Breakdown State Observed in Cylinders with Rotating End-Wall

Vortex breakdown within closed cylindrical containers with a rotating end-wall were explored by Escudier (1984). This study shows that the ratio of height to container radius is an important parameter in the flow dynamics for cylindrical containers. A series of experiments at different height ratios demonstrates the presence of one, two and three separate vortex breakdown bubble modes. This study also provides the useful map of vortex breakdown states depending on height ratio and Reynolds number (as shown in figure 2.7 upper).

Spohn *et al.* (1998) extended the work of Escudier (1984) by exploring the differences between fully enclosed cylinders and those with a free surface. Figure 2.7 lower shows the alternative parameter map for cylinders with a free surface as developed by Spohn *et al.* (1998). The main difference found was that the vortex breakdown bubble becomes attached to the free-surface and the recirculation regions become elongated and larger. They found that closed cylinders maintained the vortex breakdown state whereas

in an open cylinder it would have vanished. The observations described a
vortex breakdown state that is similar to those in pipe flows; having an open
bubble structure (with inflow and outflow) that is axisymmetric upstream
and asymmetric downstream. In these flows, the asymmetry of the bubble
was identified as resulting from asymmetric separation of the flow along the
cylinder wall (see §2.1.4 and Blackburn, 2002).

Goldshtik & Hussain (1992, 1997, 1998b,a) argue that the flow state seen
in cylinders with a rotating end-wall is not a vortex breakdown state, but
merely an *internal separation* with reversed flow. They propose that vortex
breakdown requires a 'jump' and hysteretic transition between flow states.
This definition of vortex breakdown precludes the flow state seen in cylin-
ders because they do not display a jump or hysteresis; the bubble changes
smoothly with varying flow parameters.

Hourigan *et al.* (1995) argue the case for axisymmetric base flow in
closed cylinder containers and that the supposed asymmetric form of vortex
breakdown observed in experiments is an artifact of the limits of experimental
accuracy. The asymmetry of streak-lines of dye released along the centreline
of the container was attributed to the inherent asymmetry of the flow. In
this study, axisymmetric simulations with Lagrangian particle tracking were
used to show that in pre-vortex breakdown states, spiraling of a particle trace
released with a small offset from the centreline shows qualitatively similar
asymmetry to the experiments.

The effect of experimental imperfections on the resulting vortex break-
down state is studied by Ventikos (2002) and Thompson & Hourigan (2003).
In these studies, the three-dimensional Navier-Stokes equations are solved
for flows in cylindrical containers with slight imperfections comparable to
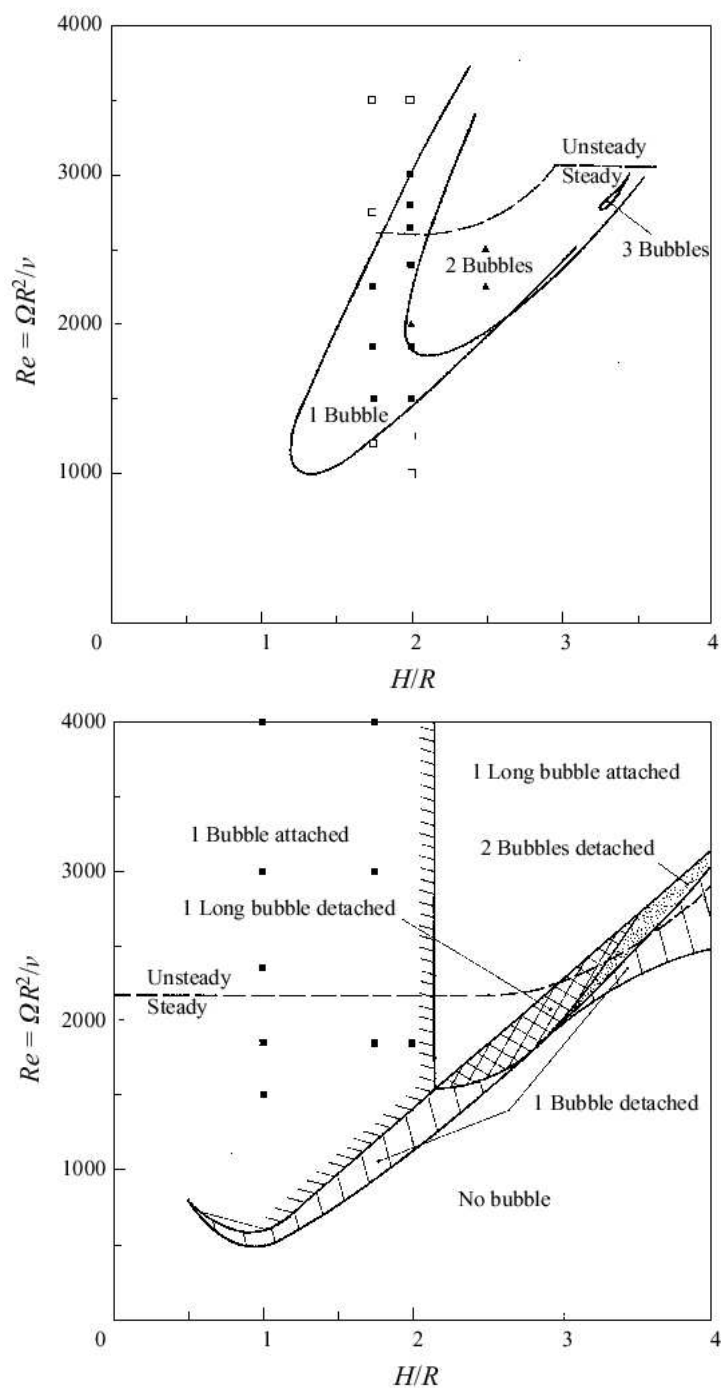those in experimental rigs. Ventikos (2002) studies the imperfections in the

Figure 2.7: The occurrence of vortex breakdown states in closed (upper) and open (lower) cylinders with a rotating end-wall for Reynolds number and height ratio. Reproduced from Spohn *et al.* (1998)
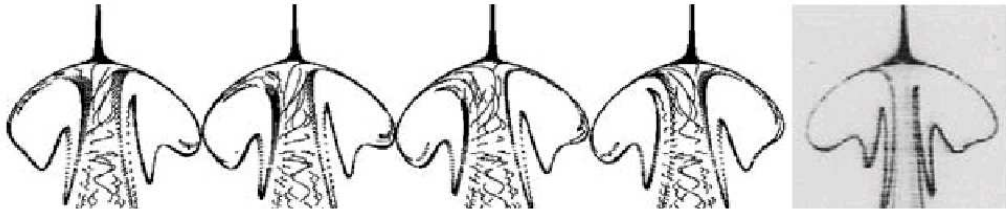
Figure 2.8: The break in symmetry of a vortex breakdown bubble due to 0.1°
angular misalignment of the rotating end-wall of a closed cylinder flow. A
variety of diametrical 'slices' are shown in comparison to an image from ex-
periments of Spohn *et al.* (1998). Reproduced from Thompson & Hourigan
(2003)

side-walls by simulating a slightly (1%) elliptical geometry and demonstrated
asymmetric resulting flows. Thompson & Hourigan (2003) offset the angle
between the container axis and the end-wall rotational axis to show that very
small misalignments can cause significant diversion of the flow from a purely
axisymmetric one. This is well illustrated in figure 2.8 where characteristic
folding is evident in the vortex breakdown bubble for a range of diametrical
slices of the computational domain, the far right picture being of visualisation
from Spohn *et al.* (1998).

A Novel Conical Vortex Breakdown State

A mode unobserved in flows in pipes and over delta wings, dubbed the 'cone',
was first seen by Khoo *et al.* (1997). Their experiments of tornados shows
a flow state that is similar to those analytically studied by Shtern & Hussain
(1993) and Shtern *et al.* (1997); a conical expansion of the vortex core
away from the vortex centreline. The cone was observed at relatively large
Reynolds numbers $Re \geq 3000$ and swirl. Figure 2.9 shows a representation
of the cone state observed; the main flow structure involved in these flows is

Figure 2.9: The conical state of vortex breakdown observed in tornado like flows. Reproduced from Khoo *et al.* (1997)

a tightly wound spiral that is not seen in the axisymmetric analysis of Shtern & Hussain (1993). Liang & Maxworthy (2005) show results similar to Khoo *et al.* (1997) with a tightly wound spiral progressing in a conical sense. They show that the spirals are formed by axial Kelvin-Helmholtz instability roll-up.

Coghe *et al.* (2004) also observe a cone-like structure in experiments of a swirl combustor at high swirl rates; however, the vortex is relatively confined in a cylinder and the conical breakdown attaches itself to the walls, creating an enclosed recirculation region behind the breakdown. Figure 2.10 shows a diagram of this confined conical breakdown. Kalkhoran *et al.* (1998) also observed a conical form of vortex breakdown at high Mach number, similar to the turbulent cone observed in Sarpkaya (1995).
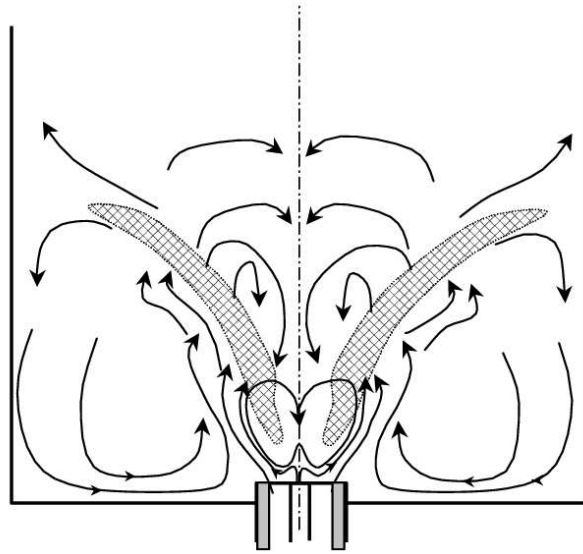
Figure 2.10: The cone state observed in a confined vortex combustor. Reproduced from Coghe *et al.* (2004)

A cone that shows even better comparison with the flow state identified by Shtern & Hussain (1993) was first discovered by Billant *et al.* (1998) in their experiments of unconfined swirling jets. The cone occurs at laminar Reynolds numbers and displays a 90° included angle expansion of the vortex core. Their cone had significantly different characteristics than the cone-like breakdown states seen in Khoo *et al.* (1997) and Sarpkaya (1995). These experiments show a cone-like state at high Reynolds number and could be explained as being a bubble with a wide, turbulent wake. Figure 2.11 shows the cone state as visualised with an axial laser sheet and a second laser sheet offset 20° from horizontal. The cone was consistently observed at $Re \lesssim 1000$.

The cone type was found to co-exist with a standard bubble type vortex breakdown. It was suggested that the bi-stability is caused by slight temperature inhomogeneities between the inlet flow and the otherwise stagnant tank flow; the resulting slight buoyancy increase was proposed to prefer the
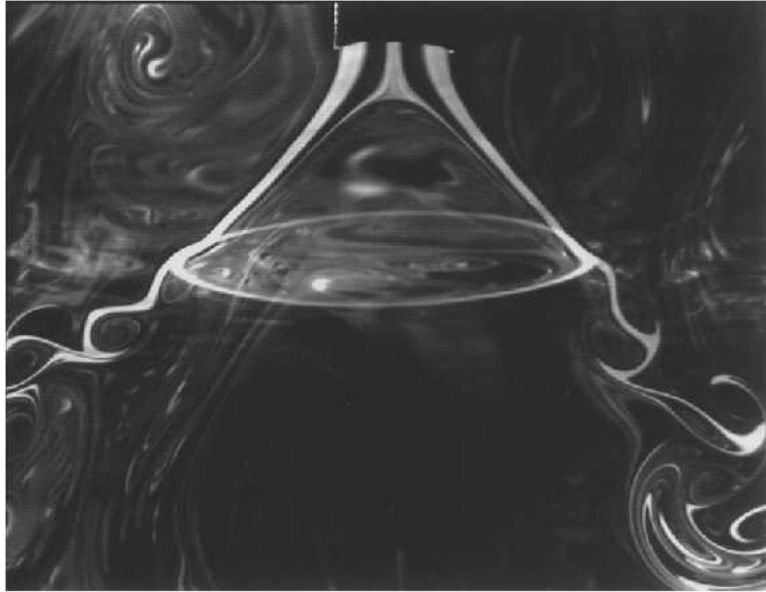
Figure 2.11: The proposed cone breakdown of Billant *et al.* (1998).

cone type. Both the bubble and the proposed cone were observed to have an asymmetric form at higher Reynolds numbers, where the bubble and cone became flattened. Billant *et al.* (1998) also showed that hysteresis was a measurable, but a fairly minimal phenomenon in vortex breakdown of unconfined swirling jets.

2.2.2 Numerical Studies

Grabowski & Berger (1976) were the first to numerically simulate vortex breakdown in an unconfined viscous vortex by solving the steady-state, axisymmetric Navier-Stokes Equations. They showed that the assumptions of steady state and axisymmetry led to solutions which exhibited some of the main features associated with vortex breakdown and compared favourably with the experimental observations of Sarpkaya (1971) and Bossel (1969).

The numerical study by Salas & Kuruvila (1989), of vortex breakdown in pipes using the stream-function-vorticity form of the steady, laminar, axisymmetric Navier-Stokes equations, was successful at producing flow recirculations similar to those seen in experiments. However, the form of the recirculation was qualitatively dissimilar to experimental observations. Multiple breakdown states (up to five different bubbles) emerging downstream for increases in Reynolds number were also observed.

Darmofal (1996) was only slightly more successful in simulating vortex breakdown using the axisymmetric form of the Navier-Stokes equations (stream-function-vorticity method). Using comparisons of velocity profiles upstream and downstream of the breakdown bubble, they showed that the forward halves of the simulated vortex breakdown bubbles were accurately representing their own experimental results. The latter half of the bubble showed differences that were explainable by assuming that the tail of the bubble was unstable to asymmetric disturbances. Similar to Salas & Kuruvila (1989), their vortex breakdown wake was seen to re-form and break down more than once, although less markedly. Sensitivity of the location of vortex breakdown due to the inlet boundary conditions was also observed.

More successful axisymmetric solutions were obtained by Beran (1994), where the time asymptotic behaviour of the vortex breakdown structure was dependent on initial conditions and the rate of variation of the inlet parameters. They achieved a single-celled vortex structure of slightly different form than that seen in three-dimensional simulations and experiments.

Keller *et al.* (1988) reviews numerical approaches based on the slender-vortex approximation and the Navier-Stokes approach, concluding that the slender-vortex approximation is successful at giving an insight into the physics of vortex breakdown despite not actually being able to determine the location

of the free stagnation point. The solutions to the Navier-Stokes equations, although giving much better representation of a vortex breakdown event, were found to be very sensitive to inflow and outflow conditions.

Spall *et al.* (1990) modelled the complex internal dynamics of the vortex breakdown bubble using unsteady three-dimensional incompressible Navier-Stokes equations with a Burger's vortex inflow condition. They found that the internal dynamics of the bubble type breakdown was highly asymmetric and contained multiple recirculation regions that compared excellently with those reported in Leibovich (1978). The bubble was seen to absorb fluid near the centreline of the wake section and releases fluid at the outer portion of the rear internal ring vortex. They reported bubble aspect ratios (length/diameter ≈ 1.75) with excellent similarity to those measured in previous experimental results. Their study shows that in order to represent the major internal structures of vortex breakdown in its entirety, unsteady three dimensional simulations are necessary. Their simulation at $Re = 200$ showed good qualitative and quantitative comparison of velocity, pressure and vorticity to earlier experimental work by Faler & Leibovich (1978).

Numerical simulations of an experimental set-up similar to that of Sarpkaya (1971) was conducted by Snyder & Spall (2000) using the three-dimensional, unsteady and laminar form of the Navier-Stokes equations. Their grid is shown in figure 2.12 with contours of azimuthal velocity superimposed. They chose to simulate the vanes used by Sarpkaya to avoid constraining the velocity at the entry to the pipe and therefore avoid contamination of the solution to upstream propagating asymmetric disturbances. They found that the use of constrained velocity conditions at the pipe do not affect the location or structure of vortex breakdown.

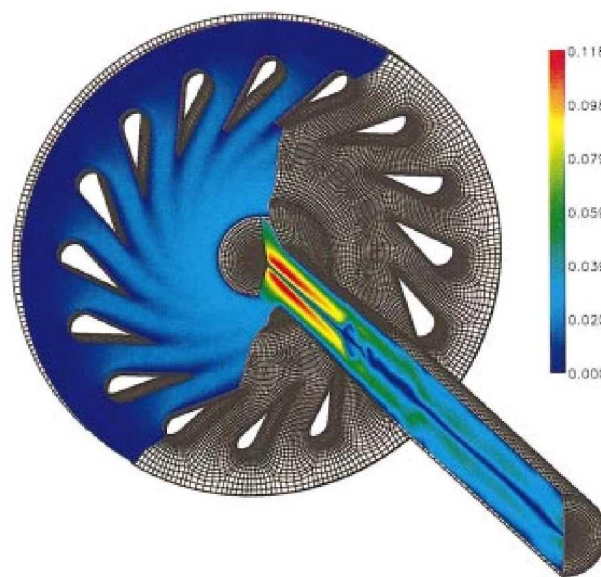In simulations of the flow over delta wings, Hsu & Liu (1992) achieved

Figure 2.12: The computational domain as used to simulate pipe flows more accurately. Note, the addition of turning vanes removes the need to impose velocity profiles at the pipe inlet. The contours show azimuthal velocity. Reproduced from Snyder & Spall (2000)

reasonable qualitative comparisons using the three-dimensional incompressible Navier-Stokes equations. Their results, however, were limited to time-independent flows and the bubble form of breakdown only.

With the increase in computational power, the simulation of turbulent flows has recently begun. Mary (2003) performed Large Eddy Simulations (LES) of flow over a delta wing at $Re = 1.6 \times 10^6$ and found that simulations were inaccurate using a no-slip condition on the wing with or without the logarithmic law (see Mary, 2003). Additionally, simulations were found to be under-resolved using the grid resolution studied, suggesting that the future of modelling vortex breakdown with turbulent effects is still to be achieved.

Sotiropolous *et al.* (2001) examined the Lagrangian dynamics of a particle interacting with vortex breakdown within three-dimensional closed cylindrical containers with rotating lids. Based on their observations they argued that the Eulerian characteristics of the flow are able to be ascertained by axisymmetric computations because the asymmetric component of the flow is small compared to the axisymmetric component. They found that the small asymmetric perturbations drastically alter the Lagrangian characteristics of the flow by increasing the chaotic nature of the flow.

In a numerical study, Beran (1994) observed hysteresis in the solutions of the unsteady axisymmetric Navier-Stokes equations, with changes in circulation.

2.2.3   Time-Dependent Dynamics

Gursul & Yang (1995) used flow visualisation and velocity measurements (using Laser-Doppler Velocimetry) to study the unsteady vortex breakdown location over a delta wing. They found that vortex breakdown fluctuations in location occur at much lower frequencies than than the hydrodynamic

instability of the wake of the breakdown bubble. Directly comparing the frequency of the helical mode instability of the wake shows that this instability does not influence the unsteady nature of vortex's longitudinal location, refuting previous hypotheses that the two are linked.

Menke *et al.* (1999) also reported on the unsteady dynamics of vortex breakdown over delta wings noting that the Strouhal frequencies of oscillation of the downstream location were much lower than those of any known instabilities. A mechanism of interaction between adjacent vortex breakdown states was proposed and shown to be important in the low frequency longitudinal oscillations (see also Menke & Gursul, 1997). Although this mechanism was not explained, its increased effect at higher angles of attack indicates that it is an oscillation of the mean flow similar to that seen in many bluff body applications (Von Kármán instability). Menke & Gursul (1997) added velocity profile measurements (see figure 2.13) including a variety of unsteady velocity measurements showing very large fluctuations in both the axial and azimuthal velocities with and without the presence of vortex breakdown.

Lagrangian particle tracking and experimental visualisation were employed by Sotiropolous *et al.* (2001, 2002) to observe particle paths interior to vortex breakdown bubbles in closed cylinders with a rotating end-wall. Differences between the numerical solutions and the experimental results are observed; Additionally, they observed that the emptying of the bubble occurs in bursts as opposed to continuous release. In flows demonstrating two bubbles, they observed that the second bubble was surprisingly axisymmetric, despite the asymmetry of the upstream bubble. The axisymmetry of the second bubble was proposed to be due to the different swirl condition.
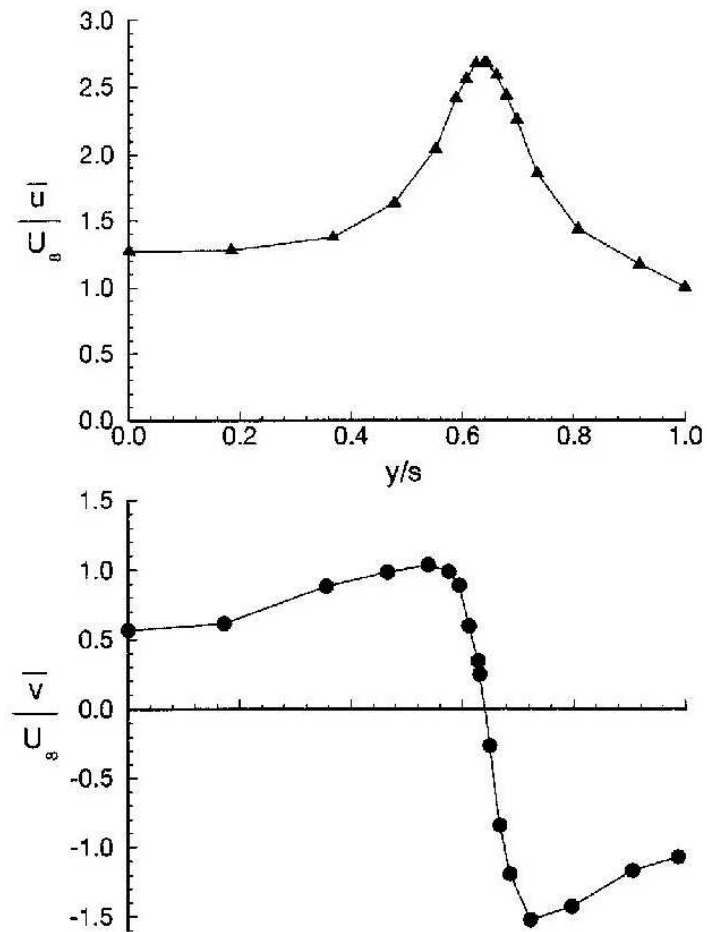
Figure 2.13: A diagrammatic representation of studied delta wing vortex breakdown showing the delta wing with the leading edge shear layer roll-up. The vortex on the left shows a typical azimuthal velocity profile, while the right vortex shows the typical axial velocity profile. Reproduced from Menke & Gursul (1997).

2.2.4 The Onset of Vortex Breakdown

This section outlines studies that focus on conditions leading to vortex breakdown in a variety of flow situations.

A switch in azimuthal vorticity of the jet flow over a delta wing was observed by Özgören *et al.* (2002) to occur at the inception of vortex breakdown. Detailed images of the structure of vortex breakdown emphasising instantaneous vorticity were presented. The switch in vorticity was identified to occur in both instantaneous and time-averaged vorticity. This switching of vorticity precedes the stagnation of the axial velocity and is identified as a useful indicator of vortex breakdown incipience.

Fernandez-Feria & Ortega-Cassanova (1999) uses the axisymmetric Euler equations with two families of inlet conditions applied, one singular at the centreline and a more realistic viscosity regularised profile. They showed that for both diverging and converging pipes, cylindrical solutions for the downstream flow, determined by the inlet flow, exist even for large swirl parameters for the singular velocity profiles. For the viscosity regularised flows, characterised by constant axial flow, solid-body rotation and small core radius, flow reversal on the centreline was observed. The implication of this is that vortex breakdown is governed by viscous effects.

Some indication that vortex breakdown is unable to be achieved in a converging tube is given by MacDonald (2003) who performed experiments in impulsively rotated converging and diverging tubes with slow moving axial flow. MacDonald showed a vortex breakdown-like region of reversed flow in the diverging tube, whereas the converging tube shows only a toroidal recirculation at the tube wall.

Revuelta (2004) studied swirling flow in pipes with sudden expansions using the quasi-cylindrical approximation of the Navier-Stokes equations.

Revuelta found that a pipe divergence causes bifurcation of the solution into two branches which were seen to fold for limited swirl, leading to multiple solutions. Above a limiting expansion ratio the fold disappears leaving only one possible solution for all swirls. Reynolds numbers below $Re = 125$ also show solutions without a fold.

Critical Conditions for Breakdown Onset

Presented here are the studies that develop a parameter to measure the incipiency of vortex breakdown.

Hall (1972) proposes the swirl angle ϕ, defined by

$$\phi = \tan^{-1} \frac{v}{w}, \tag{2.1}$$

where v and w are the local azimuthal and axial velocities respectively. This parameter can be applied as a function of radius, where the maximum value indicates the overall characteristic swirl angle of the vortex. Hall (1972) proposes a loose criterion that for vortex breakdown to occur downstream a swirl angle $\phi \gtrsim 40°$ is required. Deng & Gursul (1996) finds that the swirl angle ϕ is insufficient to locate the occurrence of vortex breakdown over delta wings with any accuracy.

Spall *et al.* (1987) reinterpreted results from previous experiments in light of the Rossby number defined as

$$Ro \equiv \frac{U^*}{r^*\Omega}, \tag{2.2}$$

where U^*, r^* and Ω are the characteristic axial velocity, radius and rotation rate respectively. This study found that for wing tip type vortices and for $Re \geq 100$, that vortex breakdown occurs below a critical $Ro = 0.65$. Figure 2.14 shows the Rossby numbers for a variety of studies. Here, the
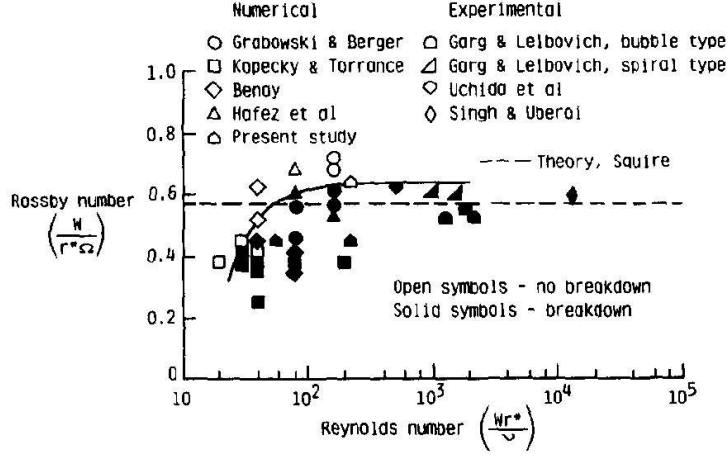
Figure 2.14: The Rossby number required for vortex breakdown in wing-tip vortices as a function of Reynolds number. Reproduced from Spall *et al.* (1987).

critical Rossby number was seen to increase as a function of Reynolds number, becoming independent at $Re \gtrsim 100$. Despite the apparent success of the Rossby number in providing a critical parameter for the onset of vortex breakdown, its application to a swirling jet experiment yielded a spread in critical numbers of $0.55 \lesssim Ro \lesssim 0.85$ (see Billant *et al.* , 1998).

Farokhi *et al.* (1989) defined an integrated parameter (also used by Panda & McLaughlin, 1994) for measuring the swirl of a jet. Their parameter referred to here as S_f was defined as

$$S_f \equiv \frac{G_\theta}{G_x R}, \qquad (2.3)$$

where G_θ is the jet torque, defined as

$$G_\theta \equiv 2\pi \int_0^\infty \rho U W r^2 \mathrm{d}r, \qquad (2.4)$$

G_x is the axial thrust, given by

$$G_x \equiv 2\pi \int_0^\infty [\rho U^2 + (p - p_\infty)]r\mathrm{d}r, \tag{2.5}$$

and R is the nozzle radius. Farokhi *et al.* (1989) used an experimental set-up that could produce two different forms of azimuthal velocity profile, one with solid body rotation and one with a free-vortex profile. Velocity profiles for two cases with the same integrated swirl ratio ($S_f = 0.48$) were published, where one shows the inception of vortex breakdown (the free vortex profile case) and the other shows no sign of breakdown. These experiments led Farokhi *et al.* (1989) to conclude that integrated parameters were inadequate for defining vortex breakdown onset.

Billant *et al.* (1998) proposes a swirl ratio and corresponding critical condition based on a Bernoulli's equation analysis of the streamline on the axis of symmetry. The analysis is of a Rankine vortex (solid body rotation in the core region, surrounded by irrotational flow) with a stagnation point on the centreline a finite distance downstream, the swirl ratio (as defined by equation 2.6) will be $S = \sqrt{2}$ or $S \geq \sqrt{2}$, depending on whether the stagnation point relates to a cone or bubble type breakdown, respectively.

$$S \equiv \frac{2W_{(R/2,z_0)}}{U_{(0,z_0)}}, \tag{2.6}$$

where $W_{(R/2,z_0)}$ is the azimuthal velocity at half the nozzle radius R from the centreline and $U_{(0,z_0)}$ is the centreline axial velocity, and $z = z_0$ is a location upstream of the vortex breakdown occurrence. Both the swirl velocity and the axial velocity used in this formulation were approximated with the maximum swirl velocity and the centreline axial velocity. Figure 2.15 shows the results of measuring the critical swirl ratios S_c for a range of Reynolds numbers in a swirling jet experiment (see Billant *et al.* , 1998). Their results show good agreement with the criterion developed in their analy-
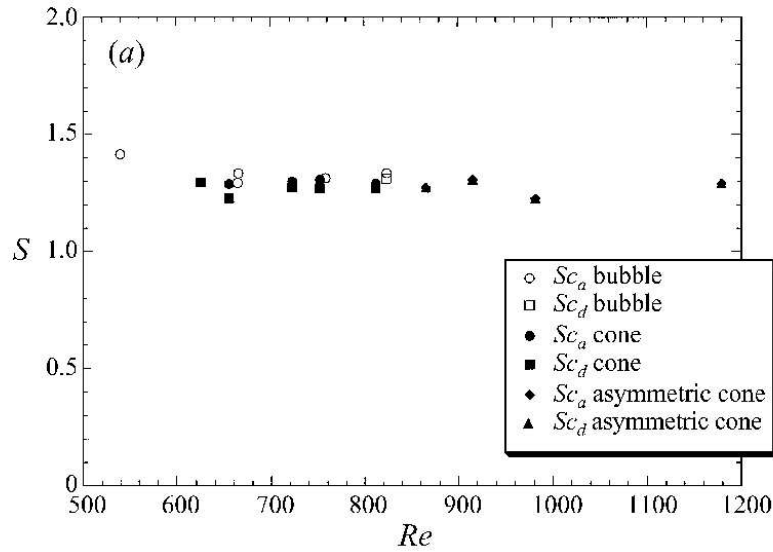
Figure 2.15: The swirl ratios for vortex breakdown in a swirling jet, where the analysis predicts breakdown at $S \geq 1.44$. Reproduced from Billant *et al.* (1998)

sis ($S = 1.44$). Marginal improvements were also gained by dismissing the Rankine vortex assumption and using an integrated azimuthal velocity formulation of the swirl ratio denoted as S_i. The success of the Bernoulli's equation analysis of the vortex core is impressive, however the applicability of the swirl ratio (S) formulation is questionable considering the peculiar axial velocity profile created by their experimental apparatus. Billant *et al.* (1998) also applies the Rossby number to their experiments, giving poorer collapse on the critical criterion than seen in Spall *et al.* (1987).

Compressibility effects were studied by Herrada (2003) using the axisymmetric Navier-Stokes equations and the quasi-cylindrical approximation of Benjamin (1962). The steady state solutions describe a range of flow states depending on Mach number, Reynolds number and velocity profiles. More importantly, they found that the critical threshold for vortex break-

down increased with Mach number. They demonstrated that the quasi-
cylindrical approximation was representative of the near-inviscid, incom-
pressible, Navier-Stokes equations. This result is reflective of the analytical
results of Rusak & Lee (2002) as described in §2.1.

2.3 The Control of Vortex Breakdown

Vortex breakdown has importance in a range of swirling flows that can ei-
ther benefit or suffer from its presence. Hence, much research into vortex
breakdown has focused intensively on aspects of control. Presented here is a
discussion on studies that focus on control aspects is given in sections dealing
with each flow type; delta wings, closed cylinders, etc.

2.3.1 Delta Wings

Significant buffeting and aerodynamic stability issues arise with high angle
of attack flight regimes that are caused mainly by the presence of an unstable
and unpredictable vortex breakdown state. Additionally, vortex breakdown
is responsible for loss of high angle of attack lift. The need to control vortex
breakdown in order to suppress, induce and stabilise, has been an important
impetus in research direction. For further information, Mitchell & Délery
(2001) extensively review the control of vortex breakdown over slender delta
wings.

In an attempt to control the longitudinal location of vortex breakdown,
Wang *et al.* (2003) used a vectored jet at the trailing edge of the delta wing
with varying angles measured between the trailing edge chord and the jet
direction (for 90°, the jet was directly downstream). Jet angles above 30°
generally caused permanent movement of the breakdown downstream for the

breakdown on the same side as the jet pointed. They also found that this effect decreased with increasing angle of attack. Menke *et al.* (1999) showed that adding a splitter plate between two halves of a delta wing suppressed low frequency longitudinal oscillations giving more stationary breakdown locations.

Similarly, Schmücker & Gersten (1988) used a series of jets on the centre-line just below the delta wing apex to control the location of vortex breakdown. They showed that blowing along the axis of vortex breakdown yields a delayed stagnation and therefore vortex breakdown occurs further downstream than without blowing.

Deng & Gursul (1996, 1997) achieved results similar to the blowing techniques by using leading edge flaps in fixed angle and in oscillating regimes. Initial investigation showed that flap angle has a marked effect on the location of vortex breakdown. More detailed investigation found that fixed flaps at 100° (as measured from the top surface of the wing) moved the vortex breakdown location from near the trailing edge to 10% of a chord length from the delta wing apex for an angle of attack of 30°. Generally, increases in flap angle caused the vortex breakdown location to move upstream. For smaller angles of attack, their results became less marked giving some indication that vortex breakdown is more strongly affected by adverse pressure gradients. Results for cases with flap oscillation proved little increase in control over fixed flap scenarios.

Akilli & Sahin (2003) sought to induce vortex breakdown and alter the turbulence characteristics by employing a coaxial wire aligned with the core of a leading edge vortex. The wire used was of very small diameter (1% of vortex core diameter) and a variety of wire lengths (measured from the leading edge) were tested. They found that even short wires in the order

of half the chord length have a dramatic effect on the location of vortex breakdown spirals, however, not for higher angles of attack ($\geq 35°$).

2.3.2   Pipe Flows

A reasonable amount of control of the selected vortex breakdown state in a pipe was achieved by Kurosaka *et al.* (2003) where azimuthal waveforms of modes $0, 1, -1$ were created by an array of oscillating pistons. Their results show that axisymmetric disturbances ($m = 0$) at Strouhal frequencies $St \gtrsim 0.22$, caused spiral breakdown to form a bubble state and to move upstream. For weak bubbles, disturbances of $m = +1$ (asymmetric azimuthal waves in the same direction as the swirling flow), at $0.16 \lesssim St \lesssim 0.19$ caused the bubble breakdown to form a spiral. In both of these situations, the vortex breakdown state remained permanently altered while the disturbances were applied. Forcing frequencies outside of these parameters had more limited effect, as did forcing of more vigorous breakdown states. The results show that hydrodynamic instability plays a major role in vortex breakdown state selection.

Sarpkaya (1971) conducted experiments to observe the response of vortex breakdown bubbles to small changes to the upstream conditions. This was achieved by varied methods including oscillation of one of the swirl vanes, and varying the angle of all blades at once. Mainly Sarpkaya found that when the blade angles were increased, and hence the overall swirl magnitude, the vortex breakdown bubble moved downstream a distance of $0.2D_o$ (where D_o was the smaller diameter of the diverging tube). After a noticeable pause, the breakdown moved rapidly upstream and overshooting before settling to the new upstream location. The process was seen to be reversed for decrease in swirl. Similar results were achieved by accelerating and decelerating the flow
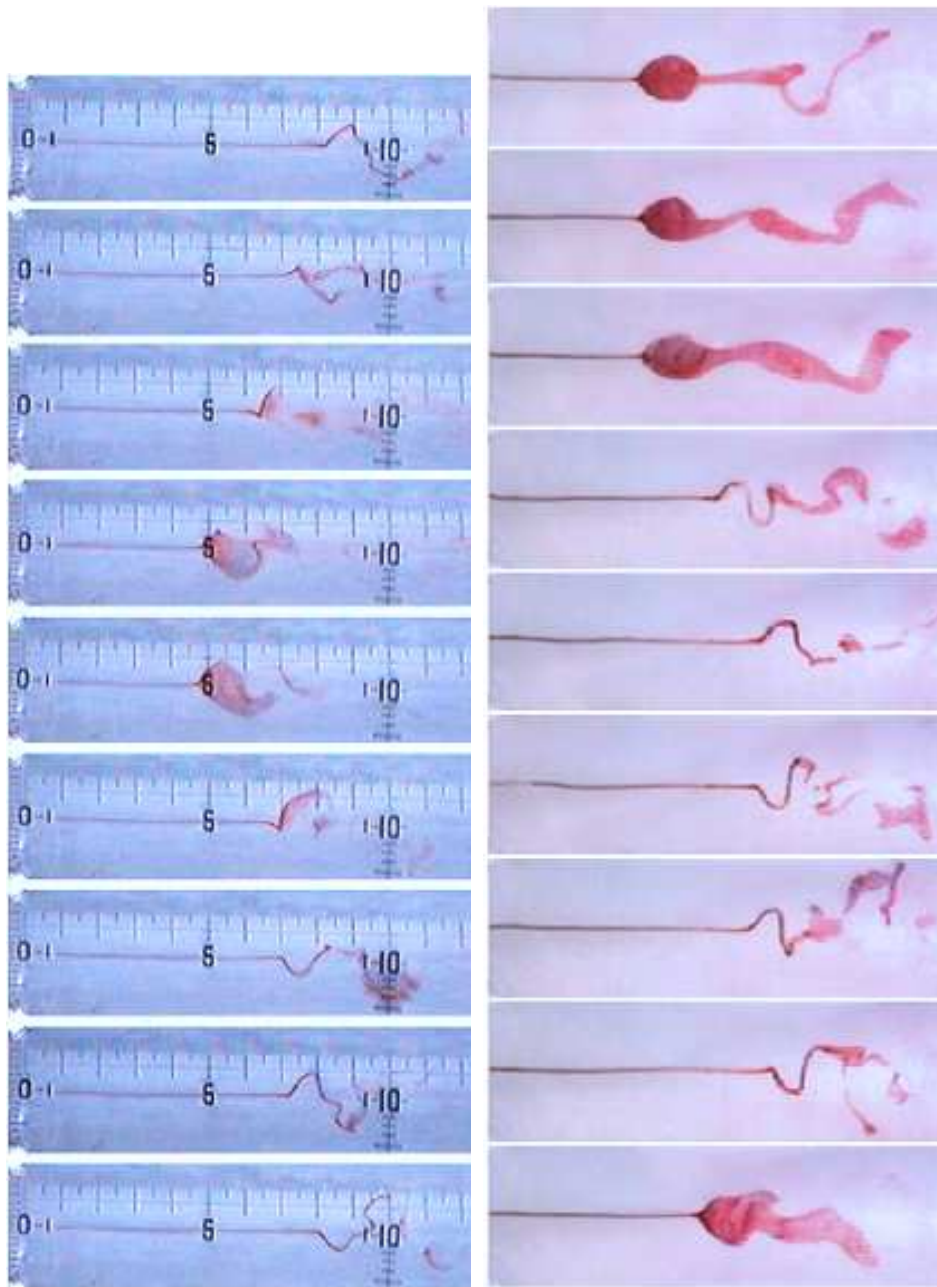
Figure 2.16: Results of upstream azimuthal waves on spiral and bubble vortex breakdown. Left shows m=0 disturbance (axisymmetric) of a spiral form of breakdown. Right shows m=+1 disturbance of a bubble type breakdown. Reproduced from Kurosaka *et al.* (2003)

by means of constriction or opening of the outlet. Increasing the constriction created a greater adverse pressure gradient that led to the vortex breakdown state settling further upstream.

2.3.3 Cylindrical Containers

Recently, Fujimura *et al.* (2004) examined the effect of rotating the normally fixed bottom and side-walls in co-rotation and counter-rotation. They found that for co-rotation the bubble was further from the rotating end-wall, and closer for counter-rotating. Mununga *et al.* (2004a,b) have shown that vortex breakdown location could be significantly and permanently altered by the rotation (co- and counter-) of a small disk at the opposite end of the cylinder to the rotating disk impeller. The rotation also has a significant effect on the critical Reynolds number for vortex breakdown.

Herrada (2003) showed that temperature gradients along the axis that create a counter-flow have the effect of suppressing vortex breakdown. Conversely, co-flow enhances vortex breakdown size and unsteadiness that is local to the axis area. Husain *et al.* (2003) used a rotating rod through the whole axis of the cylinder employing co- and counter- rotation with the same effect of suppressing size with the former and enhancing size (and unsteadiness) with the latter.

2.4 Literature Summary

Despite the large body of studies focusing on the mechanism of vortex breakdown, little consensus has been reached. Support for a fundamental axisymmetric mode is strong, with spiral forms being due to asymmetric perturbation of the axisymmetric base form. Many simplifications of the Navier-

Stokes equations have shown comparative vortex breakdown forms and full three-dimensional studies have shown spiral forms of breakdown, as well as axisymmetric forms.

Some studies have also attempted to develop a critical criterion for vortex breakdown, leading to criteria based on local velocity angle, ratios of velocities and ratios of conserved properties. However, these studies also lack consensus about the universality of critical criteria, with application of a criterion to a different experiment showing poor collapses.

This thesis will focus on the universality of vortex breakdown criteria, using the promising analysis of Billant *et al.* (1998) as a starting point.

Chapter 3

Numerical Method

This chapter describes the general method used in the presented studies. This includes a description of the physical model, the mathematical model and the computational method used to solve the mathematical equations on a discretised domain. Finally A discussion of the model validation is given showing flow visualisations and a comparison of the critical swirl ratio prediction with the experimental equivalent.

3.1 Physical Model

The initial aim of the present simulations was to replicate the unconfined swirling jet experiments of Billant *et al.* (1998). Their experimental configuration included a tank of otherwise stagnant fluid with a swirling jet apparatus attached at the top (see figure 3.1). The tank was a square cylinder of dimension $x/R = 20 \times y/R = 20 \times z/R = 60$, where R was the jet nozzle radius. The tank included a honeycomb section to ensure the tank outlet flow was purely axial. The swirling jet apparatus included a rotating honeycomb section that imparted solid body rotation onto the through flow,
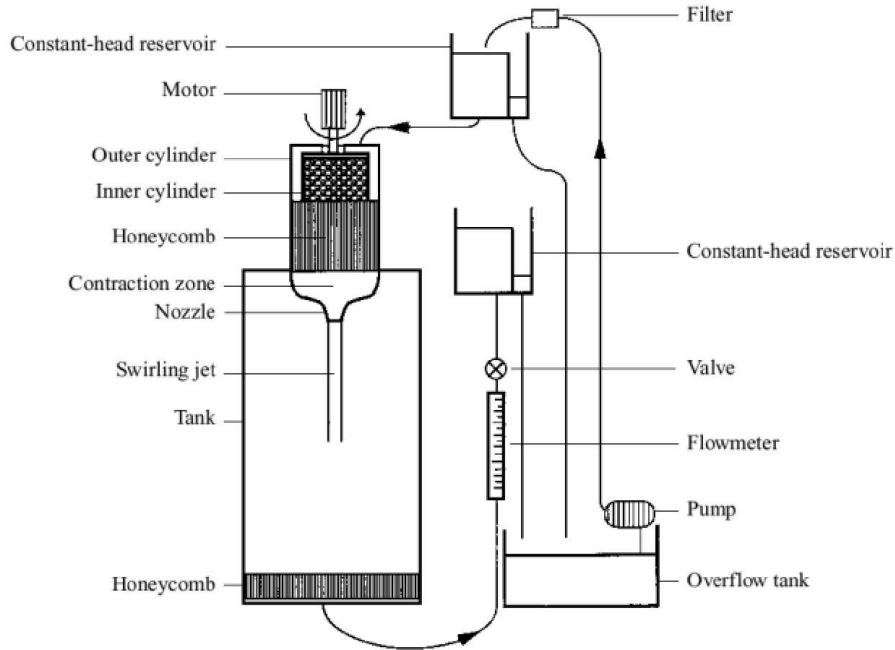
Figure 3.1: The experimental rig of Billant *et al.* (1998) used as a physical basis for the present simulations.

which was driven by a constant head reservoir set-up. After passing through the honeycomb section of the swirl generator, the flow enters a contraction and finally passes through the nozzle, and into the tank.

The physical model used in these experiments assumes the absence of density variation throughout the fluid, hence gravity effects are negligible. Axisymmetry of the flow is also assumed such that the tank is modelled as a circular cylinder. The contraction region is ignored as the numerical method allows the direct specification of velocity profiles at the nozzle outlet. The outlet of the computational domain is physically positioned just before the honeycomb at $z/R = 56$. The outlet boundary is assumed to have a constant outflow with the same mass flux as the inlet. The outer wall of the cylindrical tank is assumed to be at a great enough radial distance to have a negligible

effect on the flow. In the case of the simulations presented here, this wall is placed at $r/R = 10$. The region adjacent to the nozzle is also assumed to have negligible effect on the flow and therefore is modelled as a wall. Figure 3.2 shows the physical model used in these simulations.

The main flow parameters used to characterise the unconfined swirling jet are the Reynolds number Re and the swirl ratio S. The Reynolds number is used to non-dimensionalise the mass flow rate averaged axial velocity $\bar{U}$ with the nozzle diameter D and the kinematic viscosity ν

$$Re = \frac{\bar{U}D}{\nu}. \tag{3.1}$$

The swirl ratio is used to non-dimensionalise the maximum azimuthal velocity W_0, with the centreline axial velocity U_0, both measured at the nozzle outlet.

$$S \equiv \frac{2W_0}{U_0} \tag{3.2}$$

3.2   Mathematical Model

The mathematical model used to simulate the flow conditions in the physical model are the governing equations of fluid flow commonly known collectively as the Navier-Stokes equations. The Navier-Stokes equations consist of the momentum equations and the continuity equation. In their general form they are a formidable set of equations and they have only been analytically solved for a limited set of cases involving many simplifications. The Navier-Stokes equations are only valid for Newtonian fluids, that is fluids that have a linear shear stress and shear strain relationship. In the present simulations the fluid is assumed to be Newtonian and incompressible (constant density) in space
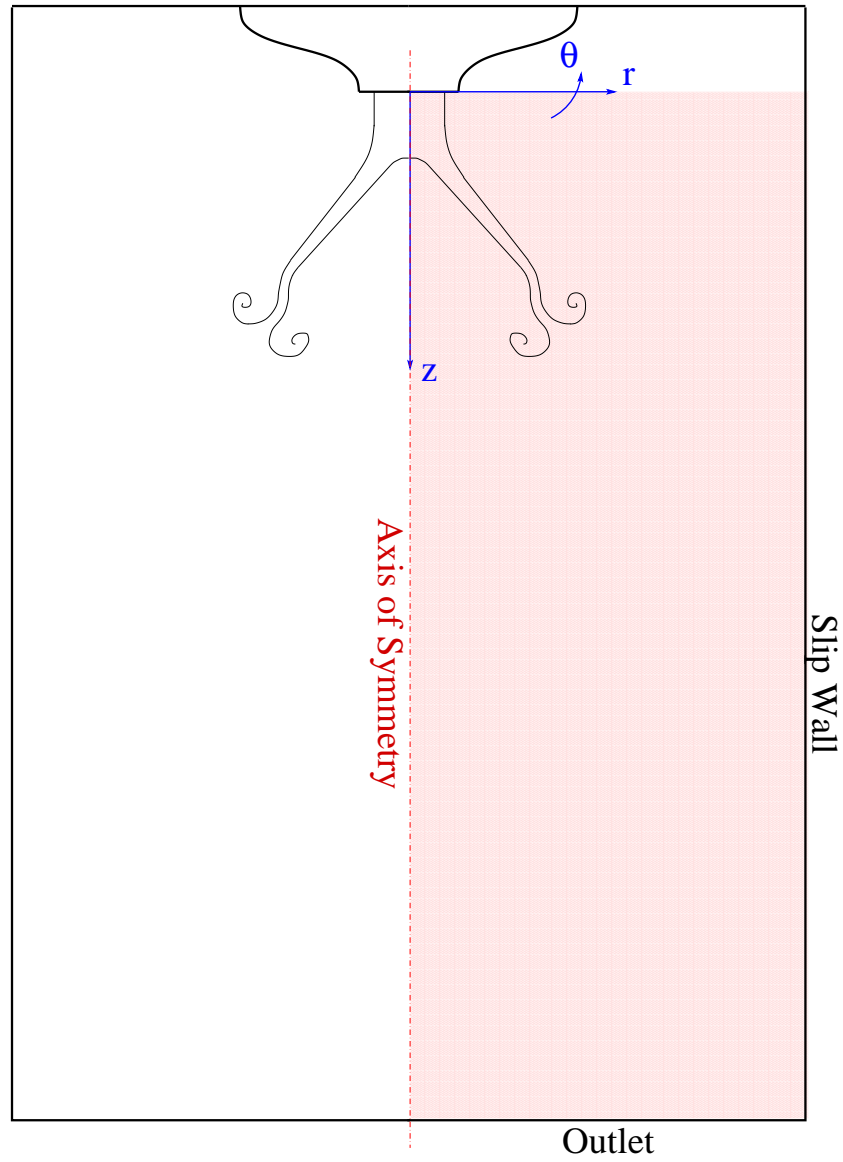
Figure 3.2: The computational domain (shaded in red) used to represent the experimental rig of Billant *et al.* (1998).

and time. This assumption is appropriate for flows with a Mach number $Ma \lesssim 0.3$, a limit for which the flows in these simulations are well within.

The non-dimensionalised vector form of the momentum equation of the complete Navier-Stokes equations is

$$\frac{\partial \mathbf{u}}{\partial t} = \nabla p + \frac{1}{Re}(\nabla^2 \mathbf{u}) - (\mathbf{u} \cdot \nabla)\mathbf{u}, \tag{3.3}$$

and the continuity equation is

$$\nabla \cdot \mathbf{u} = 0, \tag{3.4}$$

where $\mathbf{u} = \mathbf{u}(x, y, z) = (U, V, W)$ is the normalised velocity field, $p = P/\rho$ is the normalised kinematic pressure and Re is the Reynolds number.

The momentum equation includes a pressure term, a diffusion term and a non-linear advection term from left to right respectively.

3.3 Computational Model

This section describes the discretisation in space and time, the computational grid and the implementation of boundary conditions. The numerical simulations presented in this thesis utilise an 'in-house' CFD code developed by Mark Thompson and Kerry Hourigan (from the Department of Mechanical Engineering, Monash University, Melbourne, Australia). This code has been extensively validated for a variety of different relevant simulations (for example Hourigan *et al.* (2001), Thompson *et al.* (2001), and the references therein). The method is based on the Galerkin finite element method in two dimensions with high-order Lagrangian interpolants used within each element. The complete method is known as the *spectral-element method* as it has convergence behaviour of global spectral methods. The main components

of the method are the spatial discretisation and the three-step time-splitting method (e.g. Karniadakis *et al.* , 1991). The spectral-element method is described in detail in Karniadakis & Sherwin (1999). The present implementation of the method provides second-order temporal accuracy and high-order spatial accuracy. Karniadakis & Sherwin (1999) have shown that the method achieves exponential convergence for problems with 'smooth' solutions.

Discussion of the spatial discretisation and the time-splitting method will now follow. The spatial derivatives in equations 3.3 are discretised using the spectral element method (see §3.3.1) and the time derivatives are treated with a three-step splitting scheme (see §3.3.2).

3.3.1 Spatial Discretisation

The computational code uses a well-documented spectral-element method for the spatial discretisation of the derivatives in equations 3.3. A brief description of the use of the integration used within each computational element is given here. For more information see Blackburn & Lopez (2002) and Tomboulides & Orszag (2000).

The axisymmetric computational domain is discretised with quadrilateral elements. Gauss-Lobatto-Legendre quadrature is employed to integrate within each element, giving spectral convergence characteristics. According to Karniadakis & Sherwin (1999), the Gauss-Lobatto-Legendre quadrature points are the roots of the equation

$$(1 - \xi^2)P_m(\xi) = 0 \text{ where } -1 \leq \xi \leq 1. \tag{3.5}$$

An expression for the Legendre polynomial P_m of order m is given using *Rodrigues's formula* (see Kreyszig, 1993) as

$$P_m = \frac{1}{2^m m!} \frac{\mathrm{d}^m}{\mathrm{d}\xi^m} (\xi^2 - 1)^m \text{ where } m = 0, 1, 2, ... \tag{3.6}$$

The Gauss-Lobatto-Legendre quadrature weighting coefficients are given by

$$w_j = \frac{2}{m(m+1)} \frac{1}{[P_m(x_j)]^2} \text{ where } j = 0, 1, 2, ..., m. \tag{3.7}$$

The weighting coefficients and the quadrature points allow the integrals given by the method of weighted residuals to be accurately determined using the Gauss-Lobatto-Legendre quadrature in two-dimensions.

Gauss-Lobatto-Legendre interpolants are also used for the elements along the axis of symmetry, where to avoid singularities as $r \to 0$ the singular terms in the equations are set to zero. This condition uses the assumption that variables approach zero faster than r^2 as $r \to 0$ (see Blackburn & Lopez, 2002), retaining the efficiency and convergence characteristics in axisymmetric domains.

3.3.2   The Time-Splitting Method

The three part time-splitting method splits the Navier-Stokes equations into three separately solvable sub-steps: the non-linear convective step, pressure correction step and the diffusion step. An overview of these steps, as adapted from Karniadakis *et al.* (1991), will now be given. Details of time-splitting methods can be found in Karniadakis *et al.* (1991).

For the following analysis, let the linear and non-linear terms in equation 3.3 be

$$\mathbf{L}(\mathbf{u}) = \nabla^2 \mathbf{u} \tag{3.8}$$

and

$$\mathbf{N}(\mathbf{u}) = -(\mathbf{u} \cdot \nabla)\mathbf{u}, \tag{3.9}$$

respectively. The time-integration from t_n to t_{n+1} is defined as

$$\mathbf{u}^{n+1} - \mathbf{u}^n = -\int_{t_n}^{t_{n+1}} \nabla p \mathrm{d}t + \nu \int_{t_n}^{t_{n+1}} \mathbf{L}(\mathbf{u}) \mathrm{d}t + \int_{t_n}^{t_{n+1}} \mathbf{N}(\mathbf{u}) \mathrm{d}t \tag{3.10}$$

The solution to the semi-discrete system described above is obtained by splitting the above in relation to the time step, so that three sub-steps are as follows:

- Step 1 - Integrate the non-linear term forward in time using a Adams-Bashforth scheme

$$\hat{\mathbf{u}} - \mathbf{u}^n = \int_{t_n}^{t_{n+1}} \mathbf{N}(\mathbf{u}) \mathrm{d}t \simeq \delta t \cdot \sum_{q=0}^{J_e-1} \alpha_q \mathbf{N}(\mathbf{u}^{n-q}) \tag{3.11}$$

  where α_q are appropriately chosen weights and $\hat{\mathbf{u}}$ is an intermediate velocity field. At this step no boundary conditions are applied and $\hat{\mathbf{u}}$ is solved at each nodal point on the entire domain.

  The weightings (α_q) of the Adams-Bashforth (and the Adams-Moulton β_q) schemes are given in table 3.1 for variety of orders J. Typically the third-order scheme is used.

- Step 2 - The pressure correction step, where the second intermediate velocity field $\hat{\hat{\mathbf{u}}}$ is solved for using

$$\frac{\hat{\hat{\mathbf{u}}} - \hat{\mathbf{u}}}{\delta t} = -\nabla \bar{p}^{n+1} \tag{3.12}$$

  where $\bar{p}^{n+1}$ is the scalar pressure field that ensures the final velocity is incompressible at t_{n+1} and is related to the pressure term through

J	α_0	α_1	α_2	β_0	β_1	β_2
1	1					
2	3/2	-1/2		1/2	1/2	
3	23/12	-16/12	5/12	5/12	8/12	-1/12

Table 3.1: Weighting factors of the Adams-Bashforth (α) and the Adams-Moulton (β) schemes (from Chapra & Canale (1998))

$$\int_{t_n}^{t_{n+1}} \nabla p \, \mathrm{d}t = \delta t \nabla \bar{p}^{n+1} \qquad (3.13)$$

The Poisson equation for the pressure term can be found by taking the divergence of equation 3.12 and forcing continuity in the $\hat{\hat{\mathbf{u}}}$ velocity field, giving

$$\nabla^2 \bar{p}^{n+1} = \frac{1}{\delta t} \cdot \nabla \hat{\mathbf{u}} \qquad (3.14)$$

Here the pressure boundary condition must be chosen to satisfy the Navier-Stokes equations at the boundaries; Karniadakis *et al.* (1991) suggested the following Neumann boundary condition

$$\frac{\partial \bar{p}^{n+1}}{\partial n} = \mathbf{n} \cdot \sum_{q=0}^{j-1} \beta_q \left[\mathbf{N}(\mathbf{u}^{n-q}) - \frac{1}{Re} \nabla \times \nabla \times \mathbf{u}^{n-q} \right] \text{ on } \Gamma \qquad (3.15)$$

where Γ is the boundary surface, $\mathbf{n}$ is the unit normal to the boundary and β_q are the weightings of the Adams-Moulton scheme.

According to Karniadakis *et al.* (1991), the time-advancement scheme can only be one order greater than the order used in the extrapolation of the pressure boundary condition, and since the scheme requires at least first-order accurate boundary conditions, this gives second-order

accuracy in the velocity boundary conditions. Higher-order boundary conditions can be used for the pressure fields, to the detriment of stability.

The Poisson equation for the pressure term and the Helmholtz equations for the viscous terms result in linear matrix problems. The matrices can be inverted as a pre-processing step leaving the sub-steps to be carried out through matrix-vector multiplications.

- Step 3 - Integrate the diffusion term in time using

$$\frac{\mathbf{u}^{n+1} - \hat{\hat{\mathbf{u}}}}{\delta t} = \frac{1}{Re}\mathbf{L}(\mathbf{u}) \tag{3.16}$$

which is solved implicitly using the second-order Crank-Nicholson scheme with the theta scheme modification to prevent short wavelength oscillation, resulting in a Helmholtz equation that can be solved by matrix inversion. The boundary conditions are imposed upon $\mathbf{u}^{n+1}$ and since $\hat{\hat{\mathbf{u}}}$ is chosen to be divergence free, $\mathbf{u}^{n+1}$ is also divergence free.

3.3.3   The Computational Grid

The above numerical scheme is applied to all elements on the computational grid that encompasses the axisymmetric geometry shown in the physical model. A relatively simple computational domain was employed in the majority of the calculations; having no protruding nozzle and a simplified outlet condition. The grid can be seen in figure 3.3. As the computational code is set up to have the axis of symmetry in the same direction as spatially horizontal x axis, the domain is rotated by 90° anticlockwise to the physical model.

The inlet is located at the bottom left of the computational domain, the outlet at the right, the outer wall at the top and the axis of symmetry at the bottom. The majority of the flow is left to right. The axis of symmetry corresponds to the z coordinate axis at $r/R = 0$. The domain height is $r/R = 10$ (from the axis to the outer wall) and the length of the computational domain is $z/R = 56$.

The grid features compression of the elements toward the shear layer and the centreline of the jet, as well as compression towards the nozzle in the radial and axial directions. For simplicity, no expansion elements were used; hence there are elements with high aspect ratios (in excess of 7:1) in non-critical flow areas.

The computational boundaries are set as follows: At the nozzle (the computational inlet), the velocity components are specified. The radial velocity component is always set to zero. Along the centreline, the azimuthal and radial components, and the normal derivative of the axial velocity, are set to zero. The no-slip condition is imposed at the adjacent wall boundary, and the slip condition at the outer-wall. At the outlet, the normal derivative of the velocity is set to zero.
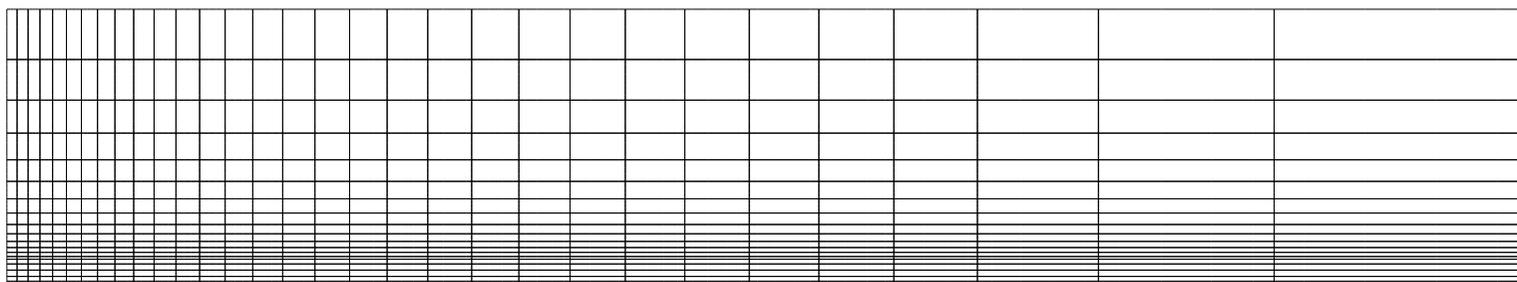
Figure 3.3: Computational mesh used in the simulations showing macro mesh elements and the location of the boundary types.

3.4 Model Validation

This section presents the model validation, including the mesh resolution and time-step independence studies, followed by boundary condition independence for the adjacent wall, the outer wall and the viscous sponge region.

3.4.1 Independence of Grid Resolution

A numerical simulation should have sufficient resolution to limit the discretisation errors to an acceptable level. When the grid is fine enough such that the discretisation error falls below a maximum allowable tolerance, then the solution is deemed to be *grid independent*. Grid independence is tested in practice by performing the same simulation at increasingly higher mesh resolutions and comparing the results.

Here, the independence of the solution to grid resolution will be demonstrated at $Re \approx 350$, $S = 1.50$ with an increasing number of interpolation nodes for a single grid as seen in §3.3.3. Since the spectral element method shows spectral convergence characteristics, this method of increasing the grid resolution should yield a converged solution for increasing interpolation nodes (n). Six grid resolutions ($\sqrt{n} = 4$, 5, 6, 7 & 8) were tested for the effect on the axial and azimuthal velocities at selected points.

Figure 3.4 shows contours of azimuthal velocity for a large bubble simulated at the flow parameter $Re \approx 350$ and $S = 1.50$. The black boxes ($\blacksquare$) show the locations of two data probe locations at $z/R = 0.4$ & $r/R = 0.37$, and $z/R = 1.7$ & $r/R = 0.37$. These locations were chosen such that they were nodes of the macro-grid and therefore common for different internal element resolutions. Figure 3.5 shows the axial U and azimuthal W velocities at the two probe locations as a function of the interpolation order $\sqrt{n}$ for the

	Interp. Nodes ($\sqrt{n}$)				
	4	5	6	7	8
$z/R = 0.4$, $r/R = 0.37$	0.18	0.33	0.03	0.02	0.03
$z/R = 1.7$, $r/R = 0.37$	3.33	1.02	0.04	0.07	0.05

Table 3.2: % Difference in the axial velocity (U) for two probe locations relative to the velocity for the $\sqrt{n} = 9$ solution. This data are also plotted in figure 3.5.
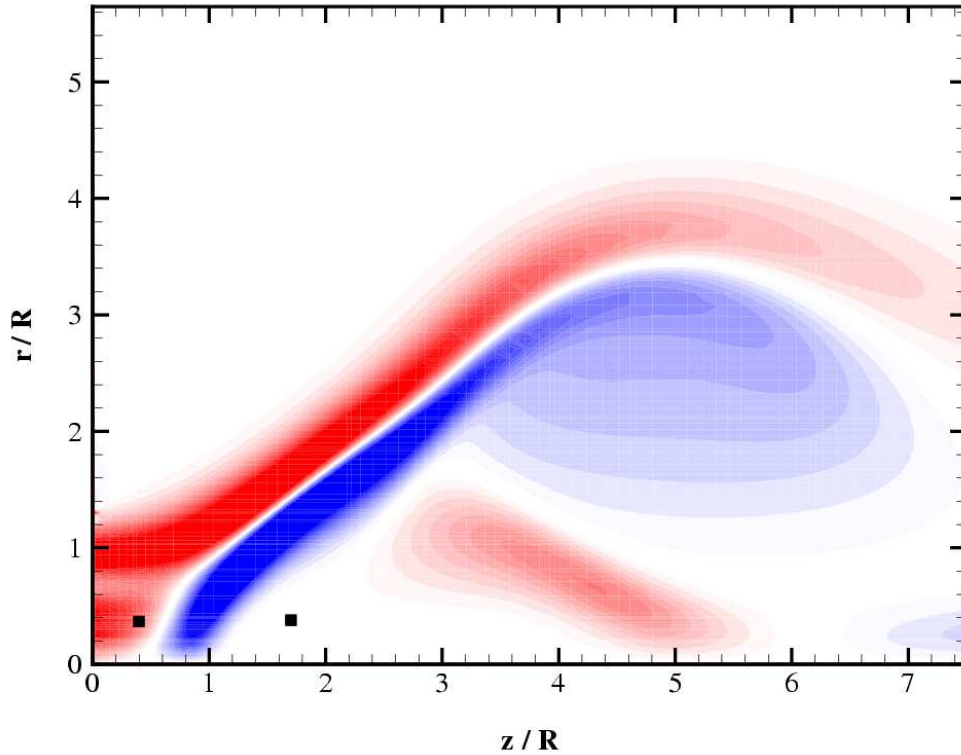

Figure 3.4: Contours of azimuthal vorticity (red and blue indicate positive and negative respectively) for a large bubble breakdown at $Re \approx 350$, $S = 1.50$. The boxes (■) indicate the two probe locations with coordinates $z/R = 0.4$, $r/R = 0.37$ and $z/R = 1.7$, $r/R = 0.37$ from left to right respectively.
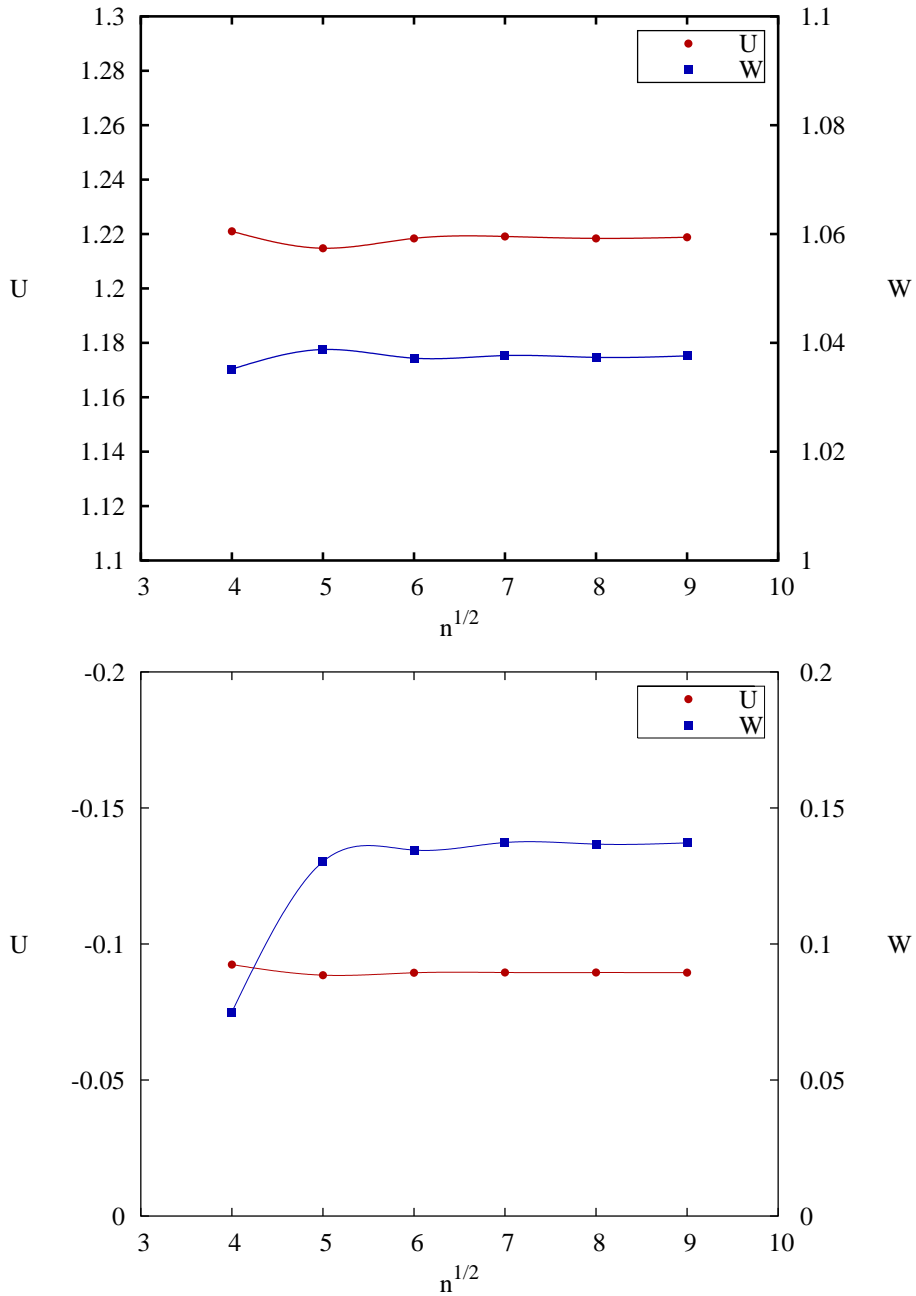
Figure 3.5: Axial (U) and Azimuthal (W) velocities at $\tau = 20$ for a series of increasing interpolation nodes n used to alter the grid resolution. The simulations are at $Re \approx 350$ and $S = 1.50$. The top graph gives the velocities at the location $z/R = 0.4$, $r/R = 0.37$ and the bottom graph gives the velocities at $z/R = 1.7$, $r/R = 0.37$ as shown in figure 3.4.

two probe locations (upper and lower). Here, as the grid resolution increases, the velocity at each probe location asymptotes to a grid independent value. Table 3.2 gives the percentage difference in the axial velocity at the two probe locations for the $\sqrt{n} = 4, 5, 6, 7$ & 8 resolutions as calculated relative to the $\sqrt{n} = 9$ case. Here, it is clear that the axial velocities at both probe locations are within 1% of the final converged case after the resolution increases past $\sqrt{n} \geq 6$, indicating that the $\sqrt{n} = 6$ resolution is sufficiently grid independent for accurate simulations. Henceforth, the number of interpolation nodes used in each simulation will be $n = 36$.

3.4.2 Independence of Time-Step

It is important to show that any simulations of time-dependent flows are independent of the temporal discretisation. Therefore, a time-step independence test is required. This is more important where the dynamics of the fluid flow are important but less so when using time-dependent simulations to capture a time-independent phenomena, as is the case in this thesis; the critical swirl ratio is reasonably independent of the unsteady behaviour of the swirling jet. However, note that even for steady state calculations there is an associated splitting error, dependent on the time-step.

Figure 3.6 shows the results of the time-step independence test, the top graph showing axial velocities and the bottom showing radial velocities. Each graph contains raw velocity data for two time-steps and three probe locations (see 3.7). The two time-steps tested were $\delta t = 0.0005$ and $\delta t = 0.00025$, the former being the time-step used in the simulations, and the latter is a more accurate time step. The simulations were performed for the initial 40 time units of a simulation of an unsteady cone type vortex breakdown. As can be seen from the two graphs, the halving of the time-step to $\delta t = 0.00025$ has

caused no graphical variation in the solution. The time-step of $\delta t = 0.0005$ is therefore deemed to be sufficient to temporally resolve the simulated flows.

3.4.3   Treatment of Outlet

Preliminary simulations revealed a significant technical problem with numerically modelling jets; the problem of how to define the outlet boundary conditions to give a stable solution. When a jet is impulsively started, a vortex ring is propagated downstream. When this vortex ring reaches the outlet, the strong vorticity causes fluid to re-enter the domain. Since only simple Neumann boundary conditions are implemented in the current code $(\mathrm{d}\mathbf{u}/\mathrm{d}\mathbf{n} = 0)$, only flows out of the domain are possible. Recirculation causes the problem to be ill-posed and numerically unstable.

An effective solution is to include a region before the outlet as a *viscous sponge*. A viscous sponge is the numerical equivalent to a perforated plate or a sponge, in an experimental rig. It has the effect of 'smoothing' out velocity gradients and creating a constant flow across the domain. This is achieved numerically through the use of a region near the outlet where the effective Reynolds number Re_2 is decreased significantly.

Firstly, the effective Reynolds number (Re_2) of the viscous sponge must be chosen such that it performs the required role. Figure 3.8 shows the results of the effective Reynolds number in the viscous sponge region on the velocity at the outlet of the computational domain. Three Reynolds numbers were tested, all at least a factor of 10 times smaller than the Reynolds number of the base flow. The base flow was a jet with no azimuthal velocity and the simulation was allowed to run until after the starting vortex had reached the outlet. For the $Re_2 = 50$ and $Re_2 = 25$ cases, the velocity profiles show the flow reversal at the outlet that causes numerical divergence problems.
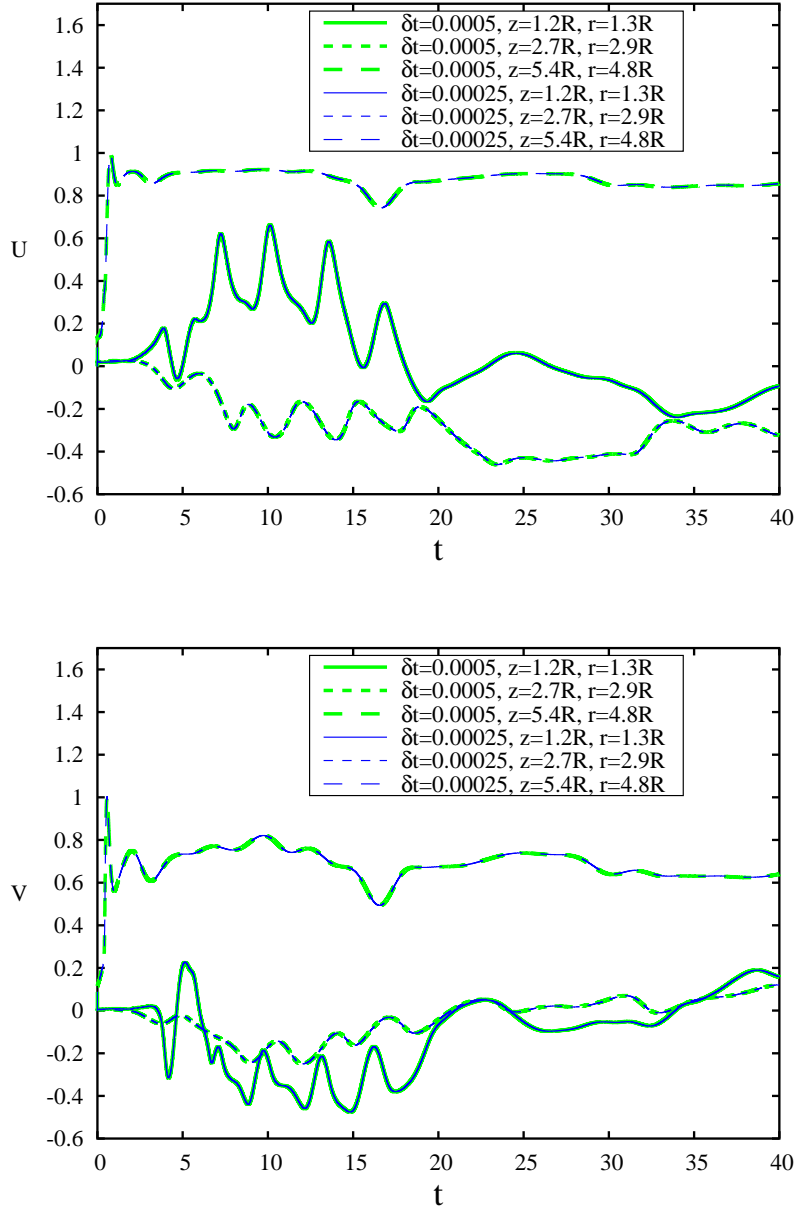
Figure 3.6: Results of time-step check for two time-steps $\delta t = 0.0005$ and $\delta t = 0.00025$ showing that the solution for $\delta t = 0.0005$ is time-step independent. Axial velocities (top) and radial velocities (bottom), as a function of time for three probe locations as shown in figure 3.7.
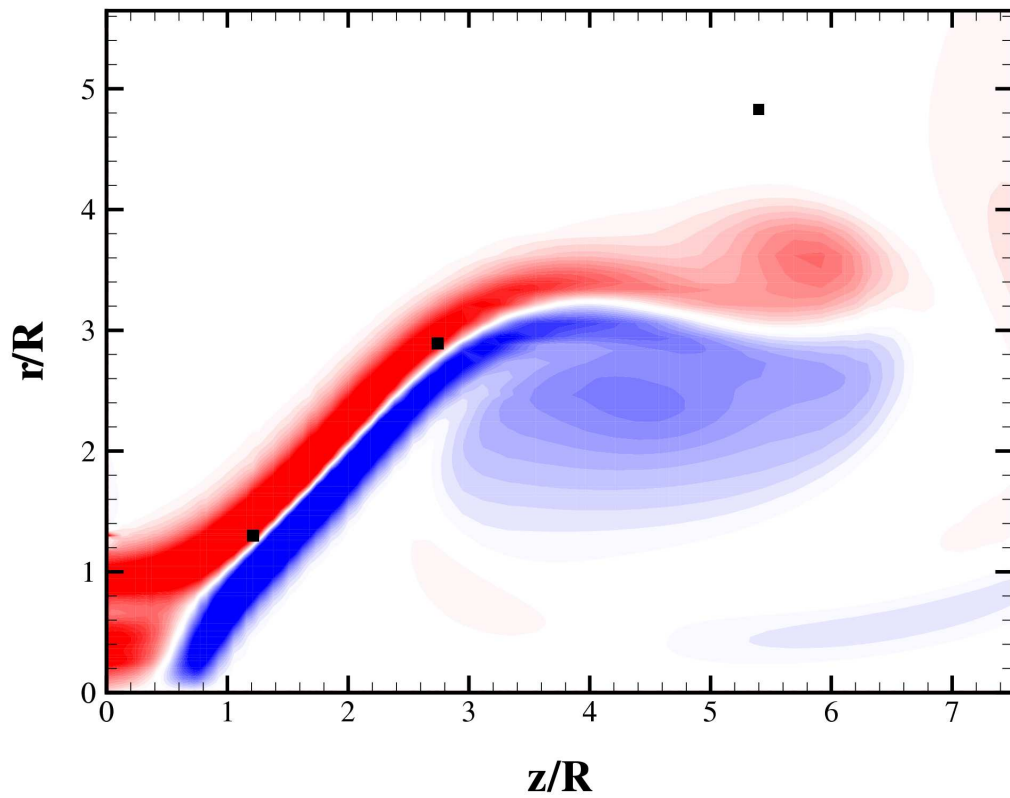
Figure 3.7: The three probe locations (marked as ■) used in the time-step independence test. Contours of azimuthal vorticity shows the vortex breakdown cone at $t = 10$ (red is positive and the contours are at 31 intervals between $-10 < \omega_\theta < 10$).
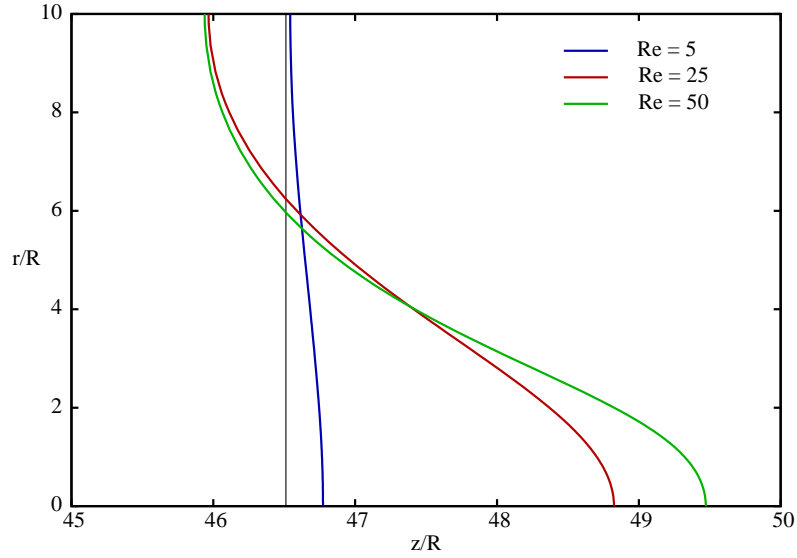
Figure 3.8: Axial velocity profiles at the computational domain showing the effect of decreasing the effective Reynolds number within the viscous sponge region.

However, the velocity profile at the outlet for each simulation shows that the velocity magnitudes are decreasing. The $Re_2 = 5$ case show that the velocity through the outlet is positive for all r. Based on this evidence, the simulations henceforth use a viscosity of five times this value, i.e. $Re_2 = 1$. A better visualisation of the effect of adding the viscous sponge is shown in figure 3.9, where the strong positive axial velocities (red contours) are quickly spread and dissipated upon entering the viscous region at $z/R = 32$.

Simulations from hereon utilise a viscous sponge region in the last 3 macro-element columns with an effective Reynolds number of $Re = 1$.
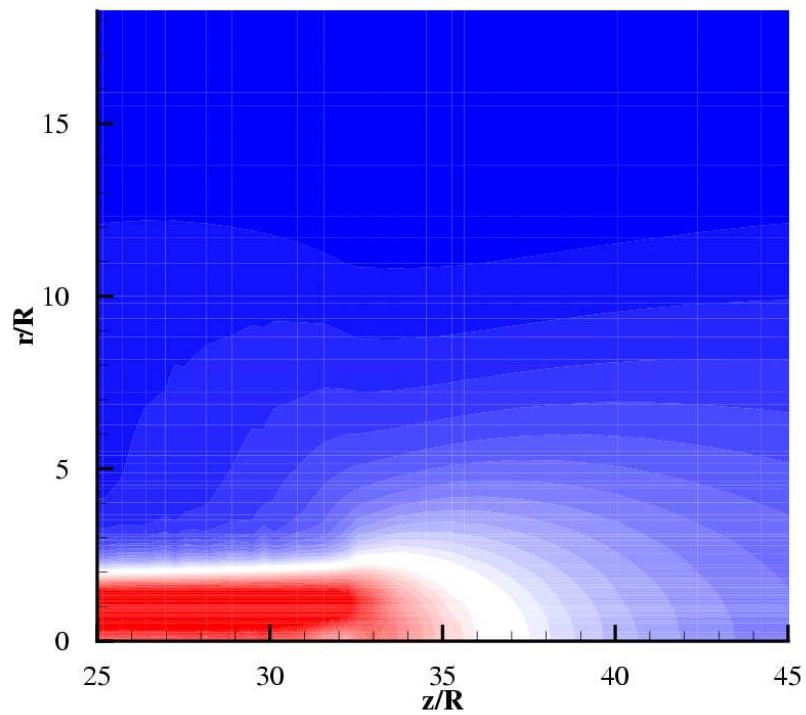
Figure 3.9: The diffusive effect that the viscous sponge has on the axial velocity shown here in contours. Rapid spreading of the axial velocity radially can be seen when the jet passes the point $z/R = 32$.
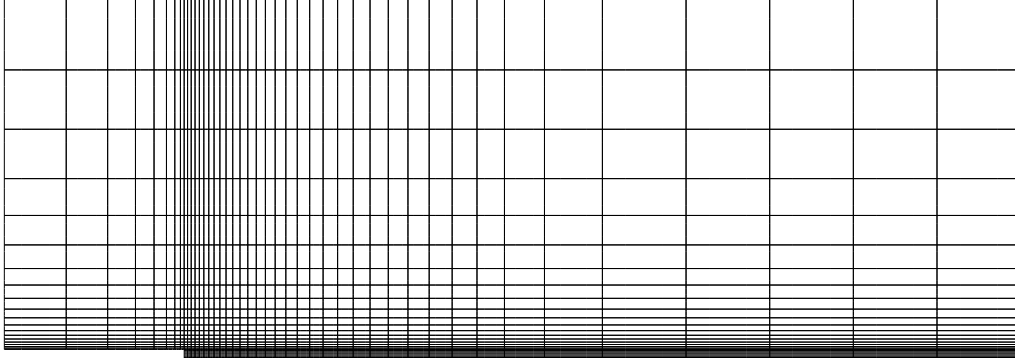
Figure 3.10: The mesh used to test the effect of the boundaries on the critical swirl ratio for vortex breakdown.

3.4.4 Independence of Boundary Location

The current simulations are ideally modelling a swirling jet as it emerges into a stagnant region of unbounded dimensions. However, for economy of computational time, we would like to limit the domain size. These limits should be located where they cause little different. Here, a boundary location independence test is presented. The grid used in this study is widely different to that which is used throughout the simulations. There is a nozzle of length $z/R = 20$, the outer wall has been moved to a radial location of $r/R = 40$ and the outlet has been moved downstream to $z/R = 93$. The grid is shown in figure 3.10.

The result of a comparative study on the critical swirl ratio for vortex breakdown in this grid and in the grid used throughout the simulations (see 3.3) gives a critical swirl ratio for vortex breakdown difference of $\delta S_c \approx 3\%$. This is an acceptable difference considering the significant reduction in computational time and memory required to compute the solutions on the more confined grid. Figure 3.11 shows a vortex breakdown bubble at
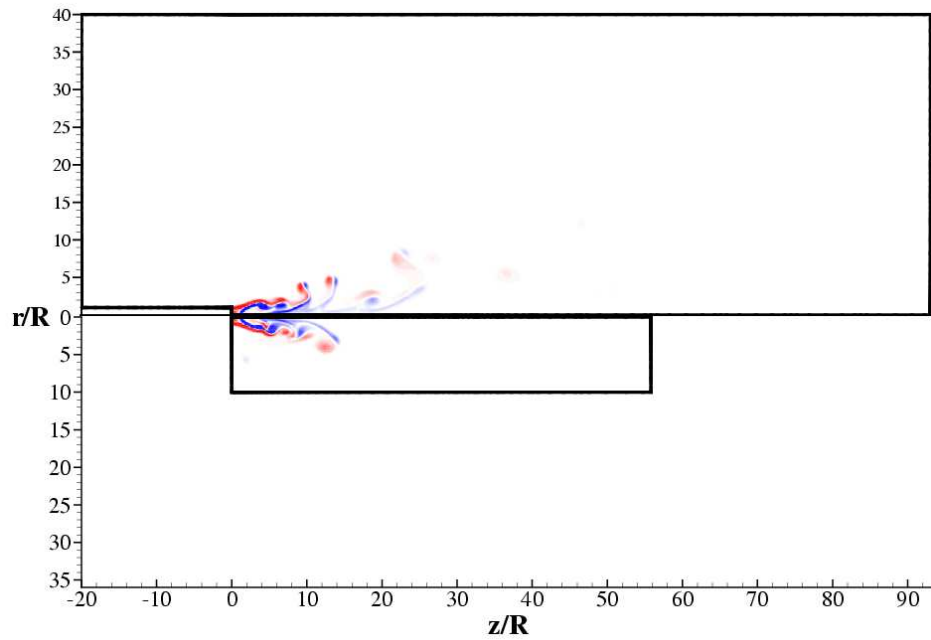
Figure 3.11: A comparison of the solution of an unsteady bubble type vortex breakdown at $Re \approx 590$, $S = 1.38$ within the large mesh tested here and the normal mesh used throughout the simulations. The respective computational geometries are shown as black lines.

$Re \approx 590$, $S = 1.38$ as simulated on the larger mesh and the smaller mesh (shown beneath the centreline). The computational domains are included as solid black lines to give some idea of the difference in scale of the two cases.

3.4.5 Comparison to Experimental studies

This section presents some comparisons between the experimental flows as measured and visualised by Billant *et al.* (1998) and the simulated flows presented herein. There are two major differences between the simulations and the experiments: the assumption of axisymmetry imposed on the mathematical model, and the differences in flow behaviour at particular Re, S pairs. Despite the absence of three-dimensionality, the axisymmetric model shows excellent agreement, but not necessarily at the same Re, S pairs. More details regarding the flow states achieved in the Re, S parameter space are given in §6.

A comparison of axial and azimuthal velocity contours is given in figure 3.12, with the axial velocity contours in the upper image and the azimuthal in the lower. In each image are the experimental contours from Billant *et al.* (1998) given above the centreline – which runs through the centre of each image – and the simulated contours given below the centreline. The experimental parameters were $Re = 687$ & $S = 1.4$, while the numerical parameters needed to achieve this flow were $Re \approx 400$ & $S = 1.4$. The contours have been matched according to the location of the forward stagnation point. Note that in the present simulations, the stagnation point location consistently sat closer to the nozzle outlet than seen in the experimental studies of Billant *et al.*

The majority of the flow structures seen in the experiments are also seen in the simulations. In the contours of axial velocity given in the upper image, there is a region of recirculation – seen as reversed flows and hence dashed contour lines – and a region near the centreline where the velocity switches once again to positive, albeit smaller and slower in the simulations. The contours of azimuthal vorticity also show remarkable similarity apart from

Figure 3.12: Axial (above) and azimuthal (below) velocity contours as measured by Billant *et al.* (1998) at $Re = 687$, $S = 1.4$ (upper half), and compared to contours from simulations at $Re = 400$, $S = 1.4$ (lower half). The flow direction is left to right and the dashed lines represent contours of negative velocity. The contours of Billant *et al.* are time averaged, whereas the contours of the simulations are instantaneous.

the slightly more elongated shape in the simulated contours.

The major difference between the simulation of the bubble and the experimental bubble is the presence of the rear stagnation point. The experimental contours show this stagnation point just behind the bubble on the centreline. The simulations however have no such point but a core region of reversed flow. Figure 3.13 shows one situation where there is also the absence of a stagnation point in the experimental flow. Here, an instantaneous image of fluorescein dye visualisation of a bubble from Billant *et al.* (1998) is compared to contours of azimuthal vorticity and streamlines of a similar simulation. Blue, white and red contours indicate positive, zero and negative levels of instantaneous vorticity. Comparing the flow fields in the experimental and numerical flows shows remarkable similarity between the open wake structure. The asymmetry of the full experimental bubble (not shown here) means that only one side of the bubble may be open, while the opposite side may be closed.

A comparison of the cone state of breakdown shows strong similarity despite the lack of asymmetry in the numerical simulations. Billant *et al.* gave a series of fluorescein dye visualisations roughly outlining a full period of oscillation in the shear layers of the cone type (figure 3.14 upper). When considering only the upper halves of each image – from the centreline of the nozzle and up – then we can compare this flow with an axisymmetric simulation. Figure 3.14 (lower) shows a series of images from a simulation that show similarity in the oscillation of the conical wake. Some of the main differences between the experiments and the simulations (excluding the lack of three-dimensionality) are as follows. The placing of the stagnation point in the simulations is within $z/R = 2$ of the nozzle outlet, whereas in the experiments it can be placed further downstream. Also the shear layer of
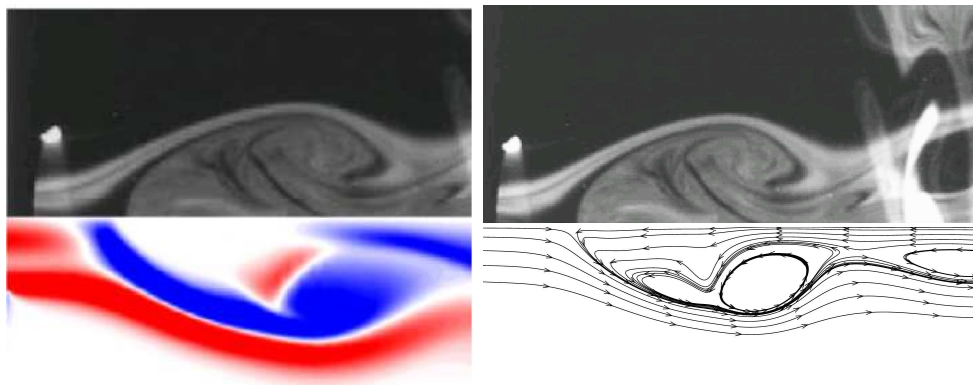
Figure 3.13: Comparison of bubble breakdown using experimental fluorescein dye visualisations (from Billant *et al.*, 1998) and simulated contours of azimuthal vorticity (lower left), where blue, white and red indicate positive, zero and negative vorticity levels respectively. The lower right half shows streamlines of the simulated bubble. Both the experiment and the simulation are at $Re \approx 600$ and the swirl ratios are $S = 1.42$ and $S = 1.32$ respectively.

the cone tends to travel further from the centreline before rolling up into coherent vortex rings – this effect may be due to the enforced axisymmetry. The swirl ratio at which conical vortex breakdown is achieved is generally higher than that of the bubble at most Reynolds numbers. This discrepancy is expanded on in §6.

A more detailed comparison of the shedding of the cone is shown in figure 3.15. Here, the top half of the third image of figure 3.14 upper (see numerals on each image) has been compared to contours of azimuthal vorticity of an unsteady cone at $Re \approx 600$ & $S = 1.45$, shown below the centreline. The comparison shows remarkable similarity in all but the location of the stagnation point relative to the nozzle outlet; here the stagnation point locations are matched. The contours of azimuthal vorticity are given in blue, white and red indicating positive, zero and negative vorticity respectively. The replication between the shear-layer shedding behaviour is simulated well, but also the internal dynamics of the cone are captured; The dye layer beneath the main ring vortex is evident in the simulation by a region of negative (red) vorticity.

Figure 3.16 shows another comparison of the current simulations to the experimental results of Billant *et al.* (1998). The lower half of the third image of figure 3.14 upper is shown here compared to in-plane velocity vectors (left) and streamlines (right). In this case, the simulations predict a large recirculation region as the main vortex ring, which may be seen in the fluorescein dye visualisation but is unclear. More interesting is the similarity seen in the dye visualisations and the streamlines where small internal recirculation picked out by the manually placed streamlines are reflected as regions of low dye concentrations.
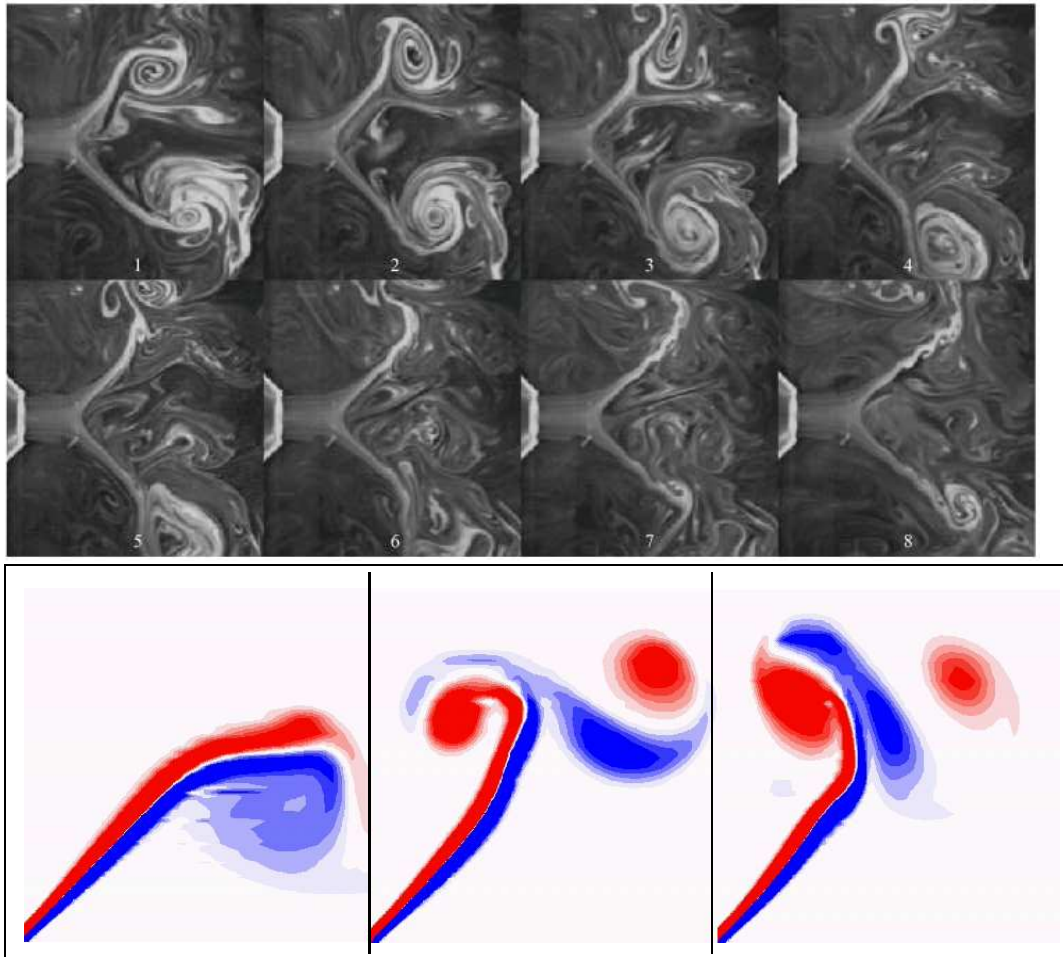
Figure 3.14: The set of images given in the upper image show approximately one period of dynamic behaviour of a cone type vortex breakdown at $Re = 626$ & $S = 1.31$. The nozzle can be seen at the left and the flow is visualised with fluorescein and a diametric laser sheet. Reproduced from Billant *et al.* (1998). The image below are a series of oscillations observed in the simulations of a cone $Re \approx 1000$ & $S = 1.45$. The flow is from left to right.
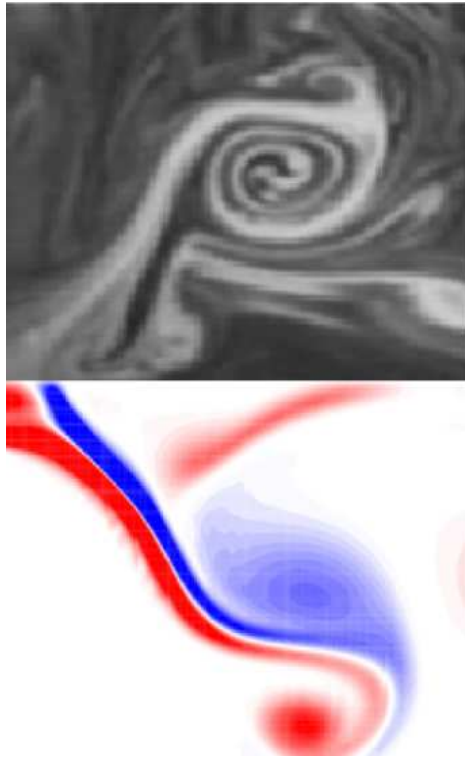
Figure 3.15: Comparison of cone breakdown using experimental dye visual-
isations (from Billant *et al.* , 1998) and simulated contours of azimuthal
vorticity (lower half), where blue, white and red indicate positive, zero and
negative vorticity levels respectively. Both the experiment and the simulation
are at $Re \approx 600$ and the swirl ratios are $S = 1.31$ and $S = 1.45$ respectively.
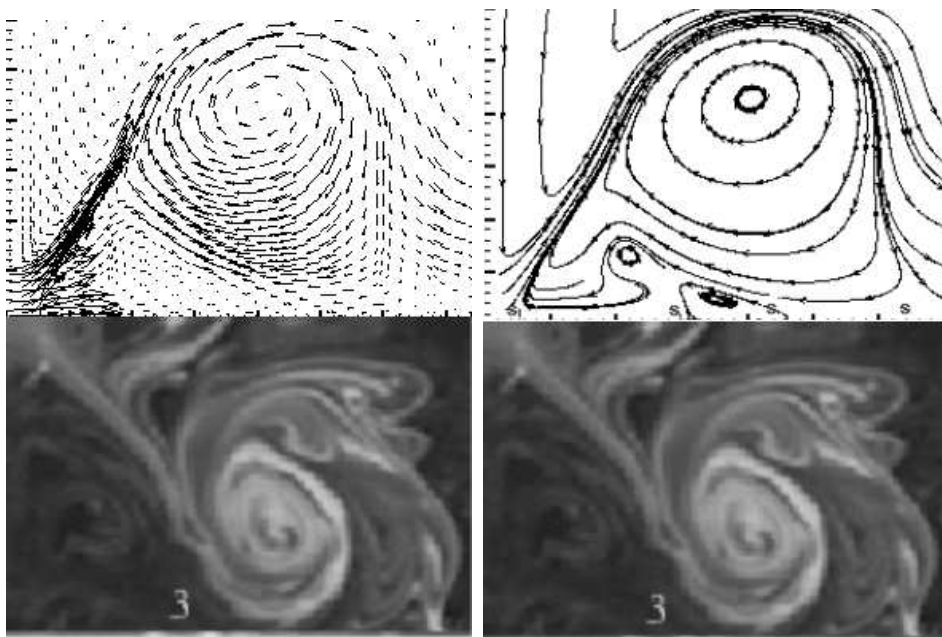
Figure 3.16: Comparison of cone breakdown using in-plane velocity vectors (left) and manually placed streamlines (right) mirrored with fluorescein dye visualisation of an experiment.

Chapter 4

Observations and Visualisation

The term *vortex breakdown* describes a wide variety of breakdown types, ranging from the near-symmetric large bubbles observed in closed cylinders with rotating lids, to highly asymmetric spiral types observed in pipe and delta wing flows. The present simulations show that, independent of the exact type of vortex breakdown seen, there are some common dynamics. All forms of vortex breakdown are characterised by some sort of strong disruption to the axial flow (usually culminating in the formation of a stagnation point on the centreline), expansion of the vortex core away from the centreline and some form of recirculation or reversed flow region.

In this Section, each type of vortex breakdown observed in the simulated unconfined swirling jet, is described. The two main types of vortex breakdown seen were the bubble and the cone; both axisymmetric due to the modelling assumptions (see §3.1). However, there were interesting combinations of the two, dubbed here as 'hybrid'. Depending on the flow parameters, quasi-steady and unsteady variants of the bubble and cone states were observed.

Initially, some explanation of the dynamics of the swirling jet preceding

vortex breakdown is necessary.

4.1 Pre-Breakdown Dynamics

Vortex breakdown occurs reasonably suddenly in a vortex core, often with little or no warning signs. Perhaps the best way of determining the state of a vortex core with respect to breakdown, is to observe the axial velocity. Vortex breakdown is usually preceded by significant deficit of the axial velocity, near the vortex centreline. A deficit usually becomes stronger at near critical swirl levels. This effect is shown in figure 4.1, where a simulated swirling jet at $Re = 175$ is shown with four different swirl ratios $S = 1.40,\ 1.42,\ 1.44\ \&\ 1.46$, from top to bottom respectively. Here, contours of axial velocity show positive, zero and negative velocities in red, white and blue respectively. The nozzle of the jet is located at $z/R = 0$ and spans the radial domain of $0 \leq r/R \leq 1$ and the flow is from left to right.

All images show the effects of spreading and widening of the shear layer with downstream distance. In the $S = 1.40$ case, the beginnings of a velocity defect on the centreline are evident as a decrease in velocity at $z/R \approx 5$. This is the first sign of the build up of a strong adverse pressure gradient leading to vortex breakdown. In the absence of swirl, the axial velocity of an idealised jet will always be greatest on the centreline. The stagnation on the centreline of the axial velocity is also observed as a switch of the azimuthal vorticity from positive to negative in the core region; a well known effect prior to vortex breakdown (see Özgören *et al.* , 2002).

With further increase in the swirl ratio from $S = 1.40$ to $S = 1.44$, the velocity defect increases relatively slowly, evident by the slight progression of the contour lines toward the nozzle. For the $S = 1.46$ case, the defect has
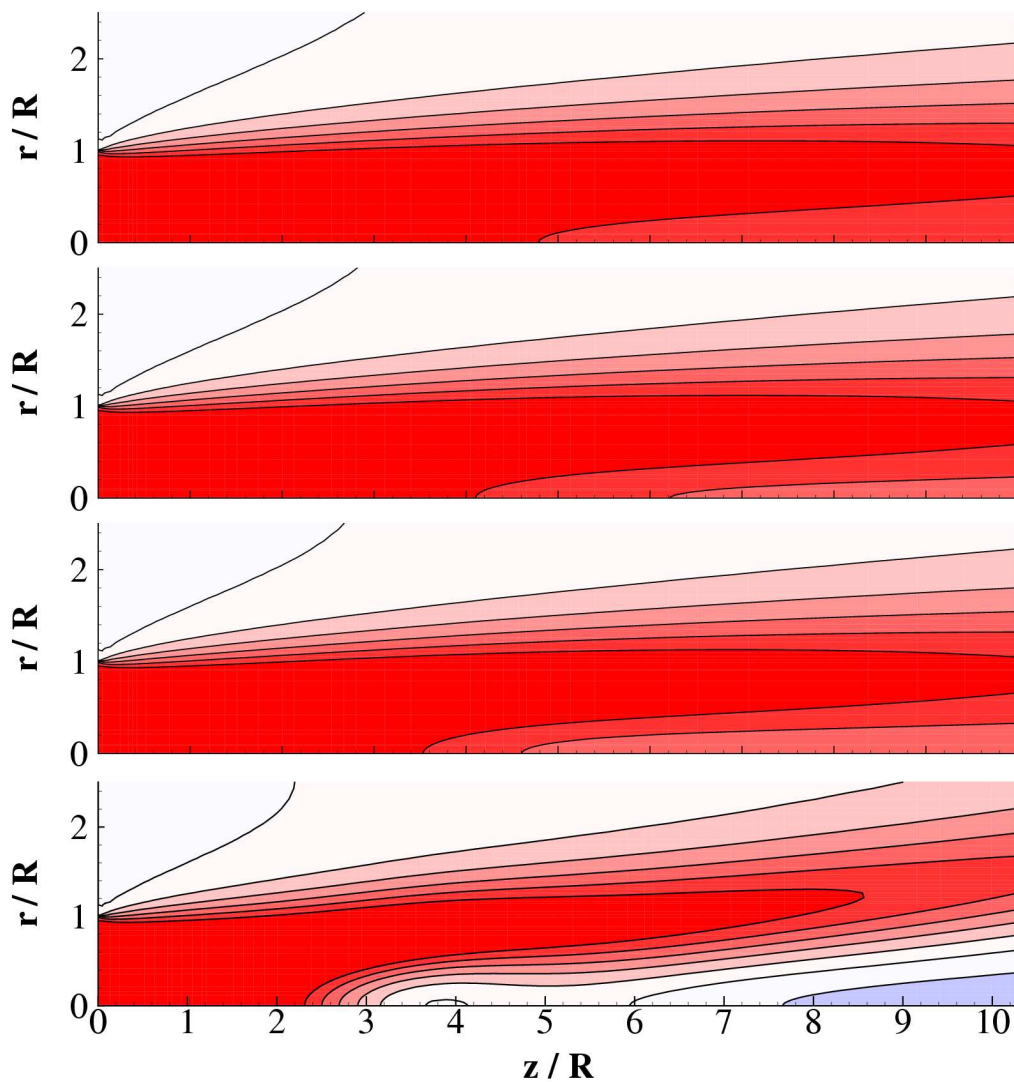
Figure 4.1: Contours of axial velocity for simulations at $Re = 175$ showing (from top to bottom) $S = 1.40$, 1.42, 1.44 & 1.46. The contours show 30 equispaced levels from $-1 \leq U \leq 1$ where red, white and blue are positive, zero and negative respectively. The flow is from left to right.
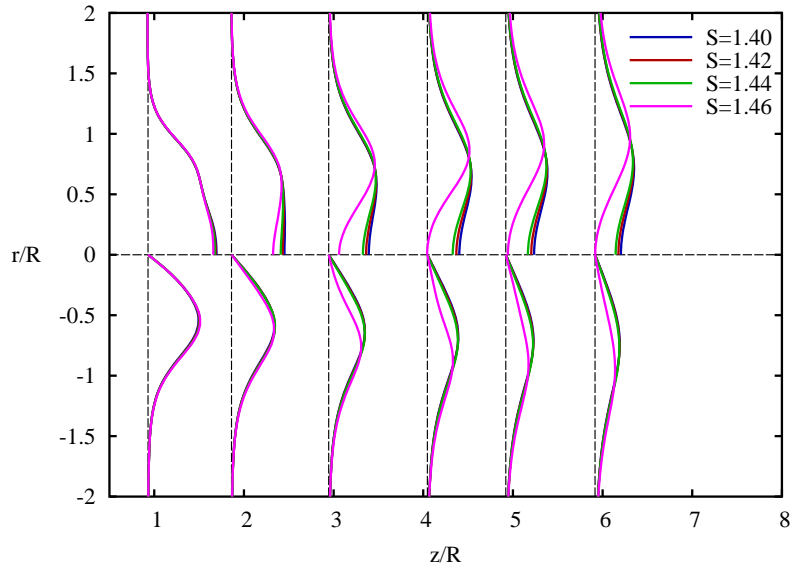
Figure 4.2: Profiles of axial and azimuthal velocity drawn above and below the axis $(r/R = 0)$ respectively, for four preliminary states to vortex breakdown at $Re = 175$. The velocity profiles are given for a variety of downstream axial locations indicated by the vertical dashed lines. The flow is from left to right.

jumped in size to become a complete stagnation (represented by the white contour level) and a slight recirculation (blue contours). Further increase in the swirl ratio leads to the growth of the stagnation and recirculation region into a recognisable vortex breakdown state. The swirl ratio at which the vortex breakdown state first occurs is referred to as the critical swirl ratio (S_c).

Figure 4.2 shows the rapid increase in the velocity defect at near-critical swirl ratios more clearly. Axial velocity profiles (above the axis) and azimuthal velocity profiles (below the axis) are shown for a variety of downstream locations (vertical dashed lines). The flow is from left to right and the nozzle is located at $-1 \leq r/R \leq 1$. The velocity profiles are of the flows

shown in figure 4.1. The rapid increase in the axial velocity deficit, occurring between $S = 1.44$ and $S = 1.46$, can be seen clearly at $z/R \geq 3$. For swirl ratios up to $S = 1.44$, the velocity profiles change very little with increases in swirl ratio.

4.2 The Small Bubble

Small bubbles are defined here as vortex breakdown bubbles that have a maximum expansion of $r/R \approx 2$, and are characterised by a single celled recirculation region. That is, there is only one ring vortex within the recirculation region. There are is usually only one real stagnation point located at the forward point of the bubble, however, due to its small size, the rear section often displays near stagnation point also. Due to the relatively small size of the recirculation region and the high velocities in the surrounding shear layer, the small bubble maintains reasonably high internal velocities.

Figure 4.3 shows four different parameters for the one example of a small bubble as predicted at the parameters $Re = 175$ & $S = 1.50$. Here, in-plane velocity vectors have been included below the centreline. Above the centreline are contours of azimuthal vorticity where red, white and blue indicate positive, zero and negative respectively. The swirling jet emerges from the nozzle located at $z/R = 0$ & $-1 \leq r/R \leq 1$.

The vorticity contours at the nozzle exit show a region $(0 \lesssim r/R \lesssim 0.6)$ with positive vorticity. In the case of a top-hat axial velocity profile, the vorticity in this region would be nearly zero. The vorticity present here is a result of the inclusion of the peak in the centreline velocity, resulting from the matching of the $S = 1.33$ axial velocity profile from Billant *et al.* (1998). The profile shape can be observed in the velocity vectors emerging from the
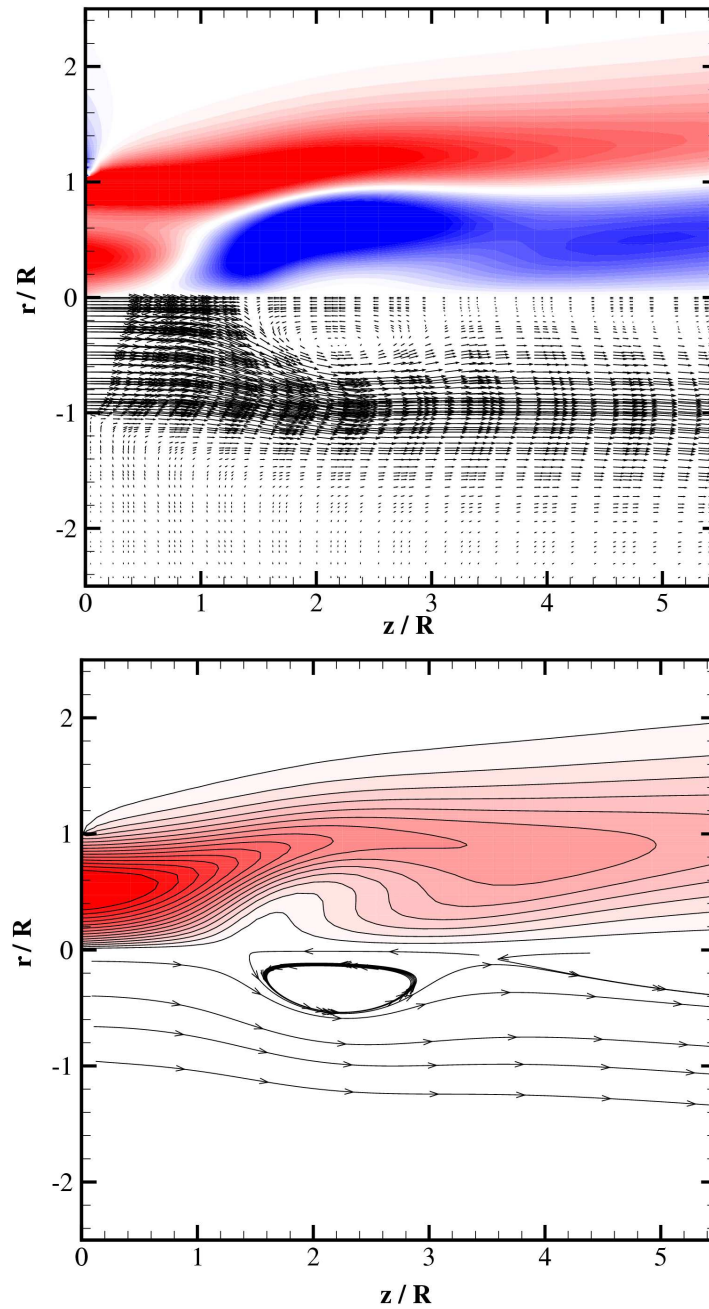
Figure 4.3: An example of a small bubble at $Re = 175$ & $S = 1.50$. For the upper image, contours of azimuthal vorticity with red, white and blue indicating positive, zero and negative vorticity respectively. Mirrored are the in-plane velocity vectors. For the lower image, contours of azimuthal velocity (W) are shown above the axis, with 16 equispaced levels from $0 \leq W \leq 1$ where red indicates positive azimuthal velocities. Mirrored are the streamlines placed to describe the flow topology best.
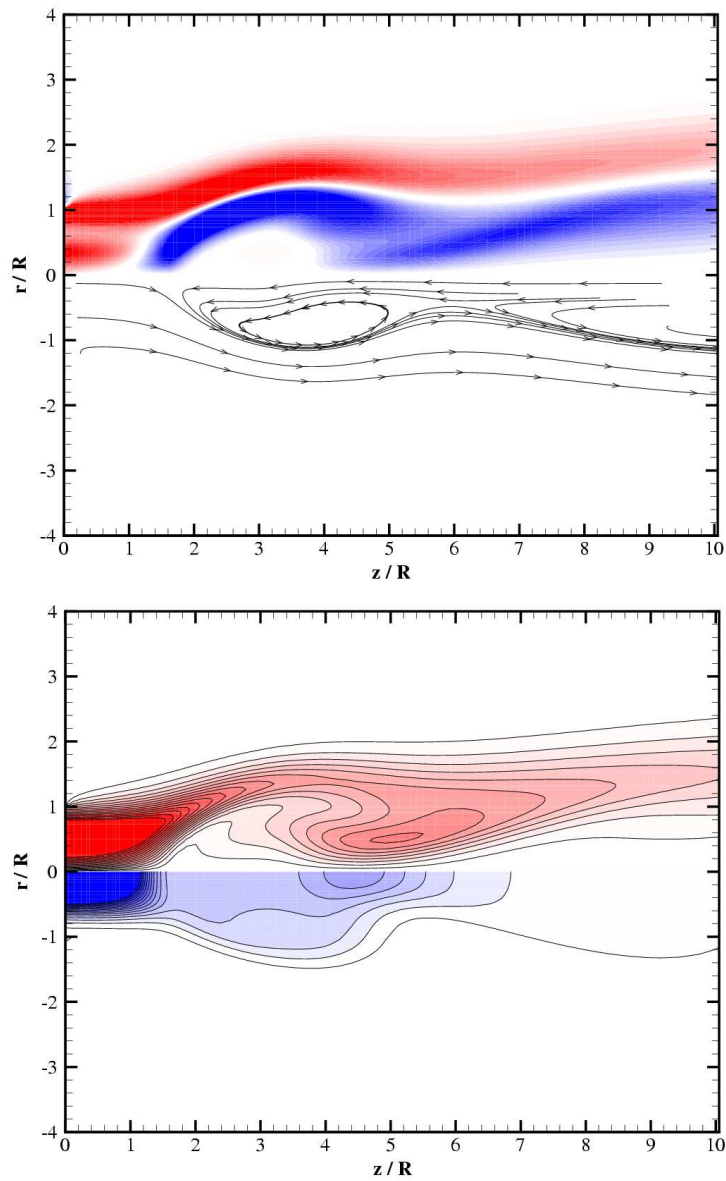
Figure 4.4: An example of a small bubble at $Re = 350$ & $S = 1.36$. For the upper image, contours of azimuthal vorticity with red, white and blue indicating positive, zero and negative vorticity respectively. Mirrored are placed streamlines. For the lower image, contours of azimuthal velocity (W) are shown above the axis, with 16 equispaced levels from $0 \leq W \leq 1$ where red indicates positive azimuthal velocities. Mirrored are contours of pressure, where blue and white indicate lower relative pressure and zero pressure respectively.

nozzle.

The axial velocity near the centreline slows quickly due to the strong adverse pressure gradient associated with vortex breakdown. This causes the peak to be flattened rapidly and the vorticity becomes zero at $z/R \approx 1.0$. After this point, the velocity is rapidly slowing on the centreline, leading to the switch in positive vorticity to negative (blue). Following the stagnation zone is a region of reversed flow surrounded by strong axial flow giving rise to more negative vorticity (see also §4.1). There is a region within the bubble near the centreline that has little or no azimuthal velocity due to nearly uniform reversed flow.

Most simulations of vortex breakdown presented in this thesis have showed a permanent open wake. That is, there is reversed flow on the axis and the absence of a rear stagnation point. The small bubble is the only case that has a near-stagnation point at the rear. In this case, there is a stagnation ring of very small radius located at $z/R = 3.4, r/R = 0.1$, however, the amount of fluid exchange occurring between the outside of the bubble and the bubble is negligible, such that the stagnation ring can be approximated as a stagnation point. The presence of a very small stagnation line at the rear of the bubble contributes to the dynamics of the small bubble, which tends to be quasi-steady; suffering less from rapid expansions, contractions and oscillations along the axis. These effects are linked to changes in volume of the bubble.

The lower image of figure 4.3 shows two alternative parameters; contours of azimuthal velocity (upper half) and streamlines mirrored below the axis. The contours of azimuthal velocity show the characteristic kink within the bubble region corresponding to the low azimuthal velocities within the bubble region. The streamlines show the small single celled recirculation region more

clearly, as well as the stagnation ring at the rear of the bubble.

Another example of a small bubble is given in figure 4.4 where the flow parameters are $Re = 350$ & $S = 1.36$. The upper image shows contours of azimuthal vorticity with the same contour levels as those shown in figure 4.3, with manually placed streamlines mirrored below the centreline. The lower image shows contours of azimuthal velocity (also the same contour levels as before), with contours of relative pressure mirrored below the centreline. Here, we can see that this bubble is slightly larger, and has an internal region near the forward stagnation point where there is very little azimuthal vorticity. The contours of pressure show the strong adverse pressure gradient leading up to the stagnation point (progression from deep blue to light blue) followed by internal flow with slightly lower pressure than the far field pressure. The fact that the stagnation pressure is lower than the far field pressure reflects the assumptions made in the analysis by (see §5.1 and Billant *et al.* , 1998). There is a region of lower pressure at the rear of the bubble due to the strong velocities in the vortex ring.

4.3 Unsteady Behaviour in Bubbles

For some cases (usually those with higher Reynolds number), the bubble state becomes unstable. An example of an unstable bubble type breakdown is shown in figure 4.5, where three instantaneous flow fields at $t = 100$, 110, & 130 are shown using contours of azimuthal vorticity – red, white and blue contours represent positive, zero and negative vorticity respectively. Here, the wake of a small bubble is shedding vortices, probably due to a similar instability to the Kelvin-Helmholtz shear layer instability. Surprisingly, the strong instability in the wake has little effect on the size or location of

the vortex breakdown bubble (for more details see §6).

4.4   The Large Bubble and Hybrid Bubble-Cone

Large bubbles and hybrid bubbles-cones are defined as vortex breakdown bubbles that have expansion $r/R \geq 2.0$ and that still contract back to the centreline to form a weak trailing vortex. They are characterised by more complex internal velocity fields and the absence of an approximate stagnation point in the wake. The large bubble is defined as the state where the flow is quasi-steady, whereas the hybrid bubble-cone case is a transient state seen in the oscillations of a vortex breakdown region between a classic conical breakdown (e.g. §4.5) and a more bubble like breakdown. The two are defined separately because their dynamical behaviour is quite different. As an instantaneous flow field, the two cases are practically the same, hence the discussion from hereon will refer to them as such unless the dynamics is being described

Figure 4.6 and 4.7 show two examples of the large bubble breakdown. In the upper images of each, contours of azimuthal vorticity are given above the centreline with red, white and blue corresponding to positive, zero and negative values respectively. The in-plane velocity vectors are mirrored below the centreline. There is a significant axisymmetric expansion of the vortex core around a region of reversed flow and a contraction at $z/R \approx 4$ back towards the axis, closing the wake to form the bubble. These types of bubbles have a much larger and more complex recirculation region than the small bubble and have no distinguishable rear stagnation point on the axis. Instead, the large bubble has an open wake with a stagnation line around a core of
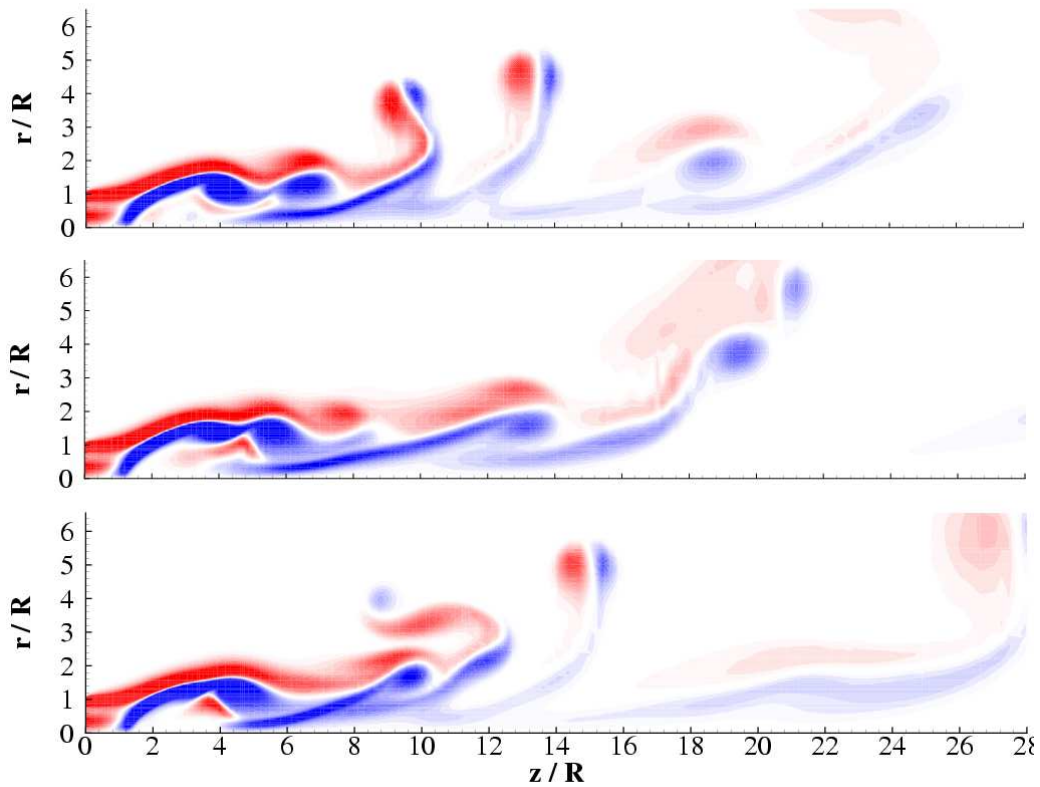
Figure 4.5: A time series showing unsteady oscillations similar to those produced by the Kelvin-Helmholtz instability in the wake of a bubble at $Re = 585$, $S = 1.38$. Each image is showing the axisymmetric plane of the simulations, the times shown are $t = 100$, 110 & 130 and the contours are of azimuthal vorticity where red, white and blue represent positive, zero and negative contours.

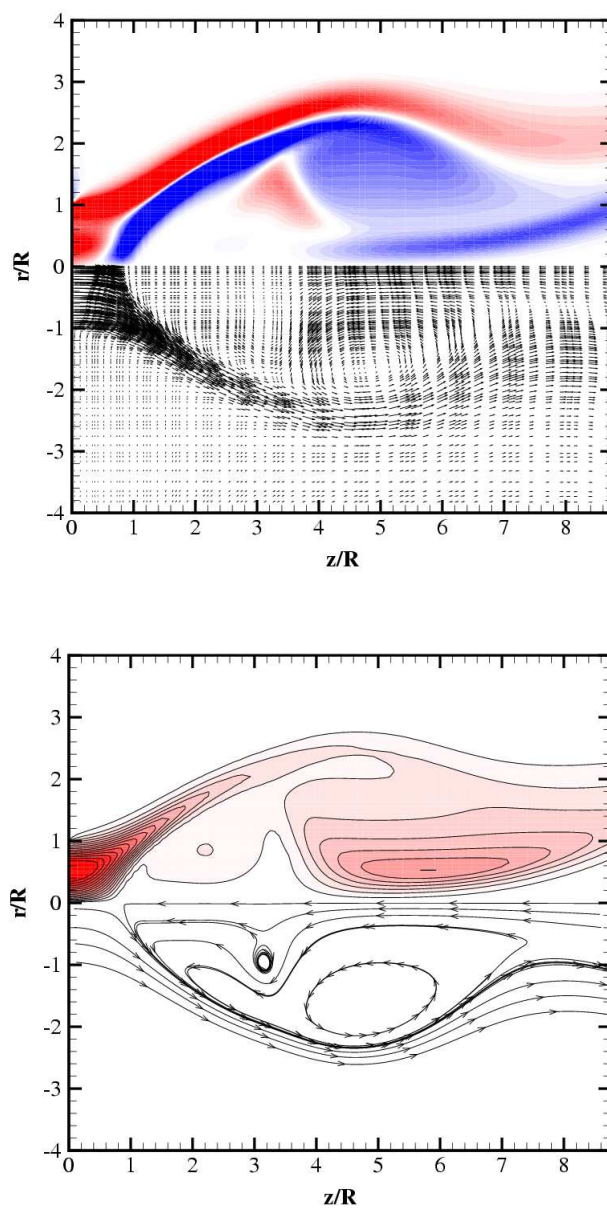Figure 4.6: A large bubble breakdown at $Re = 475$ & $S = 1.50$. The upper image gives contours of azimuthal vorticity with red, white and blue indicating positive, zero and negative respectively. Mirrored are the in-plane velocity vectors. The lower image gives contours of azimuthal velocity; red and white indicating positive and zero respectively. Mirrored in this image are manually place streamlines.

reversed flow that extends downstream. This reversed flow enters the bubble and eventually is expelled from the bubble at the outer of the main internal vortex in the same process observed by Sarpkaya (1971) in experiments of bubbles in divergent pipes.

Large bubbles have two distinct internal regions occupying the front half and rear half almost equally. The front half of the bubble has a region of almost stagnant flow and often a very small and weak recirculation region rotating in the opposite sense to the main recirculation region. The presence of this stagnant zone and its weak vortex ring can usually be identified by the weak positive azimuthal vorticity (red) forming in front of the large negative vorticity zone (blue). The rear section is made up of a large recirculation with negative vorticity (blue). The presence of this recirculation is an indicator that the vortex breakdown state is a bubble as it is representative of the convergence of the flow back to the centreline.

The lower halves of figure 4.6 and 4.7 show two alternative visualisations of the flows. Above the centreline of each image are contours of azimuthal velocity with 16 levels in the range $0 \leq W \leq 1$ where red is positive and white is zero. Mirrored are streamlines chosen manually to best represent the topology of the flow. The internal flow of the large bubbles shows that the stagnant region in the front portion of the breakdown bubble is stagnant in the azimuthal flow also, while the rear portion has relatively high azimuthal velocity near to the centreline. In figure 4.7, an almost conical expansion of the front of the bubble may be indicative of the beginning of the forma- tion of a cone type. The dual recirculation is visualised more clearly in the streamlines of the upper image where the forward recirculation zone is seen as a small ovoid in front of the main recirculation. This recirculation is also seen in the streamlines of figure 4.8 upper. This case shows a strong forward

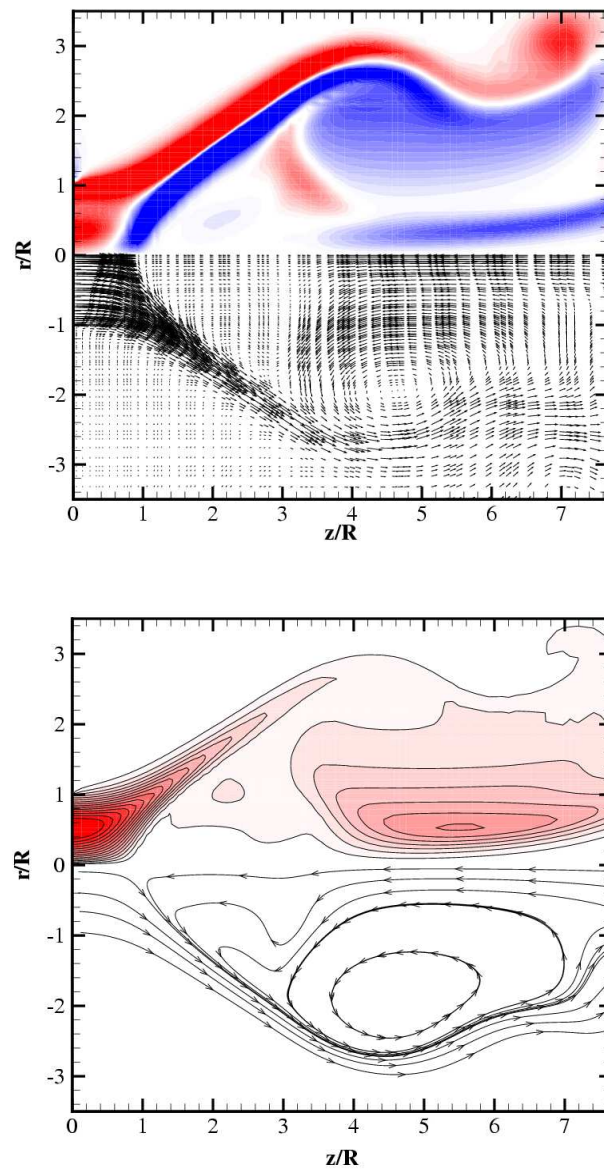Figure 4.7: A large bubble breakdown at $Re = 585$ & $S = 1.44$. The upper image gives contours of azimuthal vorticity with red, white and blue indicating positive, zero and negative respectively. Mirrored are the in-plane velocity vectors. The lower image gives contours of azimuthal velocity; red and white indicating positive and zero respectively. Mirrored in this image are manually place streamlines.
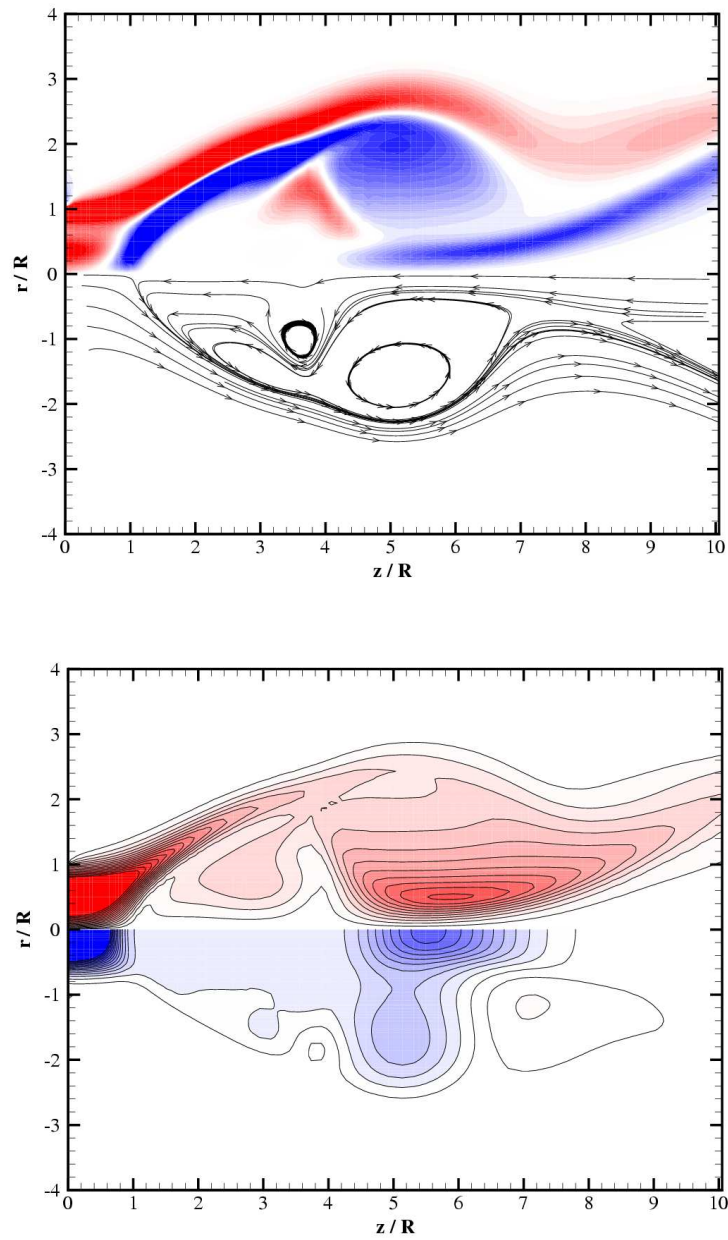
Figure 4.8: A large bubble breakdown at $Re = 467$ & $S = 1.42$. The upper image shows contours of azimuthal vorticity, where red, white and blue indicate positive, zero and negative vorticity respectively, mirrored with manually placed streamlines. The lower image shows contours of azimuthal velocity with 16 equispaced levels from $0 \leq W \leq 1$, mirrored with contours of relative pressure, where blue contours represent negative pressures.

vortex ring that also has significantly stronger azimuthal velocity (figure 4.8 lower). The pressure contours shown mirrored in the lower image of figure 4.8 shows alternating pressure at the boundary of the bubble, possibly indicating the onset of a Kelvin-Helmholtz like shear layer instability at the outer radius. Some evidence of this can be seen as a slight kink in the azimuthal vorticity and streamlines (upper image).

The hybrid bubble-cone type is separated from the large bubble in its dynamics. The hybrid bubble-cone is defined as a state of vortex breakdown where there is quasi-periodic oscillation between a bubble and a cone state. Due to the unsteady behaviour of the wake, it usually sheds vorticity downstream as a bluff body might. In figure 4.9 a time series of a hybrid bubble-cone is shown for $t = 205$, 215, 225, 230, 235, & 240 using contours of azimuthal vorticity (contour levels as previous). When in the bubble stage, such as that shown at $t = 205$, it has the same characteristic as a large bubble, however, this case shows vortex shedding in it wake. The hybrid bubble-cone opens out into a cone state, but does not remain steady like the steady cone (see below). The shear layers begin to converge back to the centreline, reforming a large bubble.

4.5 Steady Cones

Under favourable flow parameters, the steady cone state was found to be present. The steady cone is defined as being a conical expansion state that does not change to a bubble in time, that is, it is steady in as much that the state does not change. The shear layer of the cone expands rapidly and can experiences roll-up and shedding to some extent; however, the majority of the movement is weak and far enough away from the axis that it does not
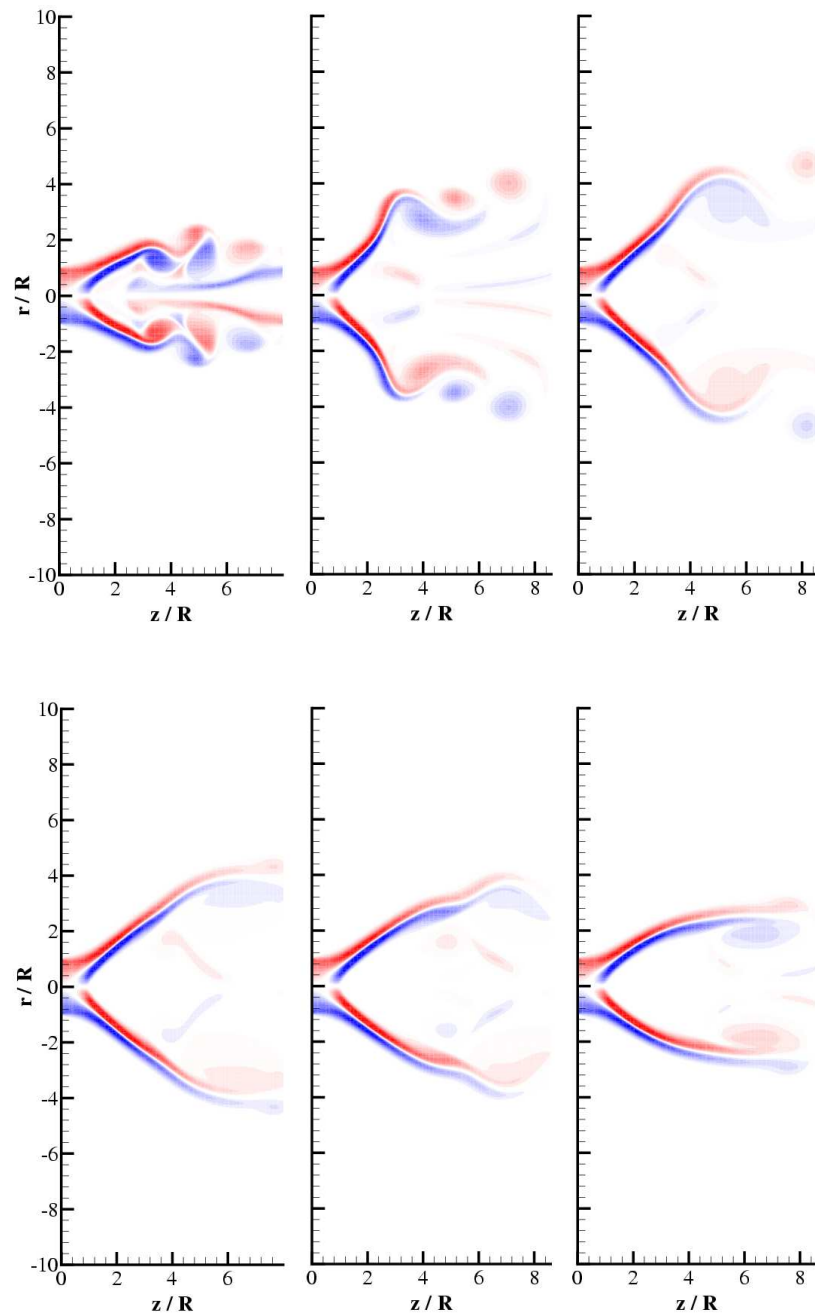
Figure 4.9: The evolution of a hybrid bubble-cone type vortex breakdown for $t = 205$, 215, 225, 230, 235, & 240, from top left to bottom right respectively. Contours of azimuthal vorticity are shown, where red, white and blue represent positive, zero and negative vorticity.

affect the dynamics of the near axis region ($r/R \leq 5-8$). The steady cone is characterised by a rapid linear expansion away from the centreline at an included angle of approximately 90°. The area behind the stagnation point is completely open to the near-stagnant surrounding fluid and has very little velocity.

The upper image of figure 4.10 shows a steady cone breakdown at $Re = 585$, $S = 1.50$, with contours of azimuthal vorticity above the centreline where red, white and blue represent positive, zero and negative vorticity respectively. The in-plane velocity vectors are mirrored below the centreline. The vortex core is seen to stagnate at $z/R \approx 1$, then open out into a axisymmetric conical rotating shear layer. Usually a steady cone has an included angle of approximately 90°. The vectors show that the velocities within the cone are small.

The lower image of figure 4.10 shows contours of azimuthal velocity with 16 equispaced contours in the range of $0 \leq W \leq 1$, where red and white indicate positive and zero levels respectively. Manually placed streamlines are given below the centreline to show the main flow features. The streamlines show the slight movement of the internal fluid due to the entrainment of the internal fluid into the shear layer. The azimuthal velocity shows the low levels of swirl associated with the flow outside of the near-nozzle region of the shear layer.

The shear layer of the steady cone type has a tendency to attach to the outer wall (usually at $r/R = 10$) such that the roll-up of the shear layer is stopped. This can be a problem for simulations where the dynamics of the cone shear layer is important, however an independence of boundary conditions study (see §3.4.4) shows that this does not affect the swirl ratio for vortex breakdown inception. When simulations with the outer wall at
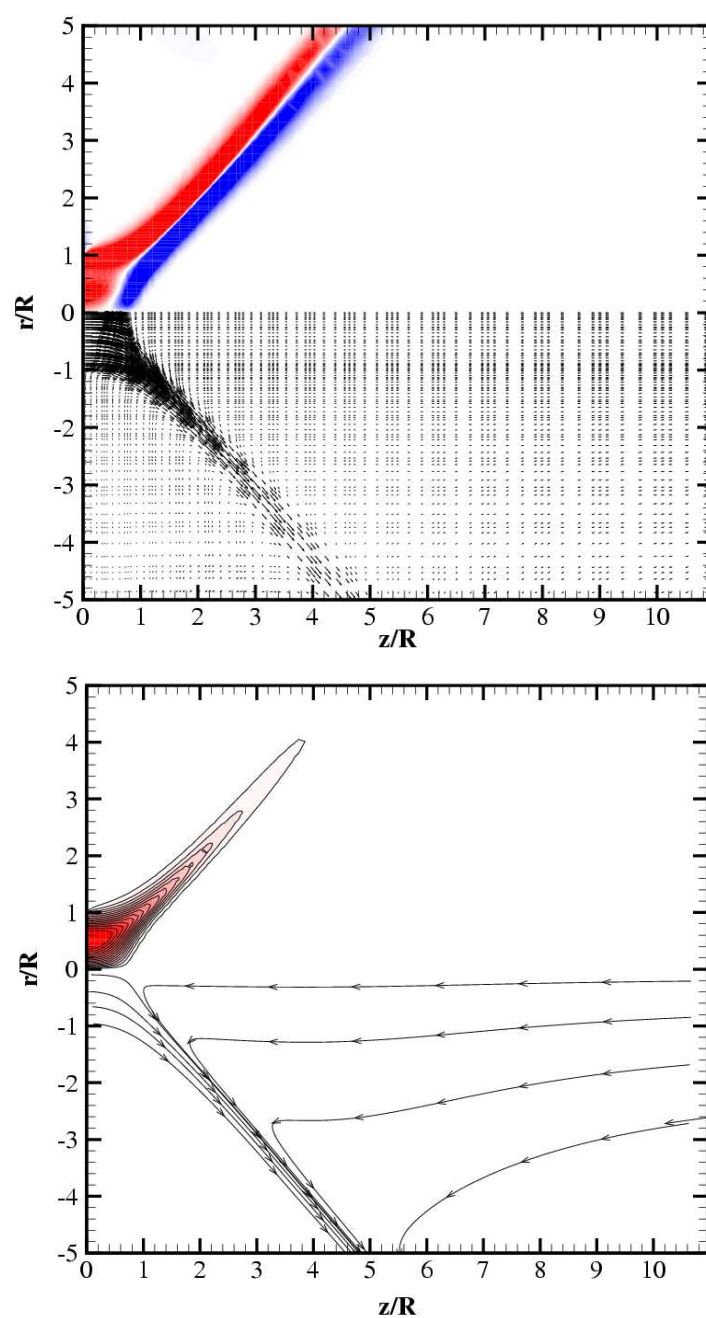
Figure 4.10: An example of a steady cone type at $Re = 585$, $S = 1.50$. In the upper image, contours of azimuthal vorticity are given above the centreline where red, white and blue contours represent positive, zero and negative vorticity respectively. Mirrored are the in-plane velocity vectors. The lower image gives contours of azimuthal velocity where there are 16 equispaced contours in the range $0 \leq W \leq 1$, with red and white indicating positive and zero respectively. Manually placed streamlines are mirrored.

$r/R \geq 20$ are performed, the cone breakdown shows rolling up of the shear layer due to a shear layer instability. A time series of the dynamics of the steady cone is given in figure 4.11. Here, a cone with $Re = 585$ & $S = 1.45$ is visualised using contours of azimuthal vorticity (contours as previous) and manually placed streamlines. Here, the quasi-steady behaviour is shown as the shear layer shows no sign of reforming a bubble type breakdown.

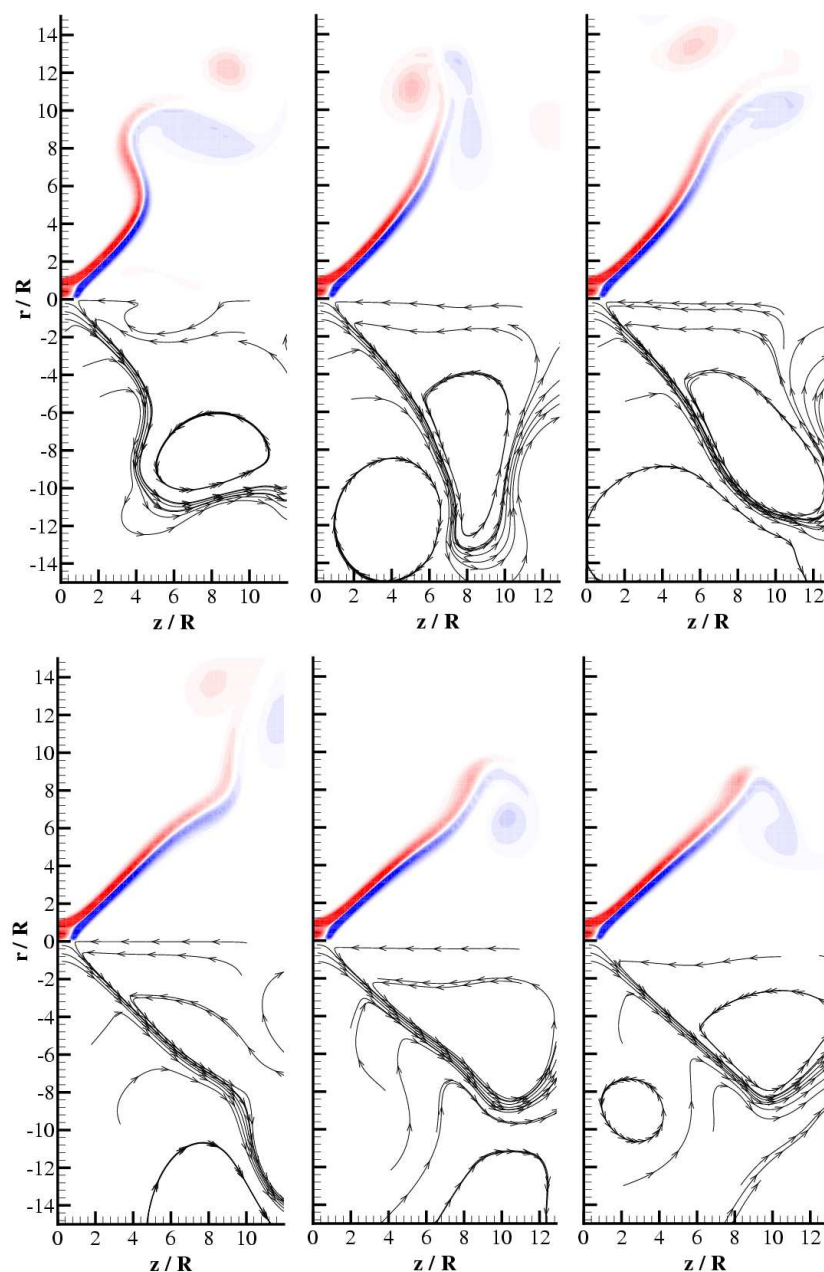Figure 4.11: A series of images in time showing the shedding of the steady cone at $Re = 585$, $S = 1.45$ for $t = 165, 175, 185, 195, 205, 215$ from top left to bottom right. The upper half of each image shows contours of azimuthal vorticity, where red, white and blue are positive, zero and negative respectively. Mirrored on each image are manually placed streamlines showing the major flow features.

Chapter 5

Universality of the Critical Swirl Ratio

This chapter presents an attempt to find a more universal critical parameter for the prediction of the onset of vortex breakdown. To begin with, the analysis used to formulate the *swirl ratio*, proposed by Billant *et al.* (1998), is reviewed. Some preliminary results concerning the universality of the parameter are presented. A modified critical parameter is then developed using integrated velocities, leading to improved universality over the parameter proposed by Billant *et al.* . Finally, using simulation results, the usefulness of both swirl ratios as universal criteria is discussed, supported by simulation results.

5.1 The Critical Swirl Ratio Developed by Billant *et al.* (1998)

Billant *et al.* (1998) offers an analysis of a swirling core which experiences a cone or bubble vortex breakdown state a short distance downstream of

the nozzle. The analysis applies Bernoulli's equation along a streamline that lies on the centreline of the jet. Figure 5.1 shows the physical model that Billant *et al.* used in their analysis , including the vortex before the breakdown, which occurs at an axial location $z = z_1$ (based on the location of the stagnation point). The diagram shows a full diametric slice through a three-dimensional cone-type vortex breakdown with a cylindrical co-ordinate system, such that z denotes the axial distance, r the radial distance and θ the azimuthal angle. The velocity profiles shown are assumed to be axisymmetric and include the axial velocity U and the out of plane azimuthal velocity W at the location $z = z_0$; the radial velocity at this location is assumed to be zero. The far field pressure is denoted by P_{ff}, and the pressures at $z = z_0$ and $z = z_1$ are P_0 and P_1, respectively.

The total head along a streamline in an inviscid, incompressible flow is described by the Bernoulli equation

$$H = \frac{P}{\rho} + \frac{1}{2}(U^2 + V^2 + W^2), \tag{5.1}$$

Conservation of head along the streamline at the axis of the vortex, such that it passes through the stagnation point, gives the balance

$$H = \frac{P_0}{\rho} + \frac{1}{2}U^2_{0(z=z_0)} = \frac{P_1}{\rho}. \tag{5.2}$$

The pressure at the upstream centreline can be expressed as a balance between the far field pressure and the centrifugal force

$$P_0 = P_{ff} - \int_0^\infty \rho \frac{W^2_{(z=z_0)}}{r} \mathrm{d}r. \tag{5.3}$$

Assuming that the velocities within the recirculation zone (behind the stagnation point) are negligible and that the cone type vortex breakdown is open
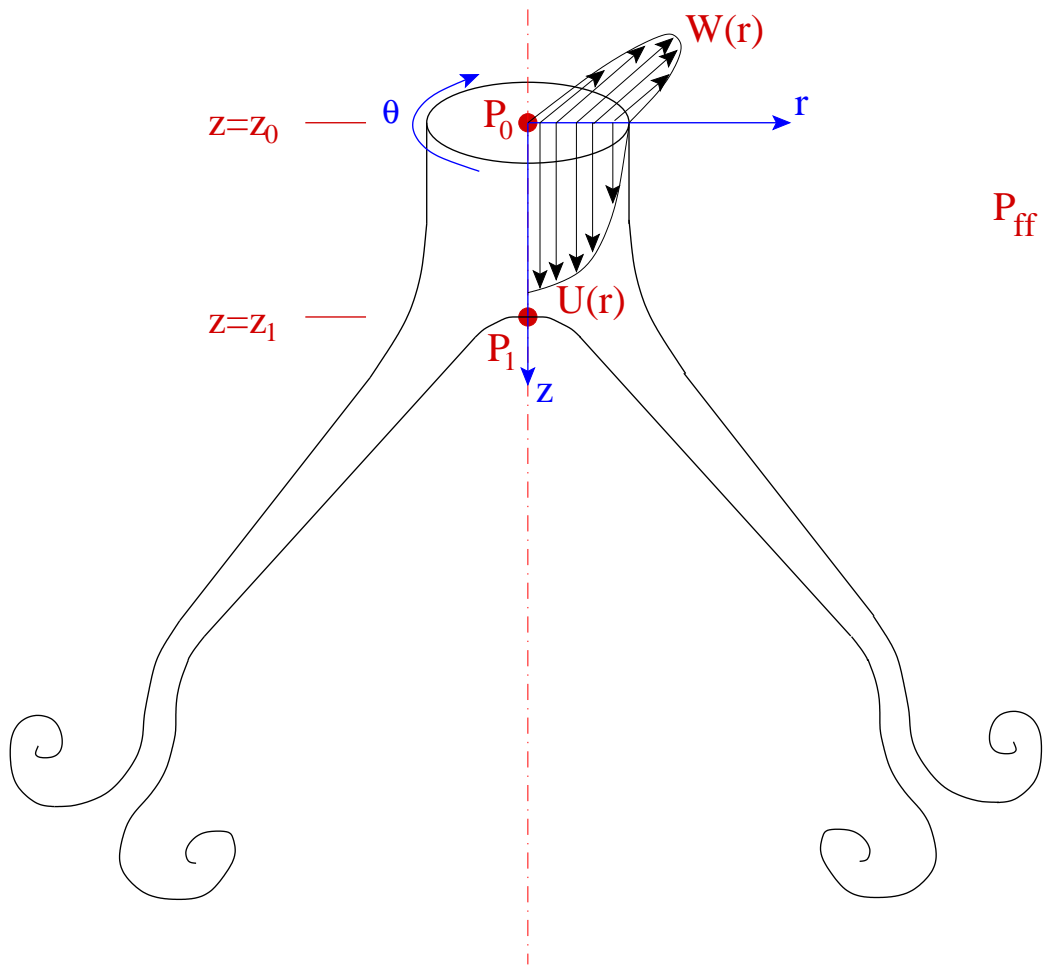
Figure 5.1: The physical model as used in the analysis of a swirling jet with a vortex breakdown cone state.

to the far field pressure, we can assume that $P_1 = P_{ff}$. Substituting this and equation 5.3 into equation 5.2 gives

$$\frac{\int_0^\infty \frac{W^2_{(z=z_0)}}{r}\mathrm{d}r}{U^2_{0(z=z_0)}} = \frac{1}{2}. \tag{5.4}$$

Assuming a Rankine vortex, where there is solid body rotation in the 'core' region, surrounded by irrotational flow, given by

$$W = \begin{cases} \Omega r & : & 0 \le r \le R_c \\ \Omega R_c^2/r & : & R_c < r \le \infty \end{cases}, \tag{5.5}$$

where R_c is the radius of the core of the vortex, allows equation 5.4 to reduce to

$$\frac{W_{0(z=z_0)}}{U_{0(z=z_0)}} = \frac{1}{\sqrt{2}}, \tag{5.6}$$

where $W_0 = \Omega R_c$, the maximum azimuthal velocity.

A similar analysis can be completed for a bubble state, however, matching of the pressure at the centreline with the far field pressure does not hold. The weaker inequality $P_1 \le P_{ff}$ can be used to give

$$\frac{\int_0^\infty \frac{W^2_{(z=z_0)}}{r}\mathrm{d}r}{U^2_{0(z=z_0)}} \ge \frac{1}{2}. \tag{5.7}$$

Using the above analysis, Billant *et al.* proposed a swirl ratio that can be used to assess the criticality of a swirling jet as it emerges from the nozzle of a swirl generator into quiescent fluid. The swirl ratio S is defined as

$$S \equiv \frac{2W_{(R/2,z_0)}}{U_{(0,z_0)}}, \tag{5.8}$$

where $W_{(R/2,z_0)}$ is the azimuthal velocity at half the nozzle radius (roughly the maximum azimuthal velocity) and $U_{(0,z_0)}$ is the axial velocity on the
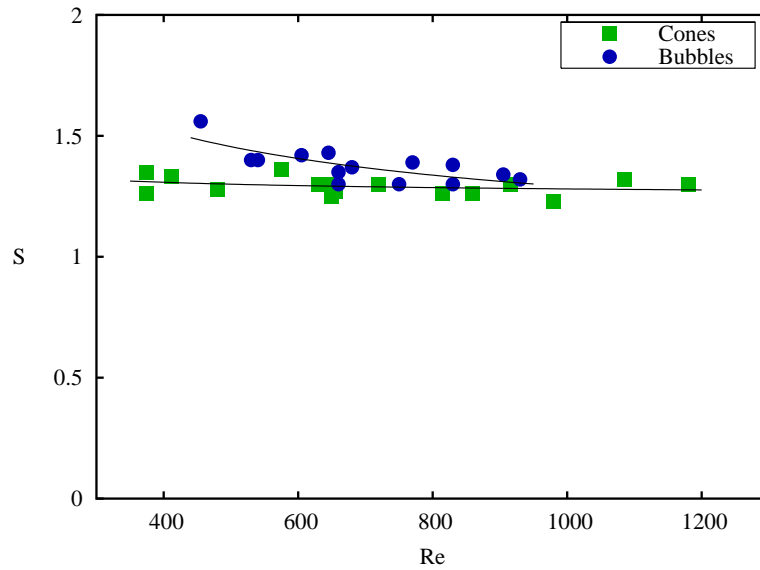
Figure 5.2: Onset of vortex breakdown for the swirl ratio S as measured by Billant *et al.* (1998).

centreline of the jet. Given this definition of swirl ratio, vortex breakdown of the cone type is predicted to occur at $S_c = \sqrt{2}$ and at $S_c \geqslant \sqrt{2}$ for the bubble type. Figure 5.2 shows the onset of vortex breakdown against the parameter S, giving a critical swirl ratio for vortex breakdown of $1.22 \leq S_c \leq 1.42$ for both the bubble and the cone types. Their findings show that the swirl ratio S predicts the onset of vortex breakdown in a swirling jet reasonably well. Additionally, the bubble type was observed at higher swirl ratios than the cone, as suggested by their analysis.

An example of the velocity profiles measured by Billant *et al.* is reproduced in figure 5.3, which shows azimuthal (above) and axial (below) velocity profiles for a variety of increasing swirl ratios. The experimental rig used by Billant *et al.* has a strong contraction before the nozzle outlet that gives an unusual axial velocity profile. The increase in swirl ratio is reflected in the increasing magnitude of the azimuthal component, but also in the devel-

opment of a peak in the axial velocity profile on the centreline. The axial velocity profile with zero swirl has a normal top-hat profile, while there is a strong divergence to a more triangular shape for increasing swirl ratios. To explain this, Billant *et al.* identifies the strong increase in azimuthal velocity through the nozzle contraction (designed for non-swirling flow), arguing that this yields a positive pressure gradient along the centreline inside the nozzle.

While the results show an excellent agreement with the theory, it is not evident that the analysis holds for different velocity profiles and for flows with lower Reynolds numbers. There are a variety of velocity profiles seen in the different scenarios where vortex breakdown exists, such as pipe flow (Faler & Leibovich, 1977; Brücker, 2002; Snyder & Spall, 2000), container flows (Herrada, 2003), jets (Panda & McLaughlin, 1994), wakes (Kalkhoran *et al.* , 1998) and delta wings (Menke & Gursul, 1997). Additionally, if the jet is analysed as a viscous flow, the peak in the velocity profile will degrade with downstream distance and the flow will gradually lose this peak. Indeed, a simulation at the swirl ratio $S = 0.9$ and Reynolds number $Re \approx 350$ (see figure 5.22), demonstrates that this is the case. Here, the axial (above the centreline) and azimuthal (below the centreline) velocity profiles are plotted at a series of downstream locations. The peak in the axial velocity profile has vanished after reaching the downstream location of $z/R = 6$.

The theoretical observations of Wang & Rusak (1997b), demonstrates that the small viscosity at near-critical swirl level can cause large-amplitude disturbances. Similarly, Krause (1985) shows that, in the approximation used, the adverse pressure gradient is solely produced by viscous effects. Based on these observations, it is expected that in low Reynolds number flows, the overall structure of the velocity profile is also important in characterising a vortex. With these studies in mind, it is hypthosised that criteria
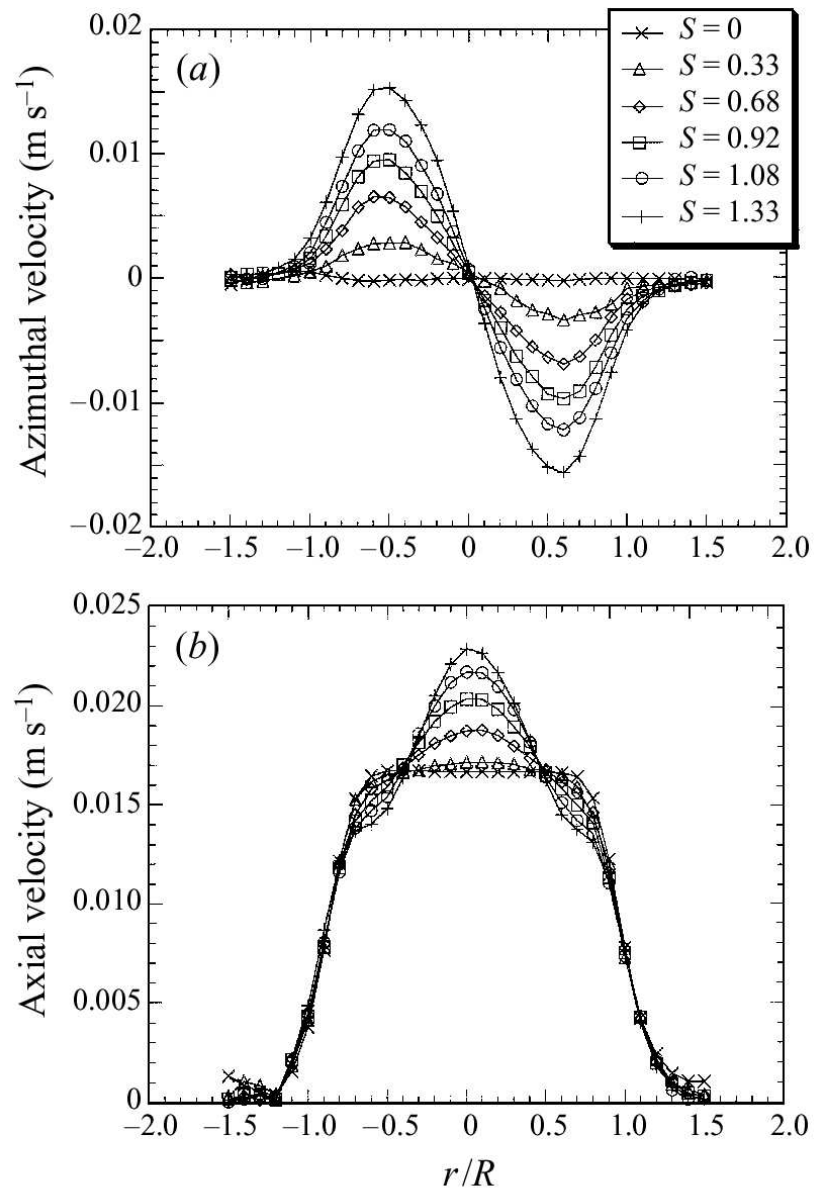
Figure 5.3: Azimuthal (above) and axial velocity profiles of the swirling jet as measured by Billant *et al.* (1998).

using non-integrated parameters lack the ability to universally describe the critical condition of swirling jets with a range of velocity profiles.

The aim of the present research is to quantify the universality of the swirl ratio S for a variety of axial velocity profiles and to attempt to improve it using an adjusted swirl ratio.

5.2 Preliminary Investigation

As a first exploration of the universality of the swirl ratio (S), it was decided to test a variety of velocity profiles and to record the critical swirl ratio S_c for vortex breakdown inception. An axial velocity profile formulation was used to allow the profile shape to be changed while the centreline velocity remains constant. Using this formulation, the axial velocity is given by

$$U(r) = U_0(1 - (\frac{r}{R})^N),\tag{5.9}$$

where U_0 is the centreline velocity, R is the nozzle radius and N is the exponent. The velocity profiles tested are shown in figure 5.4 and correspond to $N = 1, 2, 3, ..., 10$. As can be seen, the profile starts as a triangular shape for $N = 1$, then quickly passes through parabolic and as $N \rightarrow 10$, the profile resembles a more typical 'top-hat' profile. These profiles will have widely different axial flow rates and axial momenta, however they are all constructed to have the same centreline axial velocity. If the swirl ratio S is universal and profile independent (as is implied in the analysis above), then, all of these velocity profiles should demonstrate the same critical swirl ratio.

The azimuthal velocity profiles were defined by
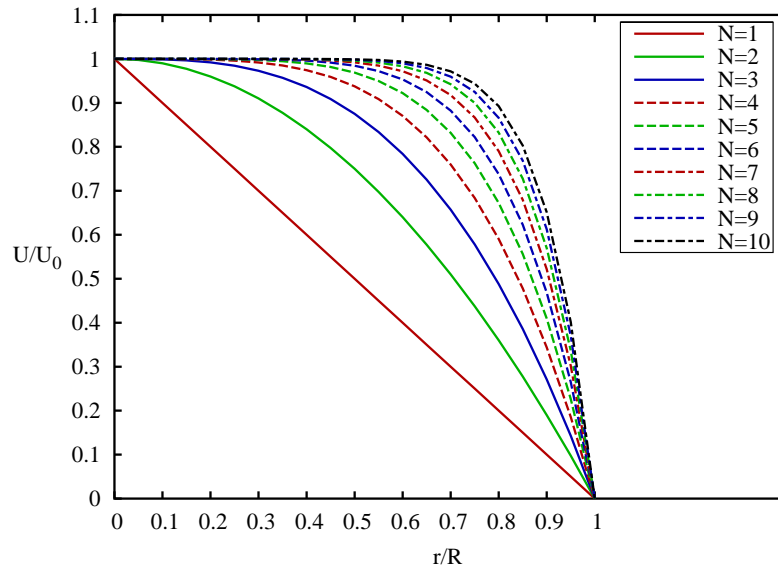
$$W(r) = W_0 \sin(\pi/Rr),\tag{5.10}$$

Figure 5.4: Axisymmetric axial velocity profiles as for $N = 1, 2, 3, ...10$ used in the preliminary examination.

where W_0 is the maximum azimuthal velocity. This profile was chosen as an approximation to the azimuthal velocity variation observed in the experiments of Billant *et al.* (1998).

A series of simulations with increasing swirl ratios were effected by starting the jet from zero initial conditions with a particular parameter pair Re, S. Control of the swirl ratio was achieved by varying the maximum azimuthal velocity W_0, while the maximum axial velocity U_0 was held constant. As the parameter N is increased, the average axial velocity $\bar{U}$ also increases. This also manifests as an increase in the simulation Reynolds number. The result of altering the Reynolds number with N has the effect of reducing the critical swirl ratio – the swirl ratio needed to cause vortex breakdown (see §4). The results of these tests are shown in figure 5.5, which shows the critical swirl ratios for vortex breakdown, plotted as a function of the parameter N.

As can be seen, the critical swirl ratio is highly dependent on the shape
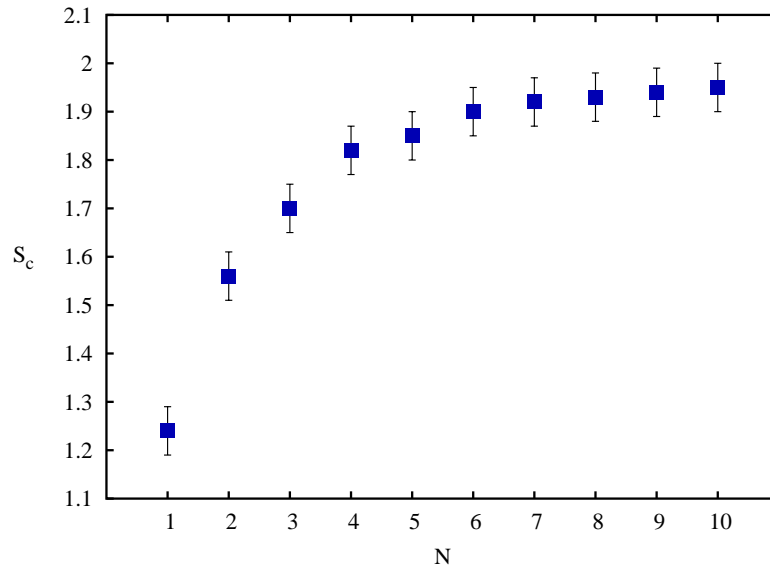
Figure 5.5: Dependence of critical swirl (Sc) number on velocity profile, as varied using the parameter 'N'.

of the axial velocity profile. Changing the profile shape from triangular to top-hat results in a 56% increase in the critical swirl ratio required for vortex breakdown, despite the Reynolds number increase (and corresponding decrease in swirl ratio magnitude needed for breakdown). This is not wholly unexpected since the vortex core is not completely described by its centreline velocity alone. In these cases, increasing the parameter N causes the jet to a have significantly greater flow rate and momentum; therefore, it is not surprising that an increase in the parameter W_0 is necessary to cause such a jet to undergo breakdown.

Furthermore, these tests show that for a realistic top-hat profile ($N = 10$), the critical swirl ratio is $S_c \approx 1.95$ as measured at the nozzle outlet; an increase in S_c of nearly 40% over the theoretically predicted S_c in Billant *et al.* (1998).

5.3 Detailed Investigative Method

To more clearly explore the effect of the axial velocity profile on the critical swirl ratio, it was decided a set of tests of greater detail were needed. Five different velocity profiles were chosen to be tested over a broad range of Reynolds numbers. This section deals with the description of the five different test cases used. These cases are named Profile A, B, C, D, and E.

5.3.1 Profile A

Profile A uses the axial velocity profile formulation given in equation 5.9. However, this profile has been matched to the $S = 1.33$ case in Billant *et al.* based on the momentum flow rate. The following analysis shows the method used to match the chosen velocity profile formulation with that of Billant *et al.* (1998).

Momentum Flow Rate Matching

An axisymmetric jet with a velocity profile $U(r)$ given by equation 5.9, where r is the radial variable, has an axial momentum inflow rate $\dot{M}_z$ described by

$$\dot{M}_z = \int_A U \mathrm{d}\dot{m}, \tag{5.11}$$

where U is the axial velocity as a function of radius, and $\dot{m}$ is the mass flow rate through the area A. The incremental mass flow rate can be rewritten as

$$\mathrm{d}\dot{m} = \rho U \mathrm{d}A = \rho U 2\pi r \mathrm{d}r, \tag{5.12}$$

where ρ is the fluid density and $\mathrm{d}A = 2\pi r \mathrm{d}r$ is the area element. If the fluid is assumed to be incompressible, $\dot{M}_z$ is given by

$$\dot{M}_z = 2\pi\rho \int_0^R U^2 r\mathrm{d}r, \tag{5.13}$$

where R is the nozzle radius. Substituting equation 5.9 for U gives

$$\dot{M}_z = 2\pi\rho \int_0^R (U_0(1 - (\frac{r}{R})^N)^2 r\mathrm{d}r, \tag{5.14}$$

where U_0 is the centreline axial velocity and N is the profile exponent. $\dot{M}_z$ can be simplified to

$$\dot{M}_z = 2\pi\rho U_0^2 \int_0^R r - 2\frac{r^{N+1}}{R^N} + \frac{r^{2N+1}}{R^{2N}} \mathrm{d}r \tag{5.15}$$

Following some algebra, this reduces to

$$\dot{M}_z = \pi\rho U_0^2 R^2 \Big(1 + \frac{1}{N+1} - \frac{4}{N+2}\Big), \tag{5.16}$$

and can be further simplified to

$$\dot{M}_z = \pi\rho U_0^2 R^2 \Big(\frac{N^2}{N^2 + 3N + 2}\Big). \tag{5.17}$$

By equating the momentum flow rate of the $S = 1.33$ profile measured in Billant *et al.* with a top-hat velocity profile that has the same momentum flow rate, we obtain the following relation

$$\int_A U\mathrm{d}\dot{m} = \bar{\dot{m}}\overline{U_m}, \tag{5.18}$$

where $\overline{U_m}$ is the top-hat velocity needed to achieve the momentum flow rate dictated by the LHS, and $\bar{\dot{m}}$ is the mass flow rate based on a uniform velocity $\overline{U_m}$. The profile can now easily be matched through equating the average (top-hat) properties of the jet in Billant *et al.* , and the momentum flow rate of the new jet, as described in equation 5.17, shown as follows

$$\bar{m}\overline{U_m} = \pi\rho U_0^2 R^2 \left(\frac{N^2}{N^2 + 3N + 2}\right).$$ (5.19)

Substituting $\bar{m} = \rho\pi R^2\overline{U_m}$ and cancelling gives

$$\frac{\overline{U_m}^2}{U_0^2} = \left(\frac{N^2}{N^2 + 3N + 2}\right).$$ (5.20)

Now let $C = (\frac{\overline{U_m}}{U_0})^2$; after some re-arranging, this yields

$$N^2(C - 1) + 3CN + 2C = 0,$$ (5.21)

which can be solved for N using the quadratic formula to give $N = 2.37$ for the Profile A case.

Numerical integration of the $S = 1.33$ profile given in Billant *et al.* (1998) (shown using green squares in figure 5.3), was achieved through the use of the trapezoidal rule with the original data (relatively coarse measurements) and a spline fit with much finer resolution. The two integrations were performed in the style of equation 5.18 using a non-dimensionalised form of the velocity profile. The integration using the raw data and the spline fit gave values of $\overline{U_m} = 0.014192$ and $\overline{U_m} = 0.014199$ respectively, corresponding to a difference of only 0.05%. Table 5.1 shows the parameters used in the quadratic equation and the solution to N for the Profile A case.

Therefore, from the above reasoning, the profile defined by equation 5.9 with an exponent of $N = 2.37$ has the same overall momentum flow rate as the $S = 1.33$ profile given in Billant *et al.* (1998). Figure 5.6 shows the $S = 1.33$ profile of Billant *et al.* (1998) superimposed upon the axial velocity profile of the Profile A case.

This profile fulfills the purpose of testing the effect of small changes in profile shape on the critical swirl ratio for vortex breakdown.
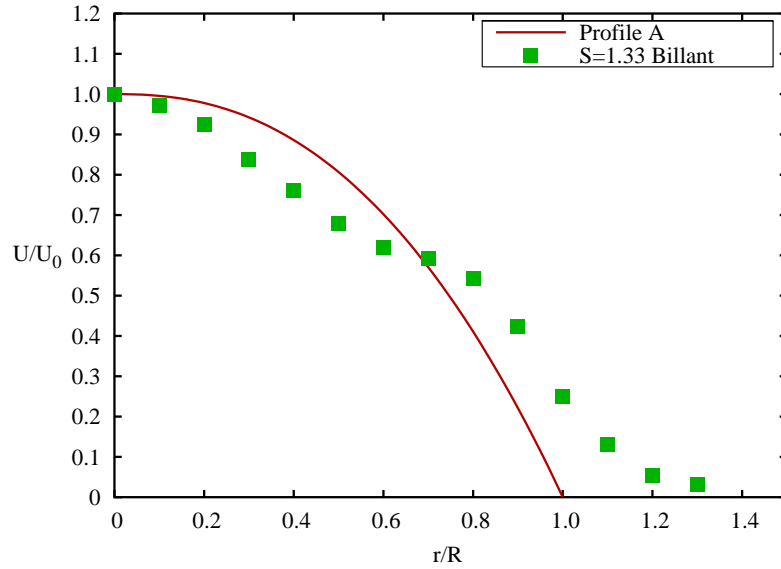
Figure 5.6: The $S = 1.33$ profile of Billant *et al.* (1998) superimposed upon the profile as described by equation 5.9 with an exponent $N = 2.37$.

$\overline{U_m}$	0.0142
U_0	0.023
C	0.381
N	2.37

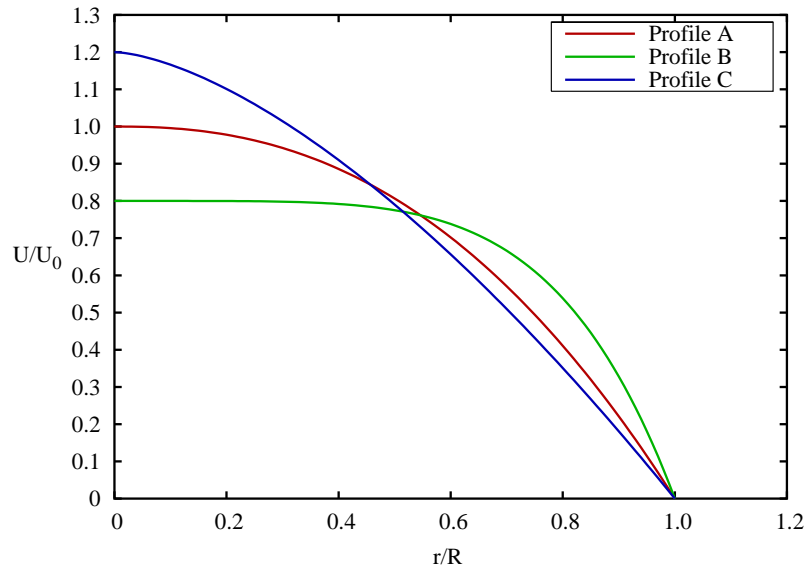Table 5.1: Parameters and result of profile matching for Profile A.

Figure 5.7: A comparison of the Profiles B and C with respect to profile A. All three have the same momentum flow rate, but different shapes.

5.3.2 Profile B and Profile C

The purpose of these two profiles is to test the effect of altering the centreline velocity, without altering the overall momentum flow rate. They are also based on the formulation given in equation 5.9 and have their momentum flow rate matched using the method shown above. Both have been chosen to have a centreline axial velocity of $0.8 \times U_0$ and $1.2 \times U_0$ respectively. Therefore, these two velocity profiles are significantly different in shape from Profile A, but maintain the same momentum flow rate. Figure 5.7 shows Profile B and Profile C superimposed upon Profile A.

Table 5.2 shows the parameters used to calculate the exponents N for the Profile B and C cases. As is shown, the average velocity $\overline{U_m}$ is fixed as the descriptor of the overall momentum flow rate in both the $S = 1.33$ profile from Billant *et al.* (1998), and the Profile A case. The centreline velocities U_0 are both a factor of 0.8 and 1.2, respectively, of the centreline velocity of

	Profile B	Profile C
$\overline{U_m}$	0.0142	0.0142
U_0	0.0184	0.0276
C	0.596	0.265
N	5.01	1.55

Table 5.2: Parameters and result of profile matching for Profiles B and C

Profile A.

5.3.3 Profile D

Profile D differs from the three previous profiles in that it does not seek to
match the momentum flow rate of the jet presented in Billant *et al.* (1998).
Instead, this case is used to investigate the role of the ability of the centreline
velocity to describe the jet. Based on the preliminary investigation (in §5.2),
this case is expected to be a 'worst case scenario'. The Profile D case has
the same centreline axial velocity as the Profile A case, but is of a top hat
profile.

Figure 5.8 shows Profile D as compared to the $S = 1.33$ profile of Billant
et al. . As can be seen, the momentum flow rate in the Profile D jet will be
much greater than in the $S = 1.33$ jet. The profile shape is also based on the
equation 5.9 with an exponent of $N = 10^5$, therefore there is only a slight
tapering off at $r = R$ as is evident in figure 5.8.
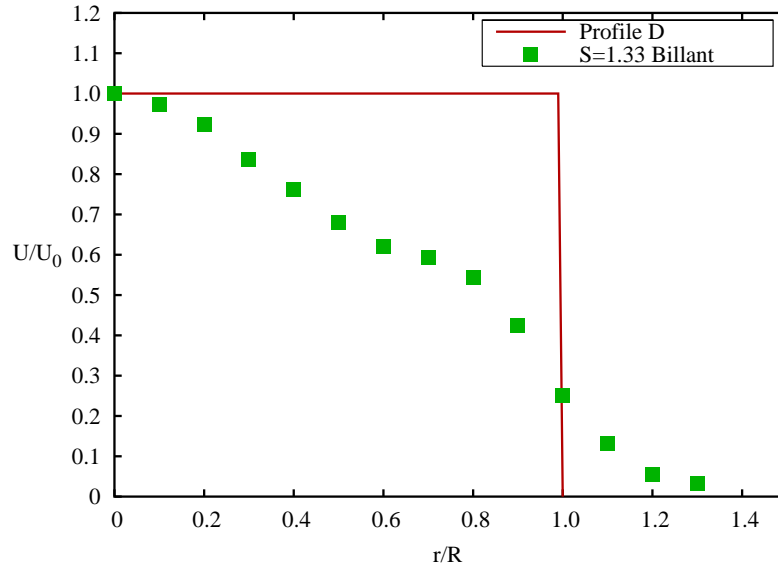
Figure 5.8: The $S = 1.33$ profile of Billant *et al.* (1998) superimposed upon the profile as described by equation 5.9 with an exponent $N = 10000$.

5.3.4 Azimuthal Velocity Profile for the Profile A,B,C and D Cases

Profile cases A, B, C and D all have the same formulation for the azimuthal velocity profile. Their azimuthal profiles are described by the equation

$$W(r) = W_0 \sin(\frac{\pi}{R}r), \tag{5.22}$$

where W_0 is the maximum azimuthal velocity, located at $r = R/2$. This profile shape bears close similarity to those azimuthal velocities shown in 5.3 and also is a reasonable approximation of the Rankine vortex. This formulation allows the increase in swirl ratio necessary for the simulations to be achieved through increasing the parameter W_0.
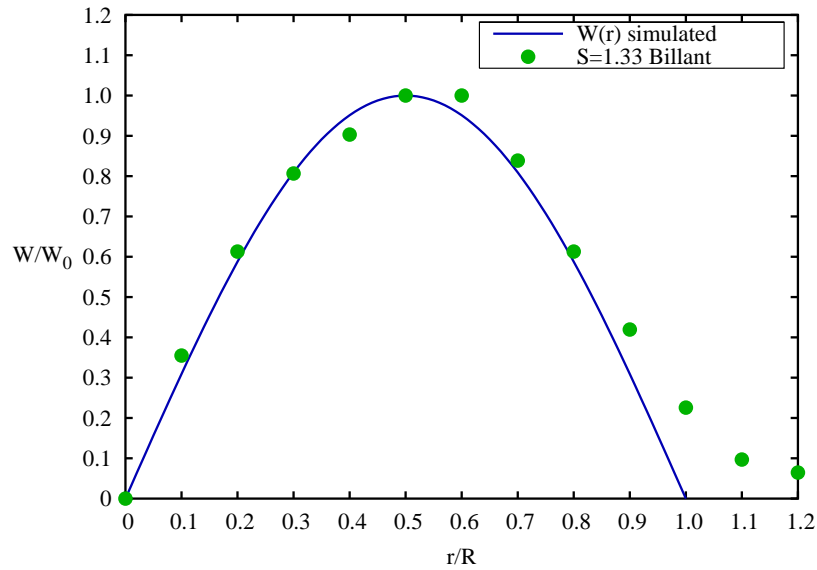
Figure 5.9: Azimuthal velocity formulation as compared to that measured by Billant *et al.* (1998).

5.3.5 Profile E

Profile E is aimed at providing the closest comparison to the experiments of Billant *et al.* . This profile is also included to validate the simulated results against their results. The profiles for the axial and azimuthal velocities are created by fitting splines to the normalised data for the $S = 1.33$ U and W profiles. Figure 5.10 shows the Profile E case axial (U) and azimuthal (W) velocity profiles compared to the data from the $S = 1.33$ profiles from Billant *et al.* (1998).

5.4 Results: Critical Swirl Ratios for Profiles A–E

A series of simulations using the profiles described above were run such that the critical swirl ratios could be ascertained. This involved many simulations with progressively increased swirl ratios for a variety of Reynolds numbers. The state of the vortex with respect to vortex breakdown was observed after sufficient time was allowed for the flow to become steady or quasi-steady. Swirl ratios were chosen such that the resolution in the swirl ratio was increased near the critical swirl ratio. This was achieved by running one set at a resolution of $\delta S = 0.05$, observing the results and running a second set of simulations at $\delta S = 0.01$ or $S = 0.02$ for the region where vortex breakdown occurs. This guarantees an error in the measurement of $\delta S \leqslant \pm 0.02$. The mapping of the critical swirl ratio was performed for a range of Reynolds numbers which overlap the experimental measurements made by Billant *et al.* (1998).

5.4.1 Results Overview

Figure 5.11 shows the resulting critical swirl ratios for vortex breakdown in the Profile A–E cases. The critical swirl ratios measured by Billant *et al.* are also included as a comparison of the simulation results (solid green squares). Each set of results has been fitted with a curve to clarify the trend of the data. Each curve is of the form

$$y = a/\sqrt{x} + b, \tag{5.23}$$

where the constants a and b are determined using the least squares method. This form was chosen to best represent the behaviour of the data.
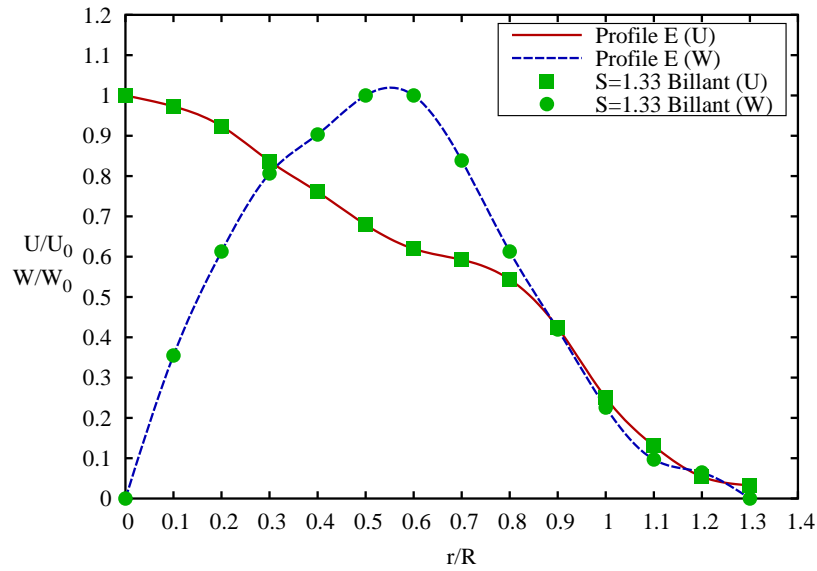
Figure 5.10: Profile E axial and azimuthal velocities (U,W) compared to the $S = 1.33$ data of Billant *et al.* (1998) (green squares).
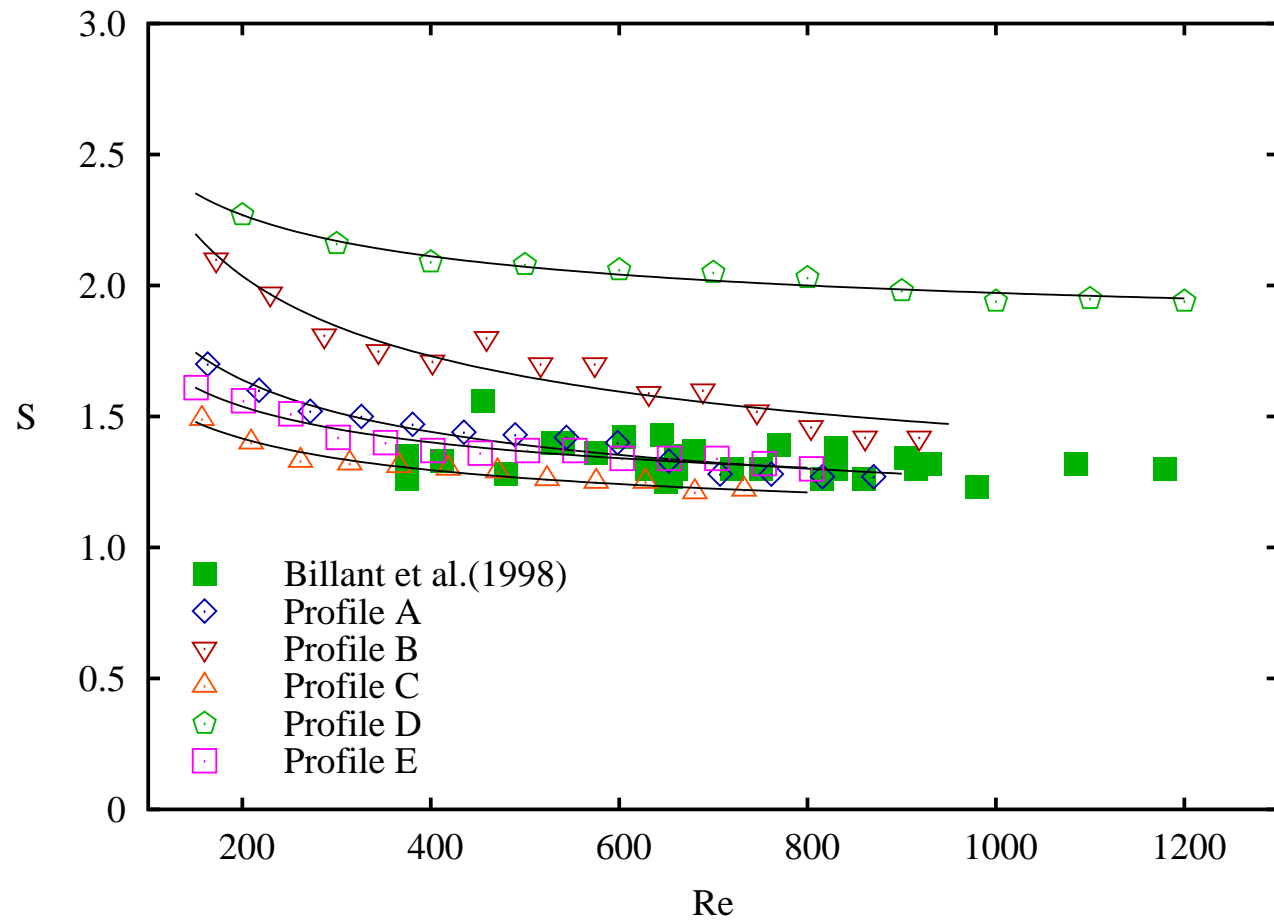
Figure 5.11: Critical swirl ratios for vortex breakdown for Profile A, B, C, D & E cases as compared to those measured in Billant *et al.* (1998).

The critical swirl ratios measured by Billant *et al.* (solid green squares), show decreased spread above $Re \approx 600$. At lower Reynolds numbers, the results are less conclusive with the spread of critical swirl ratios spanning $\delta S \approx 0.3$. In comparison, the simulated data have a spread of $\delta S \approx 0.9$ for all Reynolds numbers. Each set of data appears to asymptote towards a constant critical swirl ratio with increasing Re. At low Reynolds numbers $Re \lesssim 400$, all simulated cases show increases in swirl ratio from the asymptotic value. This effect gives some indication of the increased influence of viscosity in these low Reynolds number flows. The increased spread seen in the results of Billant *et al.* could be explained by increased viscous effects that are not accounted for in their analysis.

As the Reynolds number is increased, most simulated cases show a secondary asymptote of the critical swirl ratio. This effect can be more clearly seen in the data for the Profile A case, where at $Re \approx 600$, this asymptote ends and there is a rapid drop to a lower asymptotic value. This effect could be a reflection of the analysis and results given in Billant *et al.* (see figure 5.2), where cone vortex breakdown is consistently realised for lower swirl ratios than the bubble type. The results of a meta-stability study presented later in §6 will show that in a simulated flow, the cone type is only experienced as the first vortex breakdown state when the Reynolds number is high ($Re \geq 700-800$). At lower Reynolds numbers, swirl ratios must be increased to achieve a cone type breakdown. The curve in Re, S parameter space that describes the onset of cone type breakdown, intercepts the lower and flatter bubble-type breakdown curve at the location where the second drop in swirl ratio is experienced. Perhaps this explains the second asymptote in critical swirl ratios at higher Reynolds numbers.
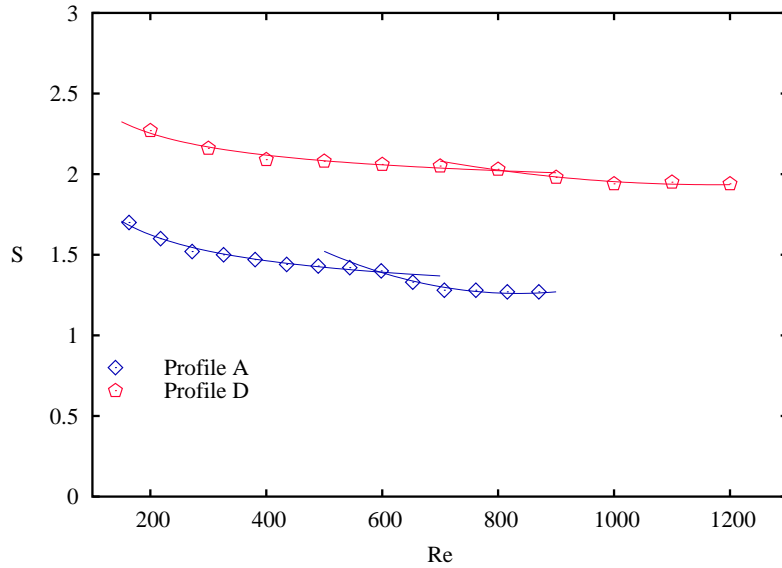
Figure 5.12: The secondary asymptotes for the Profile A & D cases, speculated to be caused by the lower swirl ratio onset of the cone type of vortex breakdown at high Reynolds numbers.

5.4.2 Profile E Case Results

The results for the Profile E case (where the velocity profiles are matched with the $S = 1.33$ profiles) show an excellent comparison with the critical swirl ratios of Billant *et al.* . Figure 5.13 shows the data from Billant *et al.* in solid green squares, and the data for Profile E in hollow magenta squares. Each set is fitted with a curve using the formulation given in equation 5.23. For $400 \lesssim Re \lesssim 800$ the data shows good similarity and the regression lines show excellent agreement.

5.4.3 Profile A, B and C Case Results

The critical swirl ratios for profile A show close resemblance to those of Billant *et al.* and those of Profile E reflect the accuracy of the momentum flow rate matching method. There is some separation at lower Reynolds

Figure 5.13: Comparison between the Profile E case and the data from Billant *et al.* (1998) showing excellent agreement between simulated and experimental results for a range of Reynolds numbers.

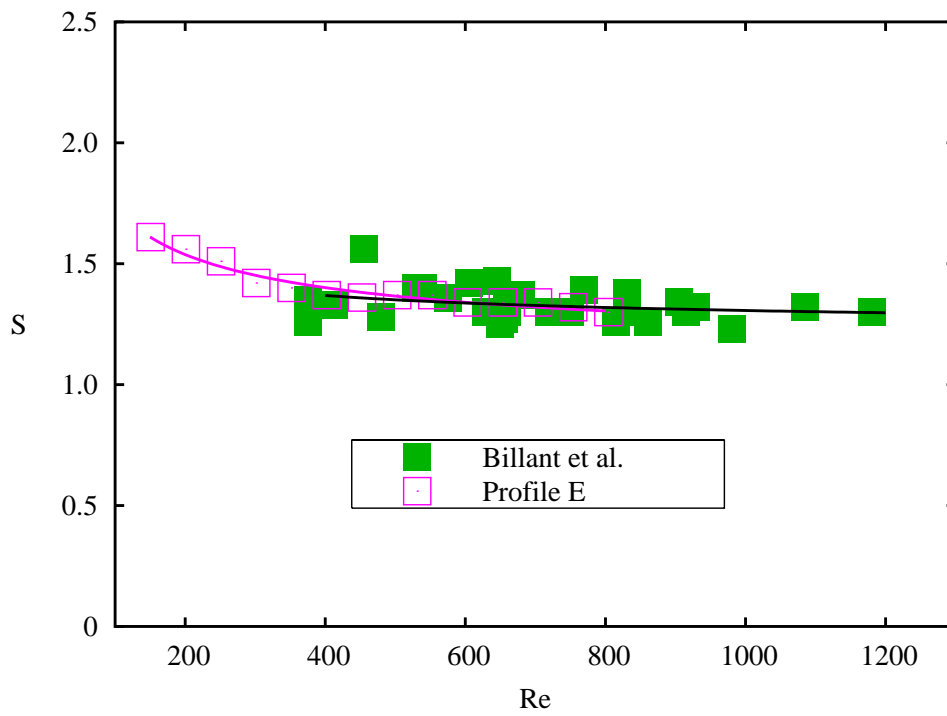numbers such that Profile A case records slightly higher S_c than Profile E. These results indicate that using a similar shaped profile yields similar critical swirl ratios to those measured by the experiments. The slight discrepancy may be described by the differences in shape of the experimental profile and that of Profile A; Profile A has more momentum flow rate at $r/R \lesssim 1/2$, whereas the experimental profiles have more at $r/R \gtrsim 1/2$. It is probable that greater momentum flow rate near the centreline delays the inception of vortex breakdown.

The critical swirl ratio curves for the Profile B and C cases show a significant shift from that of the Profile A case, despite having the same momentum flow rate. Profile B shows a significant increase in the critical swirl ratio necessary for vortex breakdown and Profile C shows a less drastic but still significant decrease in critical swirl ratio. These profiles have different centreline velocities and hence, it seems reasonable to hypothesise that it is the centreline velocity that is causing the drastically different critical swirl ratios in the two cases.

Considering the formulation of S (see equation 5.8), we can see that for both Profile B and C, the denominator of the equation has changed by $\pm 20\%$. If we assume that the jet is better described by some bulk or integrated measure (at least at low Reynolds numbers), we could conclude that the same overall swirl is needed to cause vortex breakdown. Therefore, our numerator used to construct the swirl ratio is unchanged. For a profile that has the same momentum flow rate, but smaller centreline velocity we would expect the swirl ratio to be higher. The inverse applies for a narrower profile such as that of the Profile C case.

The results of Profiles B and C show that the profile shape for a momentum flow rate matched jet, can have a large effect on the critical swirl

ratio for vortex breakdown and that characterisation with the swirl ratio S gives a variety of critical swirl ratios that vary widely from the prediction of $S \approx \sqrt{2}$.

5.4.4 Profile D Case Results

The Profile D case has much higher momentum flow rate than Profiles A, B, C and E. It is of 'top-hat' form and shares the centreline velocity of the Profiles A and E cases. The critical swirl ratios shown using this case are approximately 50% higher than those of the Profile A case. Considering that this case has the same centreline axial velocity, the increased critical swirl ratio must be indicative of the role of momentum flow rate, or some other bulk property of the jet.

5.4.5 Interpretation using S_i

Billant *et al.* marginally increased the accuracy of their critical swirl ratios by avoiding the assumption of the Rankine vortex and using the partially integrated criterion S_i, described by

$$S_i = \frac{\left(\int_0^\infty \frac{W_{(r,z_0)}^2}{r} \mathrm{d}r \right)^{\frac{1}{2}}}{U_{(0,z_0)}}, \tag{5.24}$$

where the presence of a stagnation point in the vortex requires that $S_i = \frac{1}{\sqrt{2}}$ for a cone and $S_i \geqslant \frac{1}{\sqrt{2}}$ for a bubble.

Figure 5.14 shows the result of interpreting the critical swirl ratio with the use of the azimuthal velocity profile integrated criterion S_i. As can be seen, the prediction over a range of velocity profiles has not improved. In the Profile B and D cases, the closer the velocity profile comes toward a top-hat profile, the greater the deviation in the predicted critical swirl ratios.
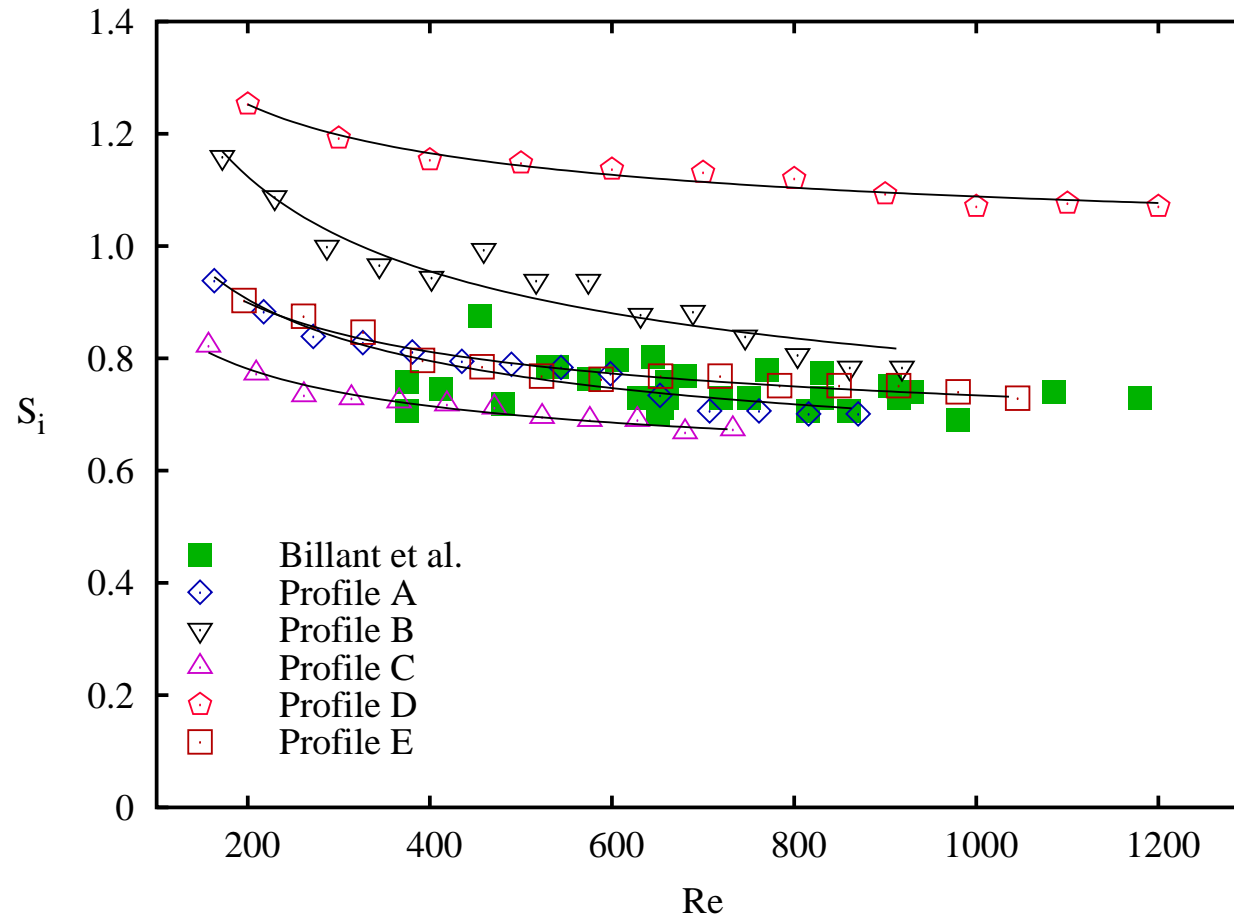
Figure 5.14: The critical swirl ratios for the tested profiles as interpreted using the criterion S_i shown in equation 5.24.

From these results, it is clear that integration of the azimuthal velocity profile alone is insufficient to describe the state of the vortex core with respect to criticality. This confirms the hypothesis that the centreline velocity does not sufficiently describe the axial component of the vortex core to be able to predict the onset of vortex breakdown. §5.5.4 will describe how a combination of axial and azimuthal integration leads to greatly improved universality of critical swirl ratios.

5.5 A Universal Criterion

Given the analysis of the results shown in the previous section and the formation of a hypothesis based on these, an attempt has been made here to increase the universality of the swirl ratio using integrated parameters. Following the hypothesis that the centreline axial velocity is not sufficient to describe the vortex core, an integrated axial velocity is used in the denominator of an adjusted swirl ratio S_a. Finding that this parameter does not improve the collapse of critical swirl ratios, a swirl ratio based on both integrated axial and azimuthal components is described. This parameter S_* shows a much improved collapse and universality of critical swirl ratios not only for different velocity profiles, but also for locations downstream of the nozzle.

5.5.1 An Adjusted Swirl Ratio

Maintaining the form of the critical swirl ratio S, as defined by Billant *et al.* , as consisting of a ratio of azimuthal and axial velocity, a new parameter S_a is described. This new parameter includes the mass flow rate averaged axial velocity $\bar{U}$ as a replacement for the centreline velocity in the swirl ratio
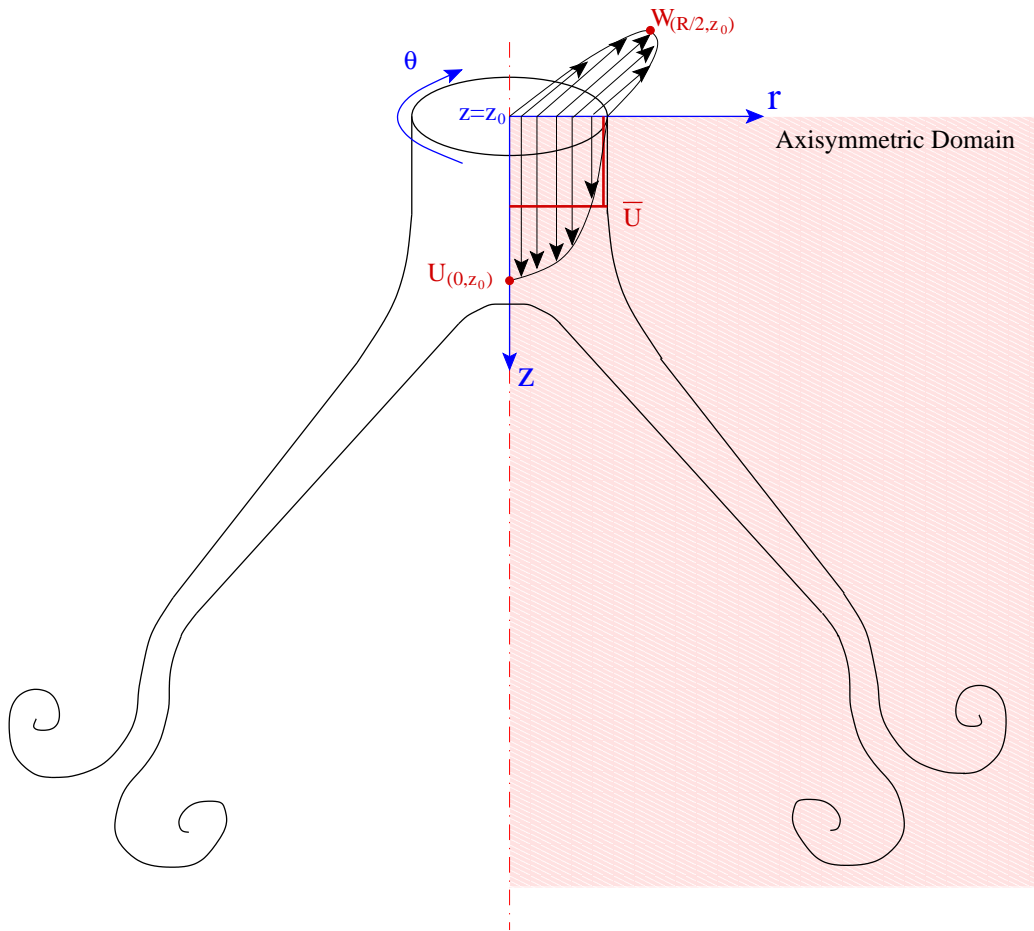
Figure 5.15: The equivalent velocity $\bar{U}$ for a top-hat velocity profile with the same mass flow rate as the variable profile.

denominator. This yielded the adjusted swirl ratio S_a which is described by

$$S_a = \frac{2W_{(R/2,z_0)}}{\bar{U}}, \tag{5.25}$$

where $\bar{U}$ is the mass flow rate averaged axial velocity. A graphical representation of the concept is shown in figure 5.15 where the axial velocity profile is made equivalent to a jet with the same mass flow rate but with a top-hat profile.

5.5.2 Defining $\bar{U}$

The axial mass flow rate $\dot{m}$ of the non-uniform axial velocity $U(r)$ in a axisymmetric and incompressible jet can be expressed as

$$\dot{m} = \rho \int_0^\infty U \mathrm{d}A, \tag{5.26}$$

where $\mathrm{d}A$ is the incremental area of the annular differential element and is given by

$$\mathrm{d}A = 2\pi r \mathrm{d}r. \tag{5.27}$$

The equivalent mass flow rate $\dot{m}_e$ of a velocity profile with constant velocity $\bar{U}$ over the domain $0 \leq r \leq R$ can be expressed as

$$\dot{m}_e = \rho \pi R^2 \bar{U}. \tag{5.28}$$

Equating the mass flow rates $(\dot{m}_e = \dot{m})$ gives

$$\rho \pi R^2 \bar{U} = 2\rho \pi \int_0^\infty U r \mathrm{d}r, \tag{5.29}$$

and hence, $\bar{U}$ is given by

$$\bar{U} = \frac{2}{R^2} \int_0^\infty U r \mathrm{d}r. \tag{5.30}$$

5.5.3 Results using S_a

The results of the Profile A–E cases and the data from Billant *et al.* reinterpreted using the swirl ratio S_a show that the introduction of an integrated axial velocity does not improve the collapse of the profiles to a single critical swirl ratio S_{ac} (see figure 5.16). Using this swirl ratio has led to the

amplification of the Reynolds number dependency of the results, which is problematic in the Profile B case.

Encouragingly, the data from Billant *et al.* coincides with that of the top-hat Profile D at $S_{ac} \approx 2$. This could give some indication that the use of $\bar{U}$ is removing the effect of the velocity profile in the data of Billant *et al.* . This is however not supported by the other velocity profiles tested. The critical swirl ratio of the Profile A case shows a significantly increased discrepancy and the Profile C case has increased dramatically to $\approx 50\%$ greater than the data of Billant *et al.* (1998).

The movement of these critical swirl ratios can be explained by observing the difference between the individual U_0 and $\bar{U}$ pairs. The Profile C case, being the furthest from the top-hat profile, has a centreline velocity $U_0 \approx 2.8$, while its averaged velocity is $\bar{U} \approx 1.2$. Such a large discrepancy leads to dramatically increased critical swirl ratios, when interpreted with S_a. For the cases where the velocity profile is nearer to a top-hat profile, the critical swirl ratios increase only slightly.
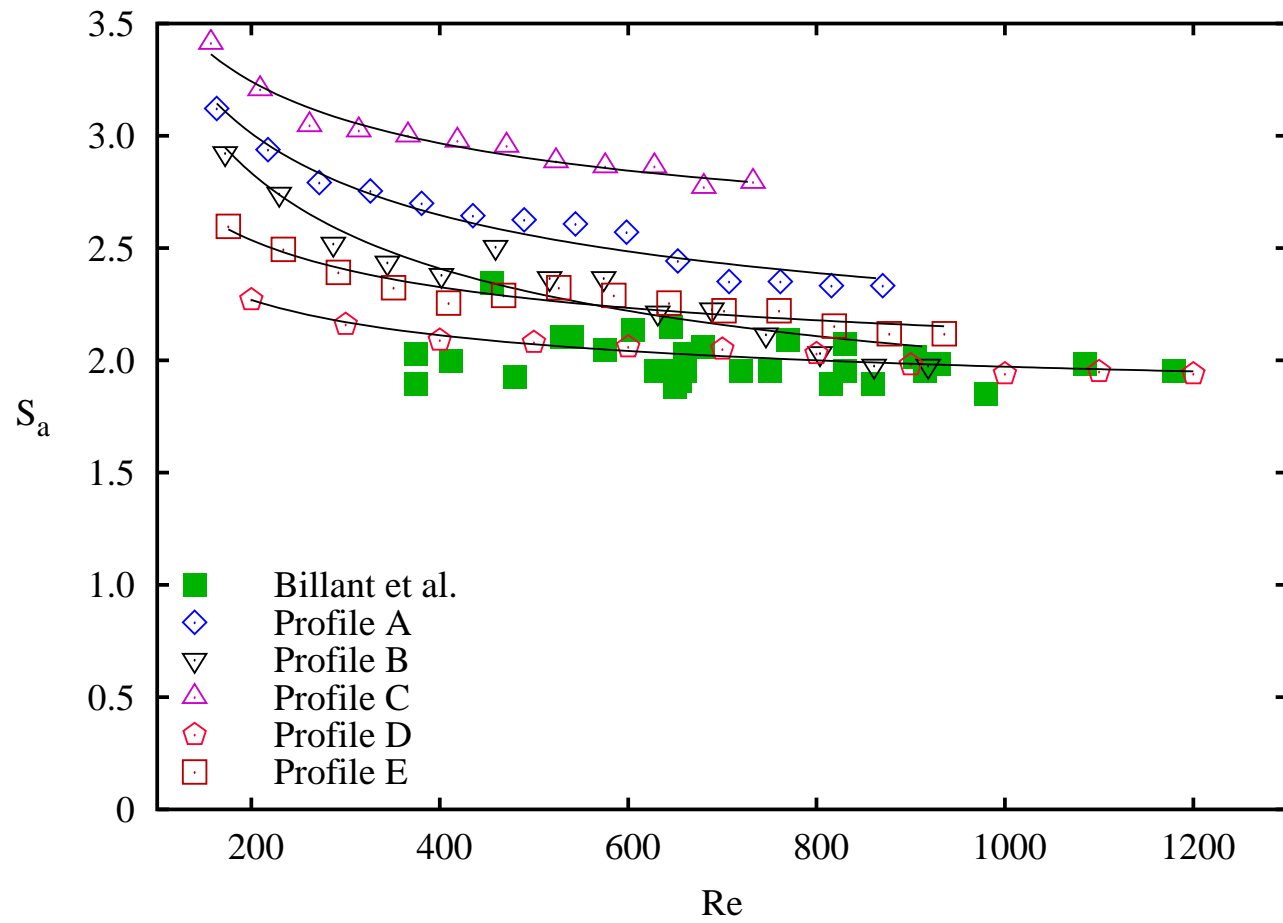
Figure 5.16: Critical swirl ratios for all profiles tested and for the data of Billant *et al.* as interpreted with the swirl ratio S_a.

In light of these results and maintaining the core hypothesis, it may be interpreted that a variation in axial velocity may cause more far reaching effects than previously thought. It is possible that the axial velocity profile shape has a dramatic effect on the azimuthal properties also. One parameter in particular is affected by the axial velocity variation is the azimuthal velocity. This leads to an adjustment of the original hypothesis such that the azimuthal velocity profile perhaps should also be integrated to account for the axial profile effects within itself.

In the following section, the parameter $\bar{W}$ is developed based on the angular momentum, in a manner similar to that presented above.

5.5.4 Introducing Azimuthal Bulk Properties

In this section, the variable azimuthal velocity profile is represented by the constant representative velocity $\bar{W}$. The problem related to the coupling of the axial velocity within the azimuthal flow is treated through integrating the axial and azimuthal velocity profiles together, with respect to angular momentum flow rate $\dot{M}_\theta$. Figure 5.17 shows a graphical representation of the concept. The azimuthal velocity is represented by the constant velocity $\bar{W}$ and, as before, the axial velocity is represented by the constant velocity $\bar{U}$.

The equivalent azimuthal velocity $\bar{W}$ is derived as follows. The angular momentum flow rate $\dot{M}_\theta$ of a non-uniform azimuthal velocity profile $W(r)$ in an axisymmetric and incompressible jet is given by

$$\dot{M}_\theta = \int_0^\infty Wr\mathrm{d}\dot{m}, \tag{5.31}$$

where $\mathrm{d}\dot{m}$ is the mass flow rate increment, represented by
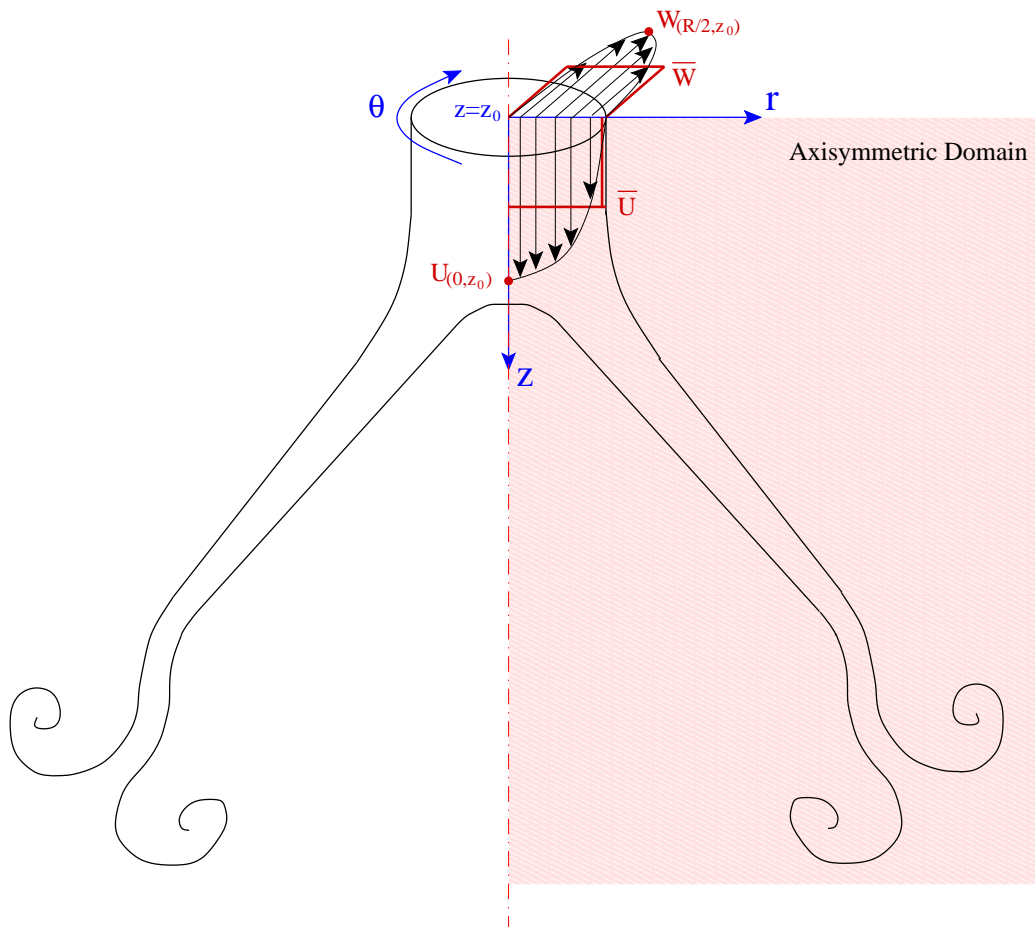
Figure 5.17: The equivalent constant velocities $\bar{U}$ & $\bar{W}$ for the same axial mass flow rate and the angular momentum flow rate, respectively.

$$\mathrm{d}\dot{m} = \rho U 2\pi r \mathrm{d}r, \tag{5.32}$$

giving

$$\dot{M}_\theta = 2\rho\pi \int_0^\infty U W r^2 \mathrm{d}r. \tag{5.33}$$

Assuming that there are equivalent uniform axial $\bar{U}$ and azimuthal $\bar{W}$ velocities over the domain $0 \le r \le R$ with an angular momentum flow rate given by

$$\dot{M}_{\theta e} = \frac{2}{3}\rho\pi R^3 \bar{U}\bar{W}. \tag{5.34}$$

Equating the angular momentum ($\dot{M}_{\theta e} = \dot{M}_\theta$) gives

$$\frac{2}{3}\rho\pi R^3 \bar{U}\bar{W} = 2\rho\pi \int_0^\infty U W r^2 \mathrm{d}r \tag{5.35}$$

and hence $\bar{W}$ is described by

$$\bar{W} = \frac{3}{R^2\bar{U}} \int_0^\infty U W r^2 \mathrm{d}r. \tag{5.36}$$

Now using a similar formulation to the criterion proposed by Billant *et al.* , a new swirl ratio S_* is proposed where the axial and azimuthal velocity components of S are replaced by the integrated parameters $\bar{U}$ and $\bar{W}$, as defined here

$$S_* = \frac{2\bar{W}}{\bar{U}} \tag{5.37}$$

Given that the parameters $\bar{U}$ and $\bar{W}$ describe the equivalent axial and azimuthal velocities, then the critical swirl ratio should remain the same as that in the analysis of Billant *et al.* , such that the critical swirl ratio $S_{*c} \approx \sqrt{2}$.

5.5.5 Results using S_*

Recalculation of the swirl ratios based on the parameter S_* reveals a remarkable collapse for all cases except the Profile D case (see figure 5.18). For the Profile A,B,C and E cases the critical swirl ratios lie within a spread of $\delta S_* < \pm 10\%$. Additionally, the data from Billant *et al.* also collapses to the same critical swirl ratio. Upon closer analysis of this data, it is apparent that the ratios of averaged to maximum velocities are approximately the same for both the axial and the azimuthal velocities, as follows

$$\left(\frac{\bar{U}}{U_0} \approx \frac{\bar{W}}{W_0} \right)_{\text{Billant}} \tag{5.38}$$
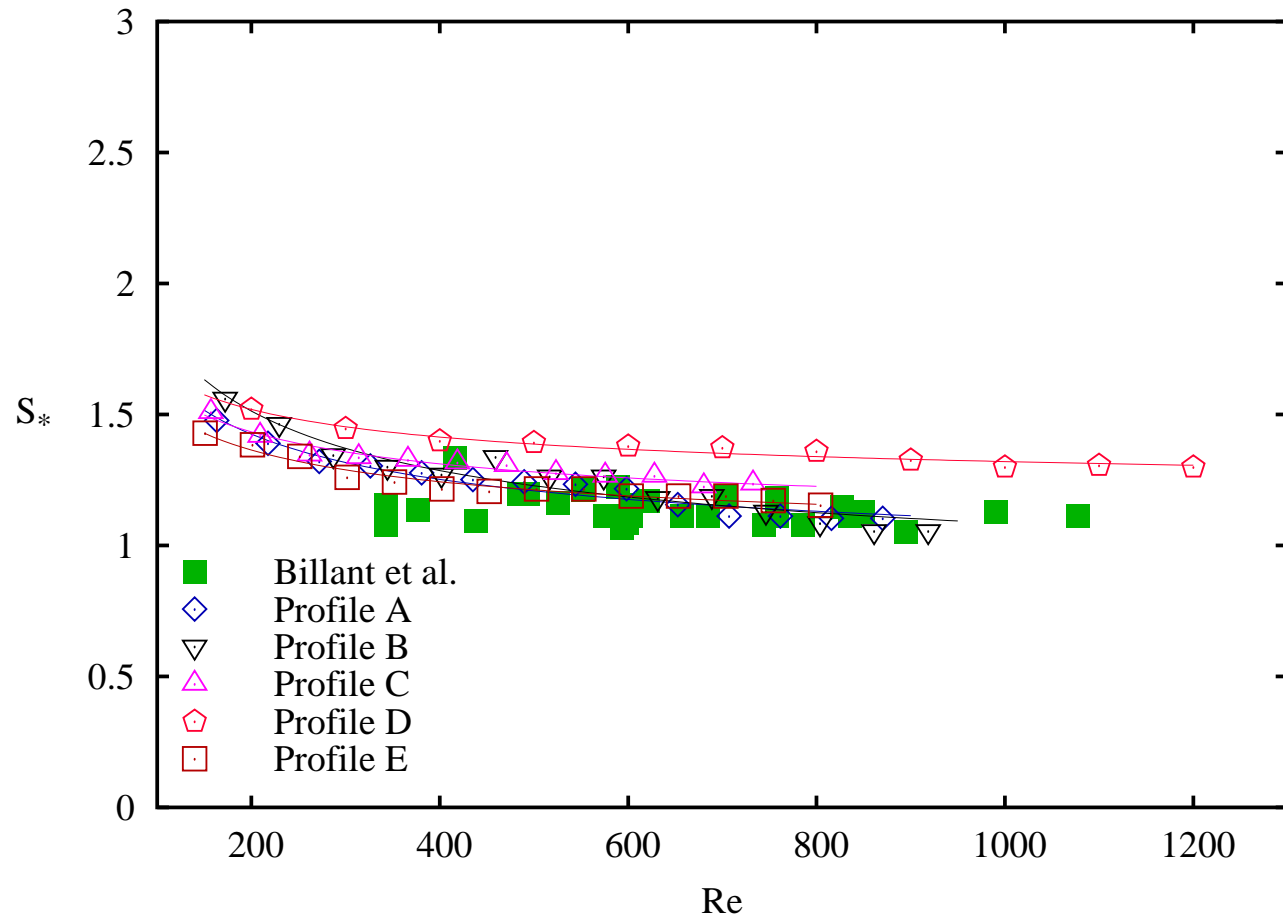
Figure 5.18: Critical swirl ratios for all profiles tested and for the data of Billant *et al.* as interpreted using the swirl ratio S_*.

This property of the $S = 1.33$ velocity profile measured by Billant *et al.* means that both the swirl ratio S and the swirl ratio S_* give approximately the same critical value. The question that this poses is: in the absence of the peak on the centreline of the axial velocity, how well will the swirl ratio S represent the critical swirl ratio derived in the analysis?

The profile D case lies at $\delta S \approx 15\%$ greater than the other cases. This result may be due to the strong outer flow of the jet helping to keep the centreline velocity from stagnation. Some evidence to suggest that this may be the case is shown in figure 5.19. Here, axial and azimuthal velocity profiles are given above and below the centreline, respectively. The profiles are shown for a variety of downstream locations of a jet at $Re \approx 350$ and a swirl ratio of $S = 0.9$. After the jet leaves the nozzle, a velocity defect begins on the centreline. Immediately adjacent to the centreline is a large flux of high velocity fluid that causes a net shear stress on the flow at the centreline, such that the velocity defect is suppressed. The result of this may be that the swirl ratio for vortex breakdown for this case needs to be stronger to overcome the bulk flow.

The Profile B case has a slightly higher critical swirl ratio in the low Reynolds number range. This may be indicative of the same effect that can be seen in the Profile D case. In this case however, the centreline velocity is smaller and the overall momentum flow rate is smaller than the Profile D case, which suggests that the increase in swirl ratio is only a low Reynolds number effect, where the shear stresses are higher.

In total, the Profile A, C and E cases show a remarkable collapse with the data of Billant *et al.* , perhaps indicating that for a range of profiles with similar characteristics, the swirl ratio S_* is much closer to a universal classification parameter.
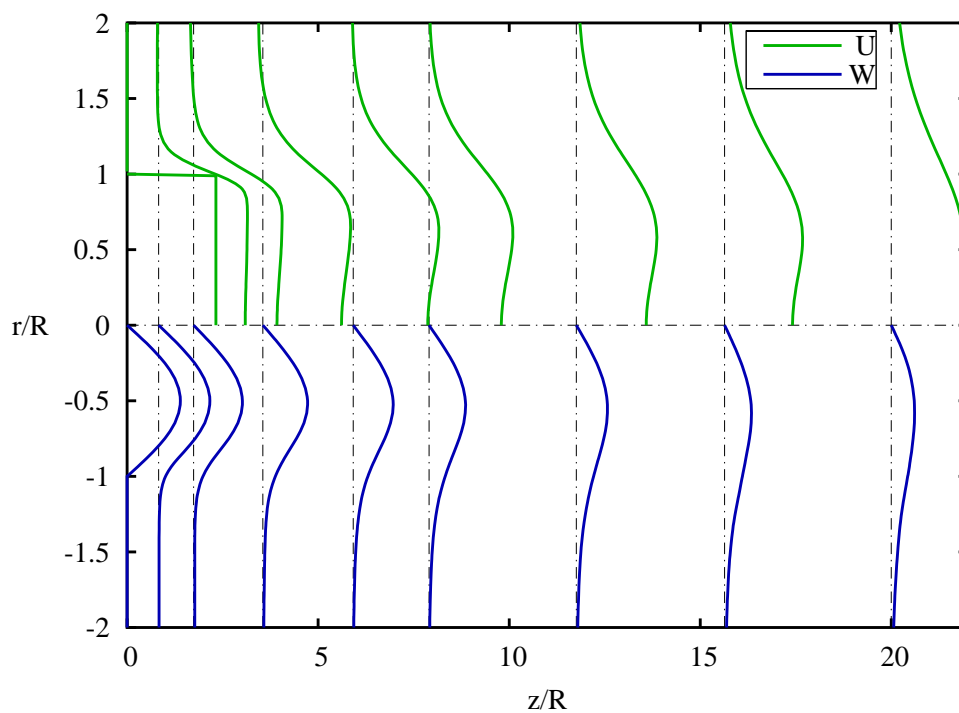
Figure 5.19: Axial (above $r/R = 0$ centreline) and azimuthal velocity (below centreline) profiles for a variety of downstream locations for a swirling jet at $Re \approx 350$, $S = 1.1$ with the velocity profiles of the Profile D case.

5.5.6 Application of S_* to Alternative Experimental Profiles

Farokhi *et al.* (1989) suggest a swirl ratio based on total angular momentum and total momentum flow rate, including the turbulent stresses within the integrands (see §2.2.4). They applied this criterion to two turbulent swirling jets that had the same swirl ratio but markedly different azimuthal velocity profiles. Their results show that although both jets have the same swirl ratio, one experienced vortex breakdown while the second did not. They went on to argue that integrated swirl ratios are insufficient to describe the condition of a vortex with respect to vortex breakdown.

Time averaged axial and Azimuthal velocity profiles for the two cases are published in Farokhi *et al.* (1989), for a variety of axial locations downstream. These profiles indeed show that one jet experiences no breakdown, while the other has a strong velocity defect on the centreline of the axial velocity profiles, becoming approximately stagnant at $z/D = 4$ downstream of the nozzle.

Application of the swirl ratio S_* to the two jets, allows a different conclusion to that reached by Farokhi *et al.* (1989). The swirl ratio for the two cases is calculated using the trapezoidal rule over the data extracted from the published profiles, giving $S_* = 1.27$ and $S_* = 1.37$ for the non-breakdown case and the breakdown case respectively. This result explains the presence of breakdown in one jet but not the other. The case that displays no breakdown has an integrated swirl ratio less than, but close to that at which breakdown is measured in the previous section (§5.5.5), while the case that displays breakdown has an integrated swirl ratio that is within the range where breakdown is measured.

5.5.7   The Swirl Ratio as a Local Parameter

In order to better understand the relevance of swirl ratios to swirling jets and their potential to describe the criticality of a swirling jet, a series of simulations with increasing swirl ratio were performed. The swirl ratios simulated were $S = 0.0$, 0.1, 0.2, ..., 1.4 for the one Reynolds number $Re \approx 350$. The velocity profiles used in the simulations were the same as those used in the Profile E case, which gives a critical swirl ratio for vortex breakdown of $S = 1.40$. Hence, all cases tested, except with $S = 1.40$, had swirl ratios less than the critical swirl ratio for vortex breakdown. The final breakdown location – defined as the location of the upstream stagnation point – for this case is $z/R = 1.5$. In the case of the $S = 1.4$ simulation, a velocity field where the vortex breakdown region is swept downstream is chosen.

Figures 5.20 and 5.21 show a series of contour plots of some of the simulated velocity fields used in these tests. The swirl ratios shown are $S = 0.0$, 0.5, 0.9, 1.2, 1.3 & 1.4 consecutively. Only the $S = 1.3$ and $S = 1.4$ contours show a slight reversal of flow at the outer boundary indicated by the blue contours at the $r/R = 10$ level; the reversal of flow becomes important in the integrations needed to obtain the parameter S_*. The contours for the $S = 0.0$ and $S = 0.5$ cases show that at no point downstream does the centreline velocity decrease below $U = 1.0$. The $S = 0.9$ case shows that the velocity defect is starting to reach further upstream; a decrease in the centreline axial velocity to less than $U = 1.0$ is evident after $z/R = 16$. The contours for $S = 1.2$ show more signs of the effect of swirl on the centreline velocity, with a strong stagnation building on the centreline. Further increases in swirl to $S = 1.3$ and $S = 1.4$ show strong deceleration on the centreline and in the case of $S = 1.4$, the velocity has stagnated and reversed

Figure 5.20: Contours of constant axial velocity for three swirling jets at $Re \approx 350$, with swirl ratios $S = 0.0, 0.5, 0.9$ from top to bottom. Here the contours cover the range $-1.0 \leq U \leq 1.0$ and there are 20 levels with red indicating positive velocity, white indicating zero velocity and blue indicating negative velocity.
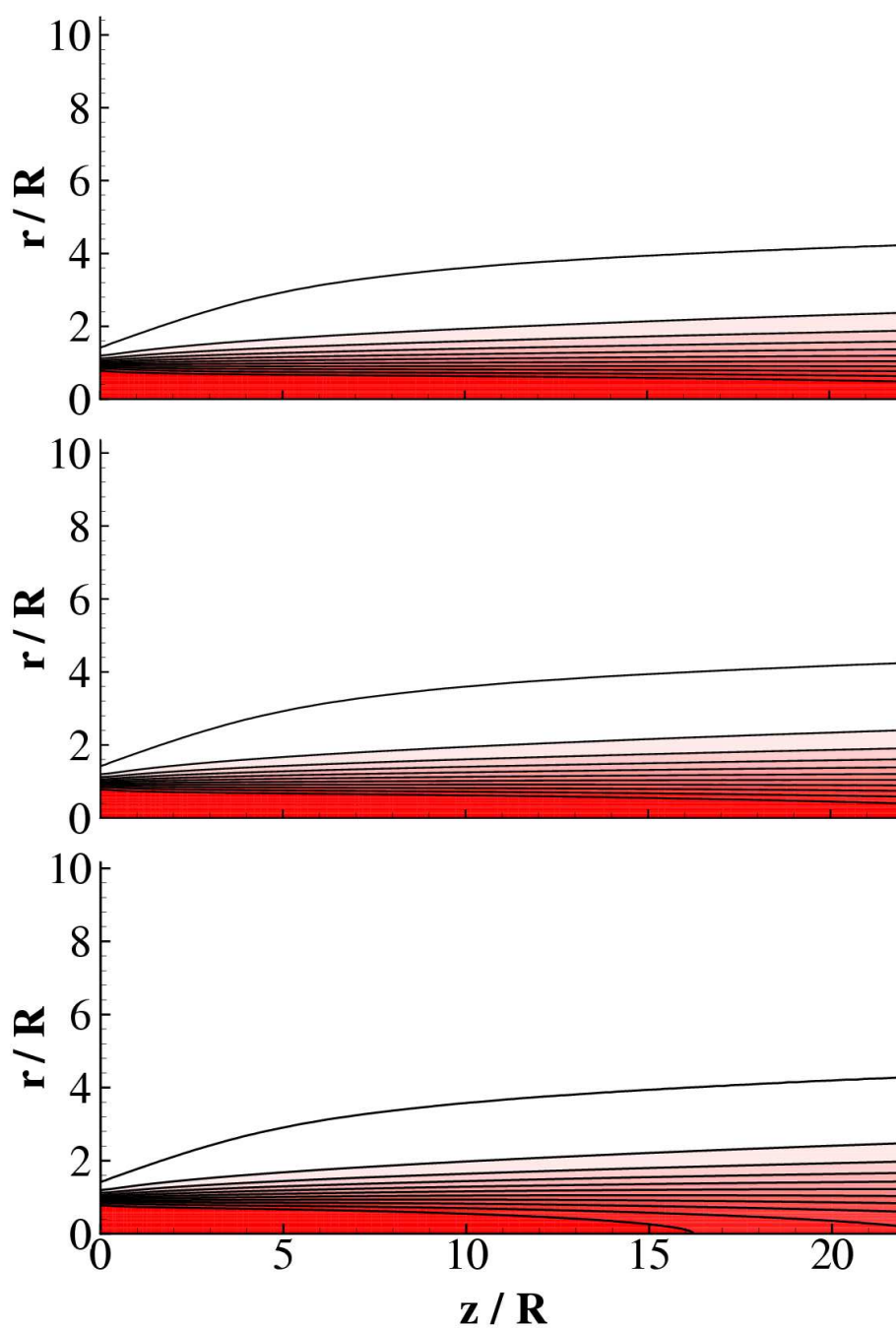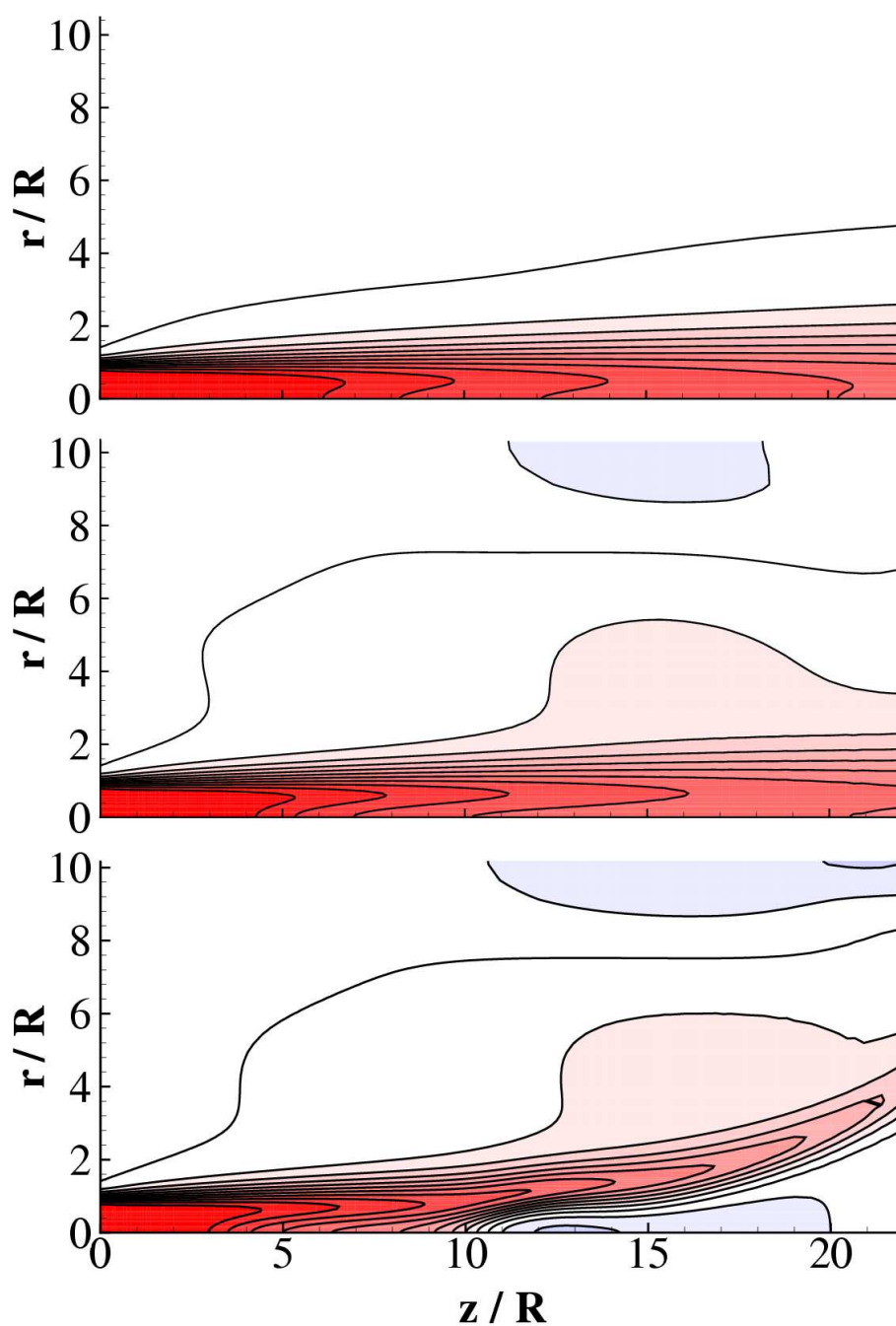
Figure 5.21: Contours of constant axial velocity for three swirling jets at $Re \approx 350$, with swirl ratios $S = 1.2, 1.3, 1.4$ from top to bottom. Here the contours cover the range $-1.0 \leq U \leq 1.0$ and there are 20 levels with red indicating positive velocity, white indicating zero velocity and blue indicating negative velocity.

after $z/R = 12$.

Each simulation, except the $S = 1.4$ case, was run to a steady state; this was assumed to be reached once the velocity profiles downstream were unchanging. A selection of velocity profiles were then extracted from each steady velocity field at distances from the nozzle of $z/R \approx 0$, 1, 2, 4, 6, 8, 12, 16, & 20. Each velocity profile extends radially across the entire computational domain and contains axial U and azimuthal W velocity data. Figure 5.22 shows an example of the profiles collated from the data. The velocity profiles are given for each location stated above, as the jet progresses downstream. At $r/R = 0$, the centreline is represented by a broken black line and perpendicular to this line are broken black lines indicating the location that each profile was taken. Associated with each location is an axial velocity profile (green line) which is drawn above the centreline, and an azimuthal velocity profile (blue line) drawn below. The swirl ratio for this case is $S = 0.9$, which can be verified by measuring the peak velocities U_0 and W_0 of the profile at the nozzle outlet $z/R = 0$. A scale is not given for the velocities, however each profile is drawn using the same scale.

Evident from these velocity profiles is a normal process of diffusion of the axial velocity profile in the radial direction, necessitating a reduction in the maximum velocity as the jet moves downstream. As the velocity profile used in these simulations was obtained using a spline fit of the velocity profiles published in Billant *et al.* , they therefore include a small peak in the centreline axial velocity. This peak is evident up until $z/R \approx 6$, beyond which the velocity profile has been affected by the viscous effect, such that the idiosyncrasies of the initial velocity profile are now negligible. Similarly with the azimuthal velocity profile, the diffusion effects cause a spreading of the profile and a reduction of the maximum azimuthal velocity.
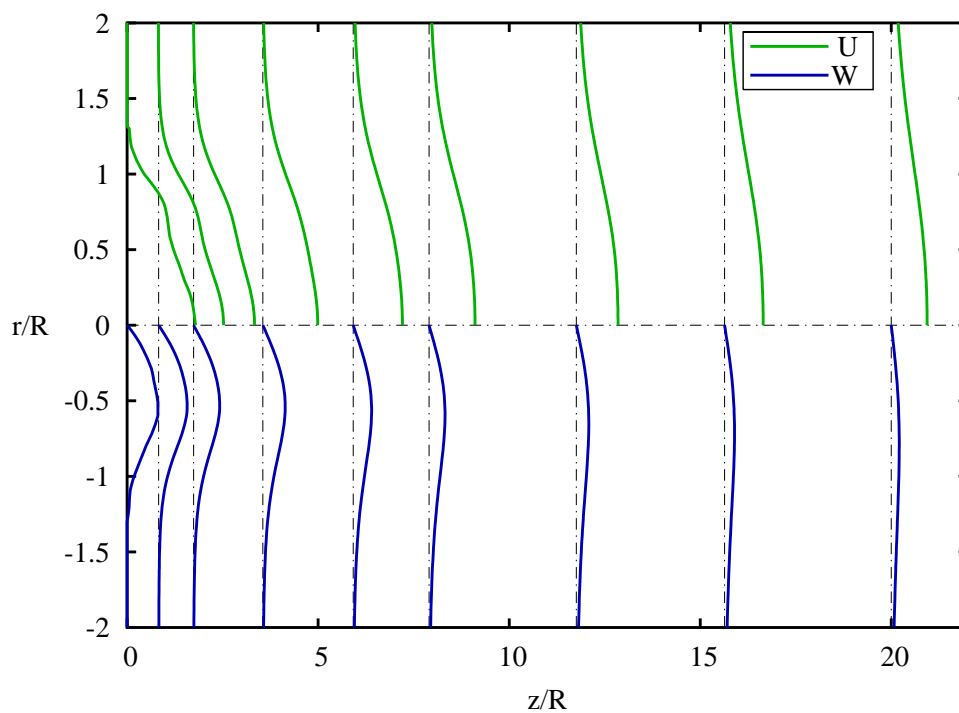
Figure 5.22: Axial (U) and azimuthal (W) velocity profiles given at a variety of distances downstream of the nozzle ($z/R = 0$) for a simulation of a jet with the parameters $Re \approx 350$ and $S = 0.9$.

The diffusion and subsequent reduction in axial and azimuthal maximum velocities will affect the swirl ratio. Billant *et al.* (1998) analysed a vortex just before a stagnation point and concluded that for a stagnation point to occur, there must be a swirl ratio of $S \geq \sqrt{2}$ upstream . We are therefore able able to observe a swirling flow at any location downstream and be sure that if the swirl ratio locally is greater than this condition, then there must form a stagnation point closely downstream.

In this section the swirl ratios S and S_* are discussed as local parameters. The swirl ratios were previously only applied at the nozzle outlet, and from now, on will be referred to as the initial swirl ratio and represented by the symbols S and S_*. The initial values of swirl are thought to be able to characterise the flow for all downstream locations (based on the analysis by Billant *et al.* (1998)). A local version of each of these, referred to as S_l and S_{*l}, are also used throughout the section. This local parameter denotes the use of the swirl ratio, measured at each downstream location, to characterise the flow; whereas, the parameters S and S_* are generally applied at or near the nozzle. In the case of the initial swirl ratios S and the local swirl ratio S_l, maximum velocity measurements are obtained from the extracted data at the pertinent locations. In the case of the initial swirl ratio S_* and the local swirl ratio S_{*l}, the complete velocity profiles are integrated using the trapezoidal rule.

Figure 5.23 shows the results of calculating a local swirl ratio (as defined by Billant *et al.* and referred to here as S_l) for each jet simulation. Note that the local swirl ratio at the nozzle exit corresponds to the initial swirl ratio S. Hence, at $z/R = 0$, the swirl ratio increases from $S = 0.0$ to $S = 1.4$ in steps of $\delta S = 0.1$. Immediately obvious is a trend at initial swirl ratios $S \leq 1.0$ for the local swirl ratio to monotonically decrease as a function

of downstream distance. An explanation for this can be seen in figure 5.22 where the maximum azimuthal velocity component decreases at a greater rate than that of the axial velocity, such that at $z/R = 20$ there is a large discrepancy and therefore a much lower swirl ratio than that measured close to the nozzle. The effect becomes more pronounced with increasing outlet swirl ratio, such that for an initial swirl ratio of $S = 1.0$, the local swirl ratio at $z/R = 20$ is approximately 50% smaller.
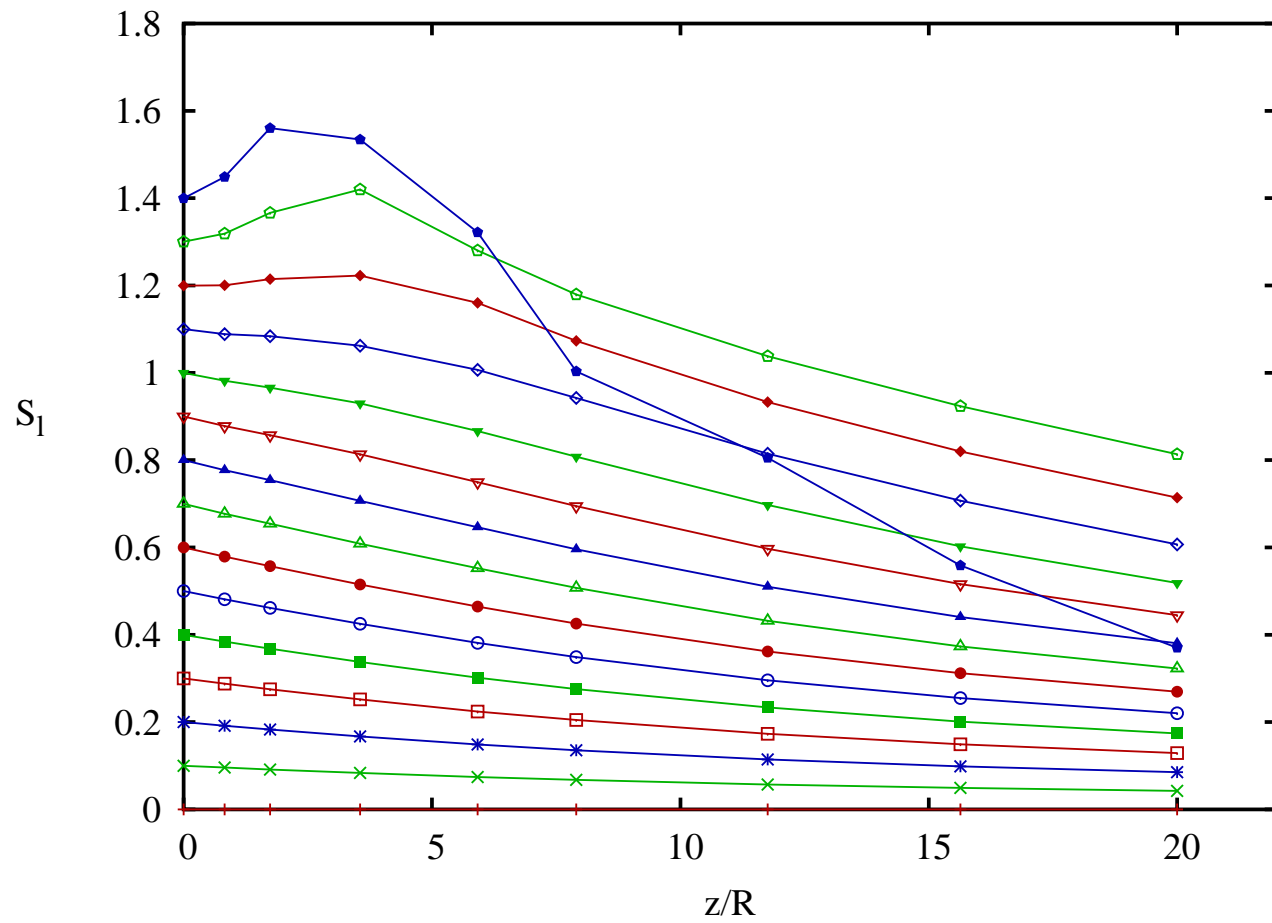
Figure 5.23: The swirl ratio S at a variety of distances downstream of the nozzle for a range of simulations with increasing initial swirl ratio.

Another effect seen in the local swirl ratio S_l is the change in gradient at the near-nozzle region ($0 \leq z/R \leq 4$). For initial swirl ratios of $S \leq 1.1$, the local swirl ratio is always decreasing with downstream distance. However, for $S \geq 1.2$ the local swirl ratio increases in the near-nozzle region, up to a maximum value, after which there is a turning point and the local swirl ratio once again decreases. For the critical swirl ratio case ($S = 1.4$), where there is a stagnation and reversed flow zone at $z/R = 12$, the local swirl ratio varies widely with downstream distance. That is, the initial swirl ratio is $S = 1.4$, while the local swirl ratio at $z/R = 4$ is $S_l \approx 1.55$ and the local swirl ratio at $z/R = 20$ is $S_l \approx 0.4$. Applying the criterion of Billant *et al.* at each of these locations gives a different story. At least, with a maximum swirl ratio of $S = 1.55$, the vortex should be experiencing a strong breakdown at the near nozzle region. In this case however, there is only a transient breakdown state downstream at $z/R = 12$.

The results of this analysis show that the swirl ratio as defined by Billant *et al.* lacks consistency when applied locally. Additionally, it is widely observed that vortex breakdown occurs downstream of the nozzle and propagates upstream due to the imposition of a stronger adverse pressure gradient on the vortex core by the stagnation point itself. The result of applying the swirl ratio S at downstream locations shows that swirl ratios are almost always smaller than the required critical condition of $S \approx \sqrt{2}$, as defined by Billant *et al.* (1998). Indeed, in the case of the $S = 1.4$ simulation, a transient and unsteady stagnation (or strong deficit) is seen to occur at $z/R > 12$. Slightly upstream of this point, the local swirl ratio is not much more than $S_l = 1.0$.
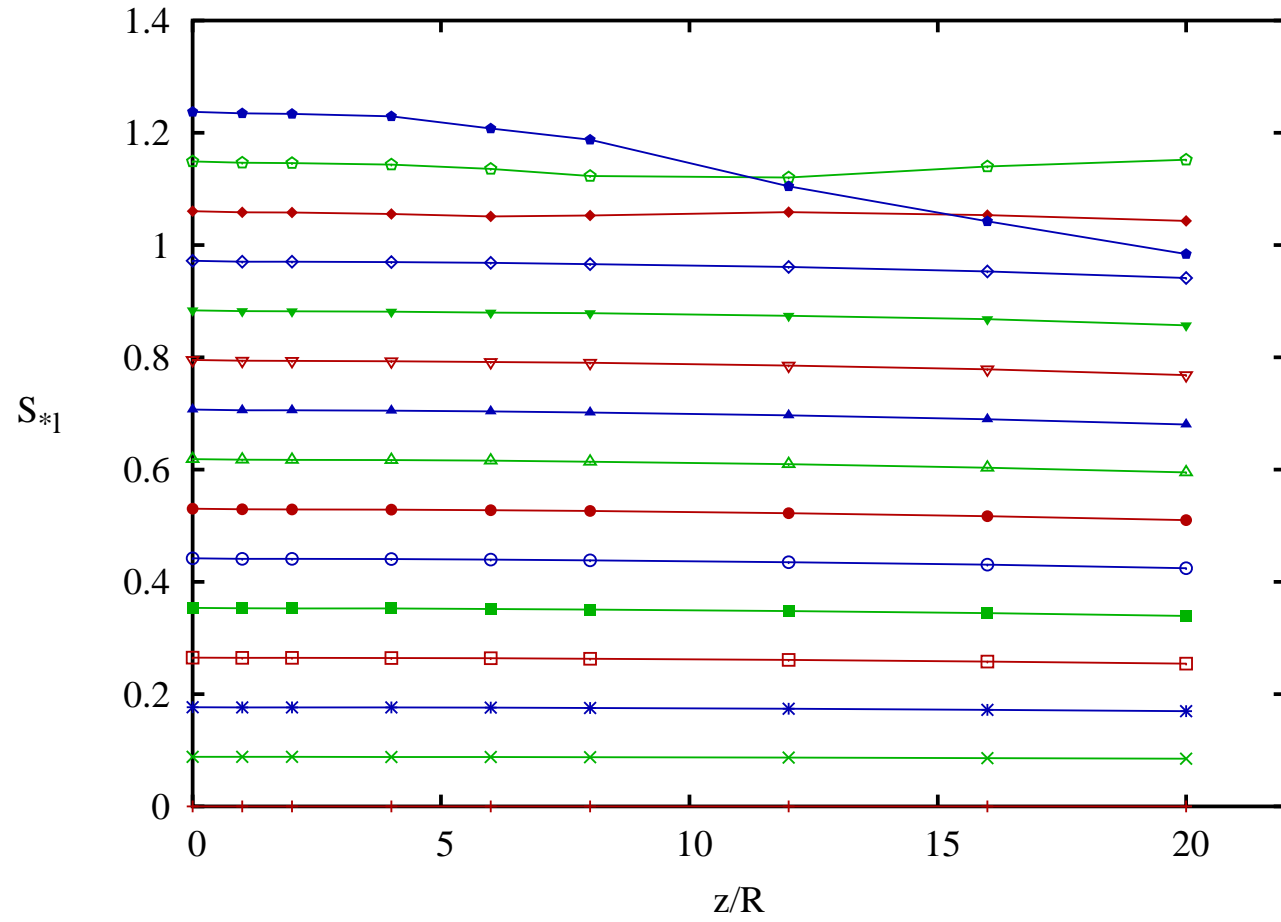
Figure 5.24: The swirl ratio S_* at a variety of distances downstream of the nozzle for a range of simulations with increasing global swirl ratio.

Using the integrated parameter S_* to describe the vortex core for a variety of downstream distances yields a much better description of the vortex core that is more consistent with the critical state theory. Figure 5.24 shows the results of the simulations as interpreted using the swirl ratio S_* as calculated locally. Immediately noticeable is the constant swirl ratio behaviour for all downstream locations measured. The constant behaviour breaks only at the near-breakdown swirl ratios of $S_* \approx 1.15$ and $S_* \approx 1.25$, probably due to the introduction of reversed flow into the integrations (see figure 5.21). The consistency of the swirl ratio with downstream distance may be expected since it is determined using velocities calculated as a result of integrals of mass flow rate and angular momentum flow rate – both being conserved properties for flows without external forces.

The consistency of the swirl ratio S_* with downstream distance is an important result. It indicates that this parameter can be applied anywhere along a vortex before a recirculation region with the result of giving the same swirl ratio. The loss of consistency with larger swirl ratios may be useful as a predictive measure. That is, if measurements can be taken at two axial locations on a vortex and the swirl ratio S_* is measured to be different at these locations, then vortex breakdown may be incipient or actually present further downstream. This property may prove to be useful in flows with different flow geometries that may not have the same critical swirl ratio as found in swirling jets.

Prediction of the Swirl Ratio for Breakdown Using Centreline Velocity Measurements at Varying Swirl Ratios

At each axial location, the centreline velocity can be extracted, allowing the tracking of the velocity defect for increasing swirl ratio. Figure 5.25 shows the

results of increasing the initial swirl ratio S and the same result as interpreted using the local swirl ratio S_l (upper and lower respectively). Each line shows the centreline axial velocity magnitude as it varies with swirl ratio, at a particular downstream location. The general trend of each curve confirms that as the swirl ratio increases, the centreline velocity at each downstream location decreases. If the trend of the velocity defect with increasing swirl ratio can be extrapolated to velocity stagnation ($U_0 = 0$), then the swirl ratio needed to cause stagnation can be estimated. The data for each initial swirl ratio S are included, however, recognising that the data for the $S = 1.4$ case are marred by the presence of a transient stagnation point at $z/R = 12$, these points are not included in the extrapolations.

The curve for $z/R = 0$ is constant for all swirl ratios, reflecting the imposed velocity at the nozzle outlet. Increases in distance from the nozzle outlet shows a general velocity decrease due to dissipation – evident in the positioning of each of the curves progressively lower with downstream distance. For each progressive increase in swirl ratio, the defect in centreline velocity increases in magnitude, resulting in the dip in each curve to the lower axis. For the upper graph, where the centreline velocity U_0 is plotted as a function of the initial swirl ratio S, the trend in the curves for $z/R = 1, 2, 4$ show a behaviour that suggests there is a vertical asymptote, suggesting the use of a rational function fit. These three curves have been extrapolated using a rational function approximation. Note that for some locations along the curve, the rational function approximation does not converge, giving discontinuities in the curve; generally, the method converges and gives a good fit to the data.

The extrapolations show that for $z/R = 1$ increasing to $z/R = 4$, the swirl ratio required to locally cause a stagnation point on the centreline

decreases from $S \approx 1.92$ to $S \approx 1.68$. This behaviour may indicate that increasing distances downstream require lower swirl ratios to cause vortex breakdown. The corollary of this is that vortex breakdown starts downstream and propagates upstream, similar to visualisations in §4.1.

The $z/R \geq 6$ data show, however, that the behaviour becomes more linear with increasing swirl ratio, after an initial parabolic region ($0 \lesssim S \lesssim 0.8$). Interpretation of these centreline velocities becomes more difficult, hence, no extrapolation is included. There is however a noticeable drop in the centreline velocities for $z/R \geq 12$ at $S = 1.4$; however, due to this region having a very strong stagnation, interpretation is more difficult. This behaviour may suggest a rapid stagnation occurrence, however, it is inconclusive.

Interestingly, interpretation using the local swirl ratio of the downstream centreline velocities causes the behaviour of these curves to become almost always linear with increasing swirl ratio, after the initial parabolic region. This behaviour leads to a linear extrapolation regime that essentially moves the incipience of breakdown much further downstream. In fact, at $z/R = 20$, the predicted swirl ratio for stagnation is $S \gtrsim 1.5$. This implies that the local swirl ratio must be greater than $S = 1.5$ for the core to stagnate. This result shows clear inconsistency with the results of the simulations, where vortex breakdown is incipient at a location of $z/R = 12$ and a swirl ratio of $S = 1.4$. Additionally, vortex breakdown occurs in this flow at a location of $z/R = 1.5$ and a swirl ratio $S = 1.40$. This graph shows that for stagnation at this location, the local swirl ratio needs to be $S_l \gtrsim 3$.

Performing a similar analysis but using the swirl ratio initially and locally as described by S_* gives the two graphs in figure 5.26. Immediately noticeable is the smaller swirl ratios predicted to create a stagnation at the downstream locations of $z/R = 1, 2, 4$, however this is mainly due to the slightly smaller
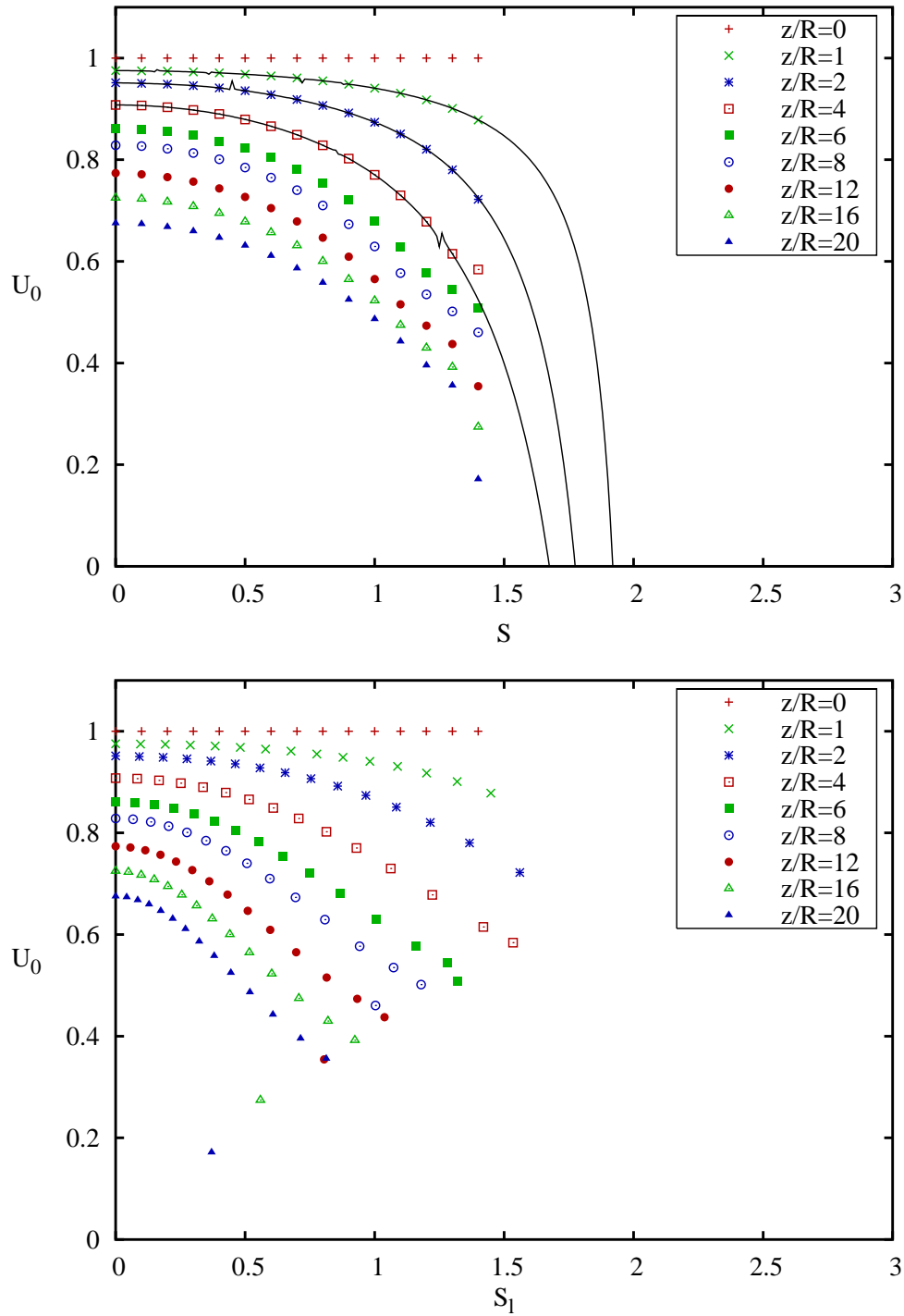
Figure 5.25: The centreline axial velocities as a function of increasing swirl ratio S (upper) and S_l (lower). Here, the curves describing the defect of the axial velocity at $z/R = 1$, 2, & 4 are extrapolated to predict stagnation.

swirl ratios given by the S_* parameter. In this case, the stagnation swirl ratios are predicted to be $S_* \approx 1.62, 1.58, 1.48$ respectively for the distances $z/R = 1, 2, 4$. This shows that for $z/R = 4$ the predicted swirl ratio for vortex breakdown is $S_* = 1.48$. Similarly to the plots using S and S_l, the curves further downstream do not indicate an asymptotic behaviour. However, they do show a rapid stagnation for the last point (referring to the $S = 1.4$ case) at the centreline for the $z/R \geq 12$ locations.

More importantly, due to the conservative nature of the integrations used in the S_* calculation and the constant behaviour of the local swirl ratio for all downstream locations, the corresponding set of curves (the lower graph of figure 5.26) shows the same behaviour as the initial set, in all but the $S = 1.4$ case. Here, the influence of the flow reversal along the outer boundary causes these points to show a different swirl ratio. This comes directly from the drop in swirl ratios seen at the $S = 1.3, 1.4$ cases of figure 5.24.

5.6 Conclusions

The importance of the use of a swirl ratio that uses integrated parameters is shown here, where the swirl ratio S_* is capable of describing the swirling jet's criticality for a variety of swirl ratios within a spread of $\delta S_* \approx \pm 10\%$. Comparitively, the swirl ratio S gives a swirl ratio spread of $\delta S \approx \pm 25\%$. The new swirl ratio provides an experimentally determined, asymptotic critical swirl ratio criterion of $S_* \geq 1.2$, aligning somewhat with the criterion developed by Billant *et al.* (1998).

The swirl ratio S_* was shown to describe the discrepancy in the experiment of Farokhi *et al.* (1989). Two jets with different azimuthal velocity profile formulations were seen to include breakdown in one case and no break-
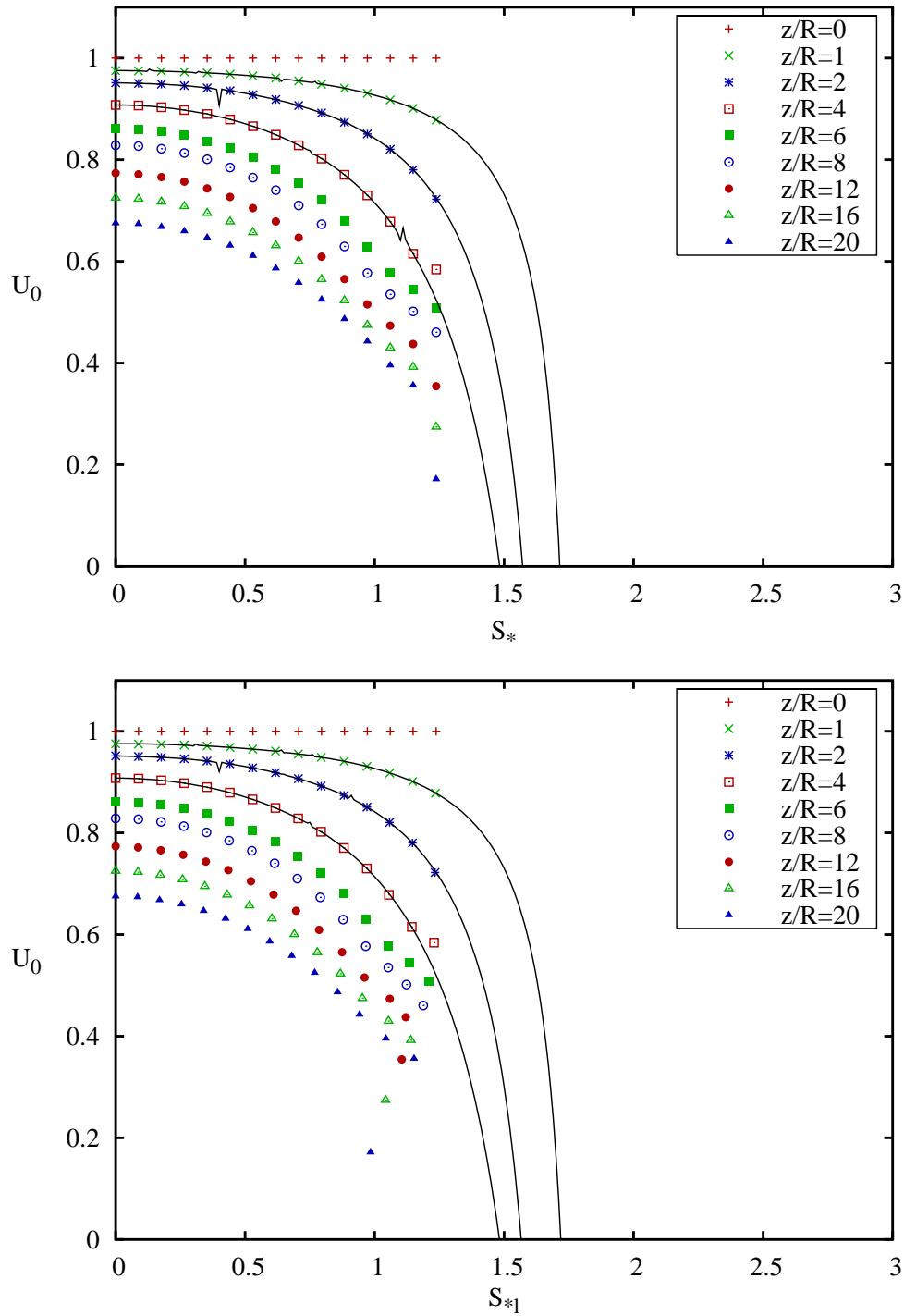
Figure 5.26: The centreline axial velocities as a function of increasing swirl ratio S_* (upper) and S_{*l} (lower). Here, the curves describing the defect of the axial velocity at $z/R = 1, 2, 4$ are extrapolated to predict stagnation.

down in the other. Both jets were calculated to have a swirl ratio $S_f = 0.48$, as defined in Farokhi *et al.* (1989). Recalculation of the swirl ratio gave $S_* = 1.27$ and $S_* = 1.37$, for the jet without breakdown and with breakdown, respectively. The result shows that the jet without breakdown had a swirl ratio that is at the lower end of the range for vortex breakdown, determined here.

Additionally, the proposed swirl ratio S_* describes the vortex for all downstream locations. The parameter allows the same swirl ratio to be deduced from measurements at any location on a swirling jet. The swirl ratio S provides limited accuracy in its critical swirl ratios for a variety of axial velocity profiles. It generally decreases as the jet proceeds downstream. The decreases in swirl ratio downstream causes some difficulty in understanding how a vortex breakdown bubble can begin at a downstream location, where the swirl ratio is lower than the critical condition prescribes.

Chapter 6

Vortex Breakdown
Meta-Stability

Research in the field of vortex breakdown has often been focused on explaining why a particular vortex breakdown state is selected. Benjamin (1962) suggested that the essential mechanism of vortex breakdown is steady and axisymmetric and that the spiral type was created through a build up of asymmetric disturbances. This hypothesis has been supported in the studies of Grabowski & Berger (1976) and Ruith *et al.* (2003), where axisymmetric numerical simulations capture the main flow topologies. Experiments by Kurosaka *et al.* (2003) used a device to create azimuthally propagating disturbances that effected a change to the vortex breakdown state from bubble to spiral and vice versa, linking azimuthal disturbances with the spiral state. Full three-dimensional simulations of the time dependent Navier-Stokes equations for an unconfined vortex were seen to proceed from an axisymmetric bubble state to a spiral state after a build up of asymmetric perturbation in the wake of the bubble (Spall, 1996). Further details regarding vortex breakdown state selection can be read in §2.2.1.
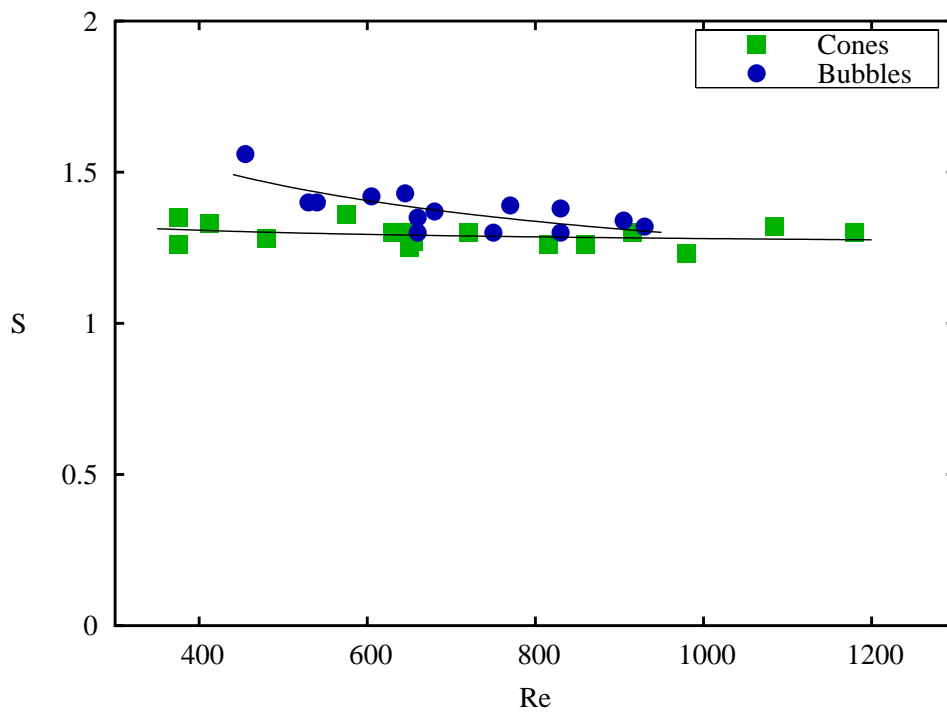
Figure 6.1: Critical swirl ratios for the bubble and cone types of vortex breakdown obtained from the experiments of Billant *et al.* (1998).

Previous studies of vortex breakdown in unconfined swirling jets by Billant *et al.* (1998) have shown that both the bubble- and cone-type of vortex breakdown can occur over a range of Reynolds numbers. Figure 6.1 shows the critical swirl ratios for vortex breakdown for the bubble- and cone-types independently as collated from their figure 4. In this image the occurrence of both the bubble- and cone-types of vortex breakdown across a range of Reynolds numbers is evident. The results show that the critical swirl ratio of the cone-type vortex breakdown is nearly constant with Reynolds number, whereas the bubble-type vortex breakdown shows increased critical swirl ratios at lower Re. This is not to say that bubble breakdown occurs after a cone breakdown, merely that cone breakdown is observed at breakdown inception for slightly lower swirl ratios. Despite the slight discrepancy between the critical swirl ratios for the bubble and the cone, the two breakdown states roughly co-exist for the same parameter range. This co-existence, or bi-stability, poses the question of how the vortex breakdown state is selected.

Billant *et al.* (1998) further investigated the stability of the bubble and cone vortex breakdown states by a series of investigations at swirl ratios slightly greater than the critical swirl ratio S_c. Their tests involved increasing the swirl ratio until a form of breakdown persists, then applying a perturbation to the axial velocity. The results of these tests showed that weak bubble and cone states were destroyed by the perturbation. In the case of the destroyed bubble, the application of more favourable perturbation lead to reformation of the bubble state. Alternatively, in the case of the destroyed cone, the cone was never seen to reappear as a vortex breakdown state; the favourable perturbations did produce a bubble vortex breakdown in some cases. These results suggest that the cone vortex breakdown can occur in a swirling jet with favourable conditions, but bubble breakdown is the pre-

ferred and more stable state. Perhaps the occurrence of the cone is reflective of a particular initial condition of the jet.

In this study, state selection in the simulated axisymmetric swirling jet is explored. A map in Reynolds number versus swirl ratio space, of the vortex breakdown states observed in the jet, is presented based on simulations where the jet is impulsively initiated at a particular Re, S pair. The resulting map describes a well defined region of Reynolds numbers where the initial vortex breakdown state was a bubble, followed by conical breakdown at higher swirl ratios. A second Reynolds number region exists where only a cone state was achieved at the critical swirl ratio; the bubble did not occur at Reynolds numbers above this region. The stability of a bubble to increases in swirl ratio and Reynolds number into the cone-type dominated regions was then explored showing a bubble with strong hysteresis.

6.1 Inlet Boundary Condition

For the tests presented in this chapter, a simplified fit of the $S = 1.33$ velocity profiles, as given in figure 4 of Billant *et al.* (1998) is used as the velocity inlet. Their profile data was normalised with the nozzle radius and the maximum axial and azimuthal velocities respectively. These normalised profiles were then fitted with polynomials using the method of least squares to minimise the error; eighth order and sixth order polynomials providing the best fits respectively. These profiles were cropped at $r = R$ for simplicity. The nodal values of velocity at the inlet boundary condition are interpolated from these polynomials. Figure 6.2 shows the velocity profiles used as compared to those from Billant *et al.* (solid green squares and circles).

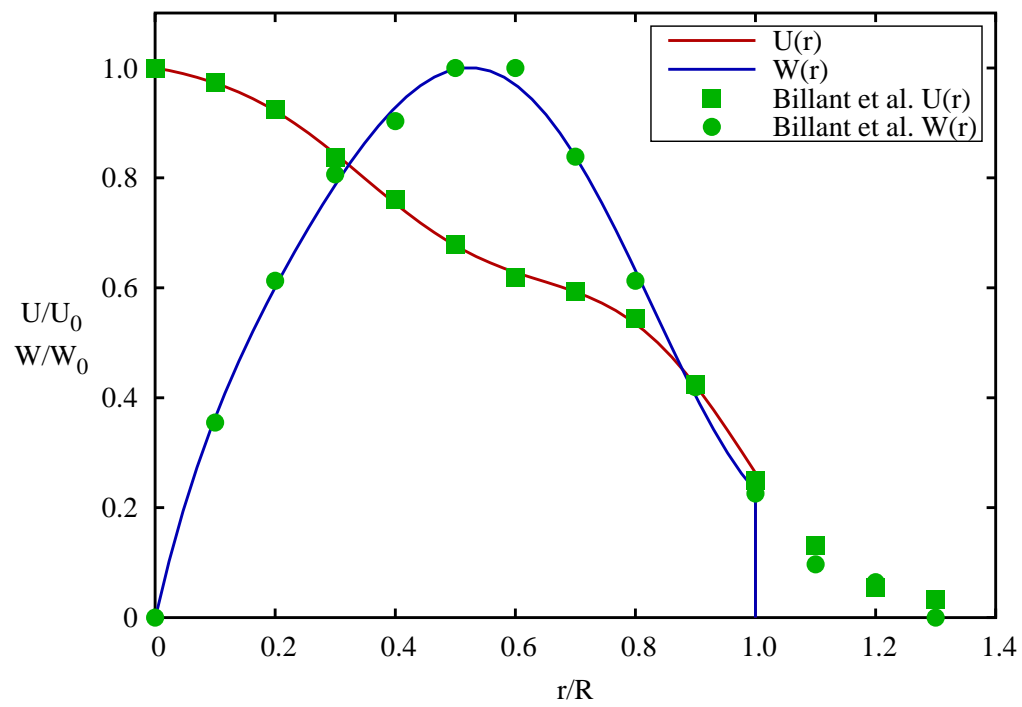The following tests will use the formulation of swirl ratio S as given by

Figure 6.2: The formulation of axial and azimuthal velocity profiles used in the present tests.

Type	Categorisation
small bubble	bubble
large bubble	bubble
hybrid bubble-cone	cone
steady cone	cone

Table 6.1: Method of categorisation of the observed vortex breakdown states.

Billant *et al.* (1998) and defined in equation 5.8.

6.2   State Selection for an Impulsively Initiated Jet

Here a full map of the Reynolds number versus swirl ratio space is developed. The tests used in this section were performed by starting the jet from zero initial conditions at a particular Re, S pair and observing the breakdown state achieved. Each Re, S pair is categorized into either the bubble or the cone. This categorisation is somewhat qualitative as many flow states present examples of both the cone and the bubble. In the case where there the breakdown state is steady (of any size), the recorded state was simple, however, the hybrid bubble-cone state shows examples of bubble and cone behaviour. The hybrid bubble-cone was categorised as a cone since the behaviour shows that the majority of its life is spent in a cone state. Table 6.1 shows how each state is categorised, using the descriptions of the breakdown types as given in §4.

As explained above, the simulation for each Re, S pair was started from zero initial conditions, which necessitated running each simulation for up to $t = 200$–300 to obtain the quasi-steady solution. As each simulation is time-

dependent, care must be taken to accurately describe the vortex breakdown state achieved. Some parameters pairs lead to variable vortex breakdown states, while some can be inherently stable. In cases where the vortex breakdown state is an unstable bubble, the bubble may be periodically swept downstream at initial formation stages of the simulation. Generally, the vortex breakdown state becomes more stable for $t \geq 200$, after which the vortex breakdown state becomes evident.

Figure 6.3 shows the resulting vortex breakdown state map in Re versus S space. The simulations were performed such that the interval between respective swirl ratios becomes smaller at the transition between each state. Transitions from no-breakdown to bubble breakdown, and bubble to cone breakdown were resolved to within the error of $\Delta S = \pm 0.01$. The only exception to this being the low Reynolds number ($Re \leq 300$) transition from bubble to cone breakdown. For these particular Reynolds numbers, the transition from bubble to cone is partially unresolved. The bubble dominates until very large swirl ratios $S \geq 2$ and the transition to the cone state causes the jet to attach to the nearby wall. This attachment stabilises the jet and makes resolving the exact transition difficult. Here it is assumed that the opening of the cone results in the attachment.

The map shows that below a critical swirl ratio S_c, that is partially Reynolds number dependent, the swirling jet experiences no vortex breakdown. This result is reliable, repeatable and based on the definition of vortex breakdown used here; that there must be a flow stagnation point and a recirculation region of limited axial extent (Leibovich, 1978). This critical transition line shows none of the bi-stability that is seen in the results of Billant *et al.* . For Reynolds numbers below $Re \approx 750$, the vortex breakdown type developed at the critical swirl ratio is always the bubble type. Above
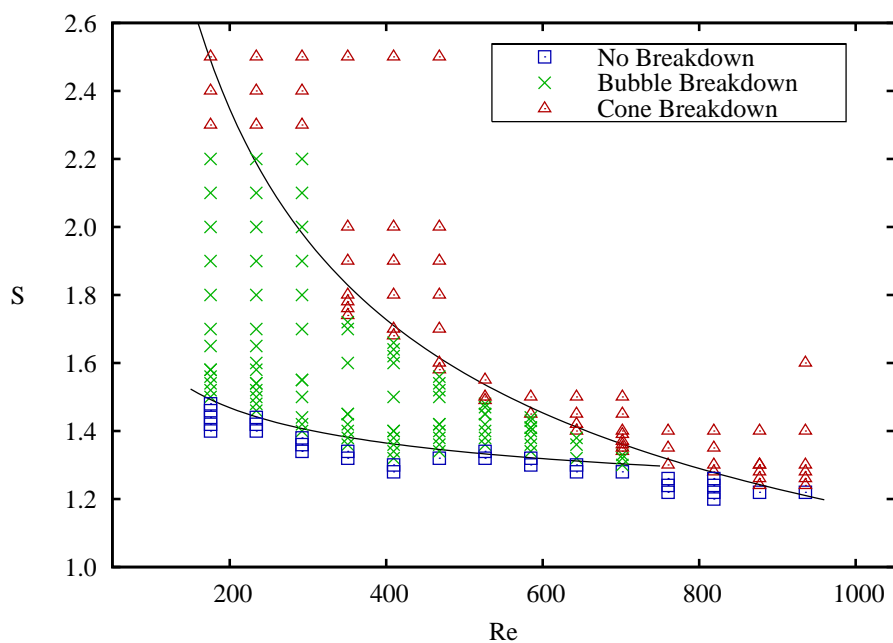
Figure 6.3: Results of a full parametric study of unconfined swirling jet vortex breakdown showing no-breakdown ($\square$), bubble ($\times$) and cone ($\triangle$) states, and the lines that approximately describe the transitions.
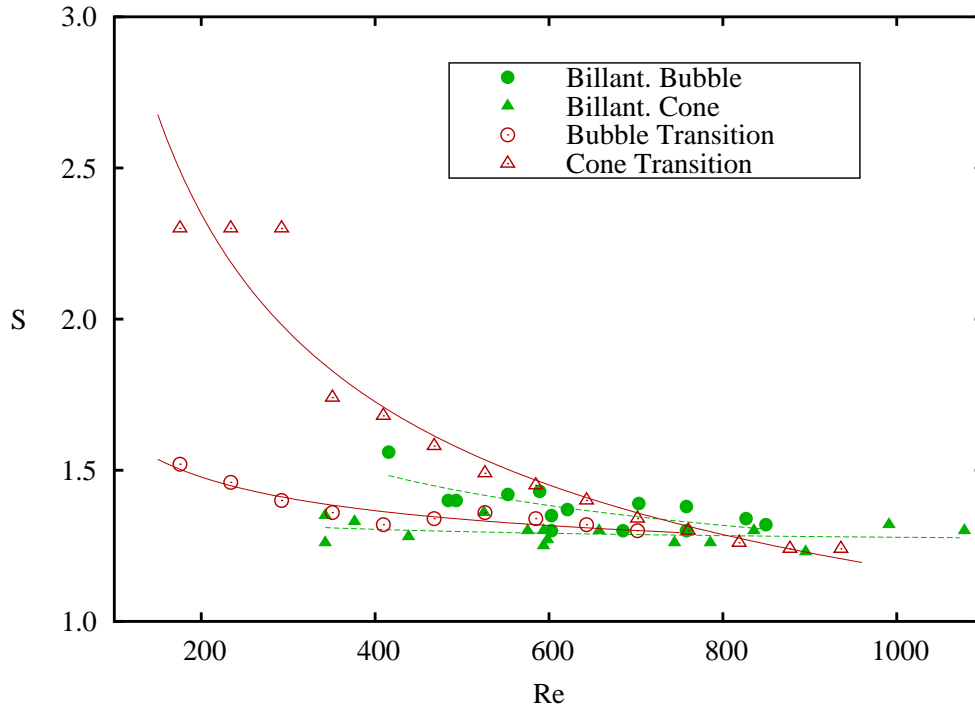
Figure 6.4: A reproduction of the transition data and lines from figure 6.3 superimposed upon the experimental critical swirl ratios of Billant *et al.* (1998). Note that bubble-type breakdown was not observed above $Re \approx 850$.

$Re \approx 750$, the preference switches to the cone type and the bubble type was nearly always absent from these flow, except as a transient state due to oscillations of the cone.

Figure 6.4 shows the transition data and lines from figure 6.4 superimposed upon the experimental critical swirl ratios of Billant *et al.* (1998). This comparison shows interesting similarities and differences between the present simulations and the experiments, and yields some more insight into the state selection question. There is a noticeable similarity between the absence of bubble vortex breakdown at higher Reynolds numbers. The experimental results reproduced here, show that the bubble type was not observed above $Re \approx 850$, corresponding well with the results of the simulations.

There is also some branching of the experimentally observed vortex breakdown states at $Re \lesssim 850$, however, this is not to say that we are observing a similar phenomenon in the simulations. The simulations show that the cone type appears at higher swirl ratios than the bubble. The bubble is always the first type seen (for lower Reynolds numbers). This result is contrary to the experimental observations, where the cone is generally seen at lower swirl ratios than the bubble. These results are unsurprising considering that the experiments used an incremental increase in swirl ratio up to the critical point, whereas the simulations used impulsive initiation of the jet.

The absence of the cone at low swirl ratios may be explained in reference to the different experimental methods. In the case of the simulations, the Re, S parameters were set at the onset of the simulations, leading to a transient vortex breakdown state at near-critical swirl ratios. That is, the vortex breakdown would appear and be swept downstream several times before becoming permanent. The periods where the bubble is absent allow the jet to fully develop and may allow any perturbations (such as the starting vortex) to be swept downstream. The absence of strong perturbation in the nozzle region may explain the absence of the cone. Billant *et al.* identified a possible mechanism in slight temperature differences between the jet and the surrounding fluid causing slight buoyancy effects comparable to the difference in pressure at the stagnation point between the cone and the bubble. An alternative explanation may be given by examining the experimental method of Billant *et al.*; they used incremental increases in azimuthal velocity to approach the critical swirl ratio. It is also possible that the azimuthal perturbation at near-critical swirl ratios is responsible for transition to cone breakdown.

The transition to the cone state in the present simulations (at least for

those in the range $0 < Re \lesssim 750$) is most likely an artifact of the strong starting vortex. The starting vortex is a common phenomena for any jet that is started abruptly, where vorticity at the jet–quiescent fluid boundary, rolls into a large toroidal vortex. This vortex then spreads axially and radially. Observations of the initial stages of the cone vortex breakdown formation shows that the jet attaches to this starting vortex and quickly opens out into a cone.

Although the direct comparison of the experimental results and the simulated results is impossible, it may be that the critical swirl ratios are comparable and independent of the initial conditions. The collapse of a vortex breakdown and its subsequent downstream disappearance yields a jet-like flow field that is independent of the initial conditions, and may just as easily have been created by the incremental increase in swirl. In fact, the experimental and simulated critical swirl ratios show remarkable similarity in magnitude and in its relative independence of the Reynolds number.

6.3   Metastability Tests

In order to test for metastability of the vortex breakdown state, a set of simulations were devised such that cone breakdown transition is approached starting from a stable bubble state. Five Re, S pairs were chosen from the previous parametric study to be the starting cases (see table 6.2). From these five states, two paths of increasing Reynolds number, and three paths of increasing swirl ratio were chosen. Simulations were restarted from a velocity field for each bubble at $t = 200$, then increased in a stepwise pattern in either Reynolds number or swirl ratio. The list of these five tests and their pertinent parameters is given in table 6.2.

Test Number	Starting Parameters	Incremented Parameter Values
1	$Re = 234, S = 2.0$	$S = 2.00, 2.25, 2.30, 2.35, 2.40, 2.50$ 2.60
2	$Re = 409, S = 1.6$	$S = 1.60, 1.65, 1.70, 1.75, 1.80, 1.90$ $2.00, 2.20$
3	$Re = 536, S = 1.4$	$S = 1.40, 1.45, 1.50, 1.55, 1.60, 1.70$
4	$Re = 234, S = 2.0$	$Re = 234, 292, 322, 351, 380, 409, 438$ $497, 556, 614, 643, 702, 760, 819$
5	$Re = 234, S = 1.8$	$Re = 234, 292, 322, 336, 351, 380, 409$ $438, 468, 526, 585, 643, 702, 760, 819$

Table 6.2: Description of the five metastability tests giving the initial starting parameters, and the increments of the test parameter.

Figure 6.5 shows the results of the five metastability tests. Tests 1–3 are represented by a series of vertical blue arrows beginning at the starting parameter of the test and running with constant Reynolds number and increasing swirl ratio, to the highest swirl ratio tested. Tests 4–6 are represented similarly with red arrows that run horizontally with constant swirl ratio and increasing Reynolds number. Each step of test 1–3 is represented by a solid square that is colour coded with relation to the vortex breakdown state attained during each step. In the case of tests 1–3, blue denotes a bubble vortex breakdown and green denotes a cone. For tests 4–6, the bubble vortex breakdown state is described by a hollow red square. Hollow green squares were to be used to denote cone vortex breakdown for these tests. The test results are superimposed upon the transitional values and lines taken from the previous results, using the same symbols (see figure 6.3).

The result of all tests demonstrate that the bubble vortex breakdown state, once it is achieved, is inherently stable. All bar one simulation failed to gain the cone vortex breakdown state when their flow parameters were increased to within the region of cone vortex breakdown, as defined in the parameter mapping study shown previously. Test 1 showed an expansion into a cone state only upon increasing the swirl ratio to $S = 2.6$ which corresponds to a swirl ratio 13% larger than the previously recorded. Test 2 demonstrated even more dramatic suppression of the cone vortex breakdown state with increases of swirl ratio up to 33% higher than previous results failing to produce a cone breakdown state. Similarly, in test 3, increases in the swirl ratio of 13% above the cone transition line, caused little change to the vortex breakdown bubble other than a slight enlargement. Tests 4 and 5 also presented profound steadiness of the vortex breakdown bubble state once fully developed, with increases in swirl ratios of 54% and 38% respectively
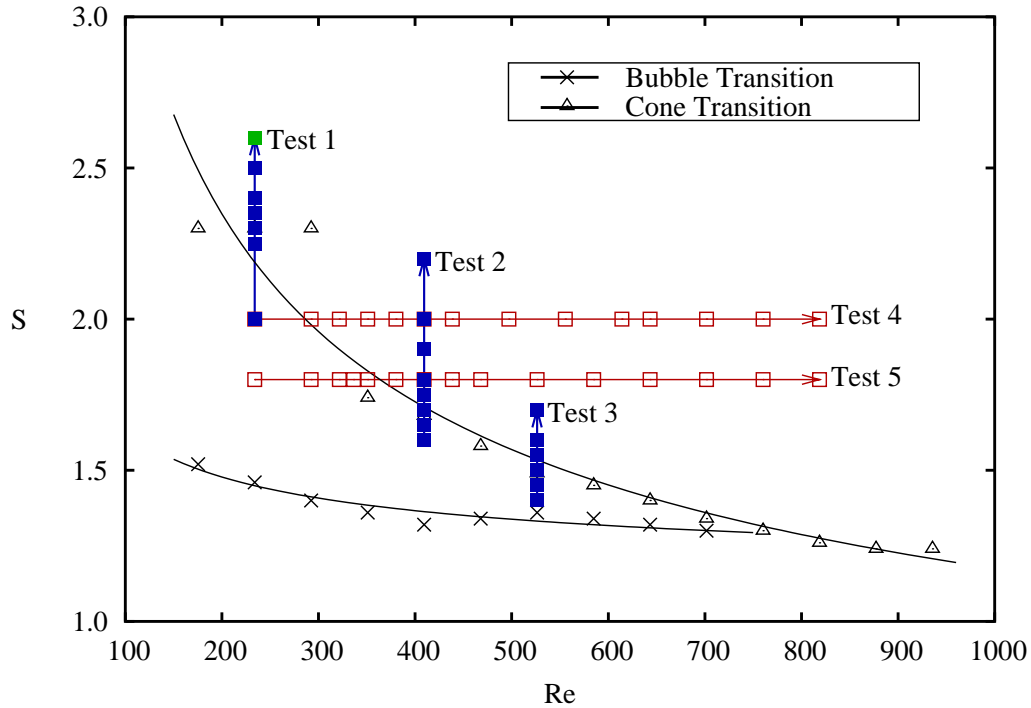
Figure 6.5: Results of metastability tests. The maintenance of the bubble state is represented by solid blue squares for tests 1–3 and hollow red squares for tests 4–5. Note that the single solid green square relates to the only case when the bubble state was destroyed.

demonstrating no change in state.

Considering that the Reynolds number and swirl ratio were increased in a stepwise fashion, the bubbles of each simulation were considerably perturbed at parameter pairs within the cone breakdown region. Surprisingly, for most simulations within this region, these perturbations showed little sign of permanently changing the bubble to a cone. Only at the extremities of the simulations could transitory cones be observed, quickly collapsing back to the bubble state. Examples of this behaviour is shown in figures 6.6 and 6.7. On the left-hand side of both of these images shows the flow at $\delta t = 10$ time units after the last parameter increase. Most cases show that there

is significant distortion of the vortex breakdown bubble. Within $\delta t = 30$, the disturbance was completely gone leaving a steady bubble state (see the right-hand side of each image).

In tests 4 and 5, the bubble extends into a region of reasonably high Reynolds number. In this region, large oscillations of the wake of the bubble were observed. These oscillations resemble those that are formed by the Kelvin-Helmholtz shear layer instability. In the present simulations, the bubble state shows no sign of being affected by the oscillations apart from an increase in unsteady behaviour. This result indicates that vortex breakdown bubbles at these parameters can be extremely stable to external disturbances. Comparatively, as shown in §4.4, the conical shear layers of cone-type vortex breakdown can be highly unstable to shedding, sometimes reforming as vortex breakdown bubbles.

The key parameter for the strength of bubble type vortex breakdown may be the internal pressure. One of the main differences between the cone and the bubble type is the magnitude of the internal velocities. Bubbles tending toward having higher internal velocities and therefore lower pressures. This internal pressure may stabilise any tendency for the wake to open out into the cone state.

6.4   Conclusions

The results presented here are in agreement with the tentative conclusion of the research of Billant *et al.* . The bubble vortex breakdown state is indeed the preferred vortex breakdown state and is inherently stable to reasonable perturbations. The cone state achieved in the present simulations at higher swirl ratios is probably caused by the starting vortex and is a direct effect

(a) Test 2, $S = 2.20$, $\delta t = 10$

(b) Test 2, $S = 2.20$, $\delta t = 30$

(c) Test 3, $S = 1.70$, $\delta t = 10$

(d) Test 3, $S = 1.70$, $\delta t = 30$

Figure 6.6: Flow field in the near nozzle region ten time units (left) and thirty time units (right) after the last increase in swirl ratio ($S = 2.20$ and $S = 1.70$ respectively). The contours show positive (blue) and negative (red) azimuthal vorticity from $-10 < \omega_\theta < 10$ and streamlines are also given for a variety of locations.

(a) Test 4, $Re = 819$, $\delta t = 10$

(b) Test 4, $Re = 819$, $\delta t = 30$

(c) Test 5, $Re = 819$, $\delta t = 10$
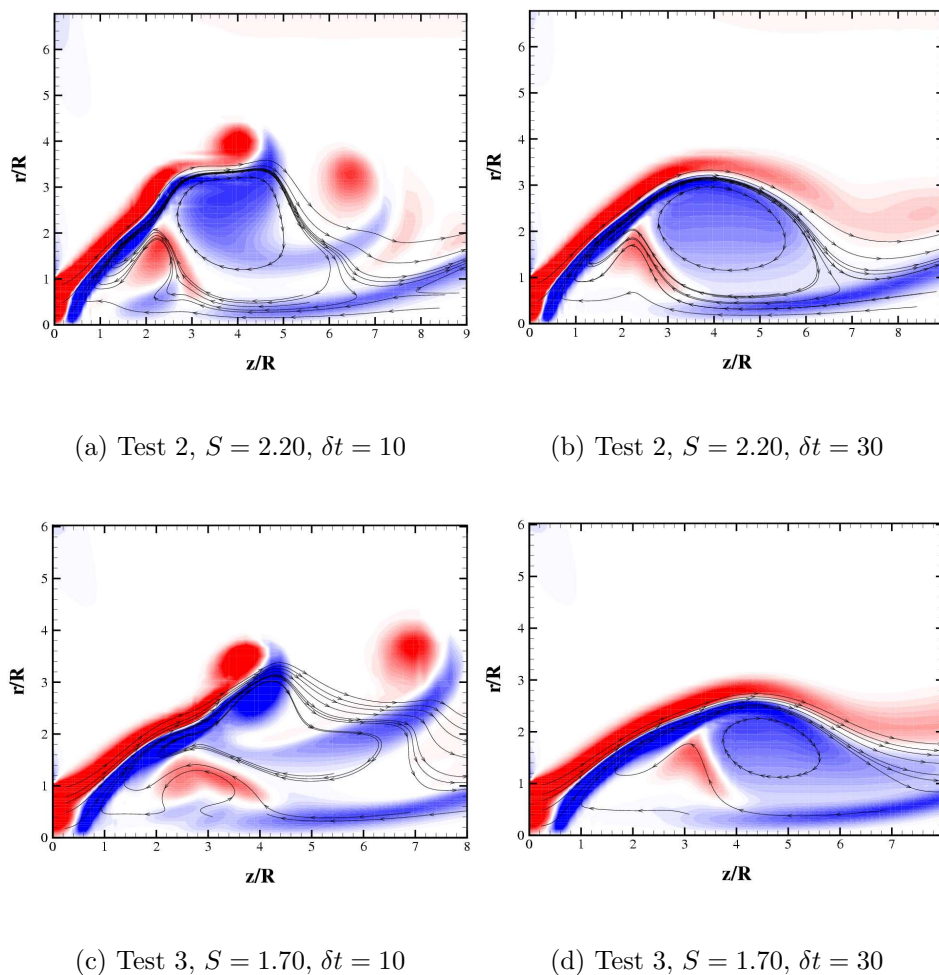
(d) Test 5, $Re = 819$, $\delta t = 30$

Figure 6.7: Flow field in the near nozzle region ten time units (left) and thirty time units (right) after the last increase in swirl ratio ($Re = 819$ for both cases). The contours show positive (blue) and negative (red) azimuthal vorticity from $-10 < \omega_\theta < 10$ and streamlines are also given for a variety of locations.
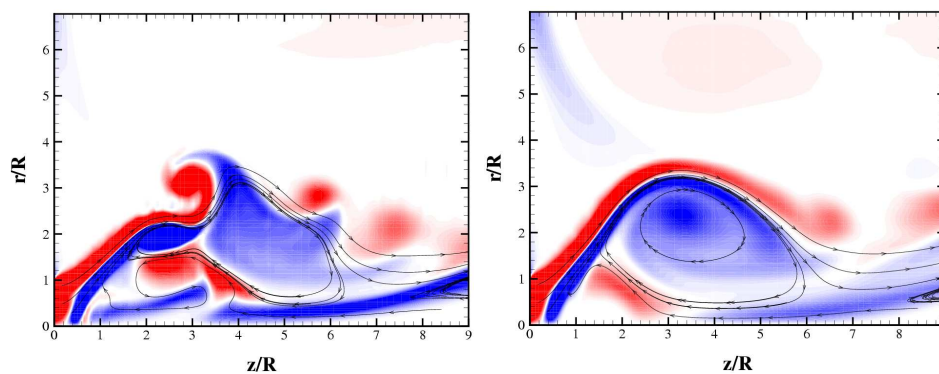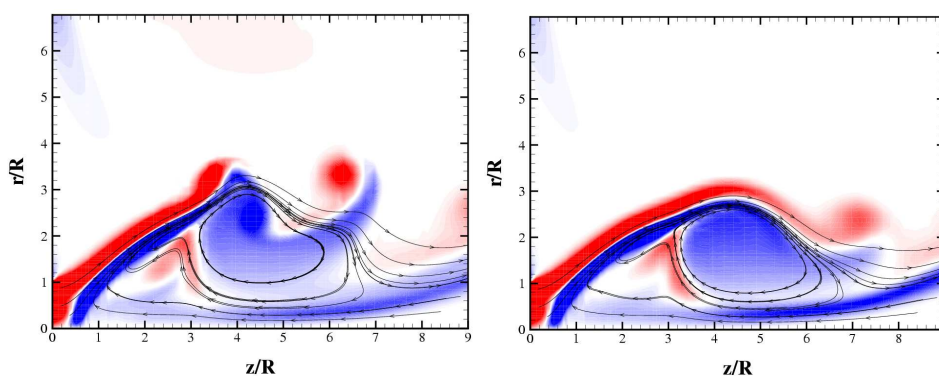
of the simulation method. Alternatively, the simulation method supplies suitable conditions to correctly simulate the critical swirl ratio.

Simulations with increasing swirl ratio and Reynolds number, from the bubble state, show that the cone-transition line does not relate to simulations where the parameters are increased in small steps and that the bubble is the preferred state at high Reynolds numbers and swirl numbers once it is attained. Evidence of meta-stability in the bubble and cone states is shown clearly here. Both the bubble and the cone can be reliably maintained as the flow state for the same parameter ranges. The state selection is clearly affected by the initial conditions.

Further research may observe the Re, S parameter space as obtained using ramped increases in swirl ratio (or Reynolds number) and the behaviour of the bubble state when the swirl ratio is decreased. Similarly, the same set of experiments can be performed on a cone-type breakdown.

Chapter 7

Conclusions

The research presented herein used an in-house spectral-element code to numerically solve the incompressible, axisymmetric, Navier-Stokes equations for an unconfined swirling jet displaying vortex breakdown. The resulting simulations gave good agreement with the equivalent experimental flows described in Billant *et al.* (1998). Comparison of the main parameter used throughout the study (the critical swirl ratio S_c) gave excellent agreement with the experimentally measured values ($\delta S_c \lesssim 3\%$) over a range of Reynolds numbers.

The study focused on the universality of a leading swirl ratio used as vortex breakdown prediction tool and also gives a limited study of vortex breakdown meta-stability. The following sections deal with each study separately.

7.1 Universality of the Critical Swirl Ratio

The criterion for vortex breakdown in swirling jets developed by Billant *et al.* (1998) shows promise in its ability to describe the criticality of the vortex

core. However, investigations presented here (see §5.2) show that the swirl ratio parameter developed by Billant *et al.* (S) is not universal for different axial velocity profiles, yielding up to 45% variation in the predicted critical swirl ratio for vortex breakdown. The measurements of the critical ratio Billant *et al.* are also based on an unusual axial velocity profile due to the contraction geometry used to create the swirling jet, leading to the question of whether the proposed swirl ratio S criterion will naturally extend to a variety of different axial velocity profiles.

In this thesis, the question of the universality of the critical swirl ratio S to a variety of velocity profiles is addressed. The profile dependency of the swirl ratio S is determined through a study of five different velocity profiles. The study examined the critical swirl ratio of vortex breakdown for a range of Reynolds numbers ($150 \lesssim Re \lesssim 1000$) and showed that the swirl ratio S provided a variation in the critical swirl ratio of $\delta S = \pm 0.35$, representing a spread of approximately 50% from the proposed critical swirl ratio of $S_c \approx 1.44$. This provided the impetus to investigate two other modified formulations of the swirl ratio, S_i and S_a, based on integrated azimuthal and integrated axial profiles, respectively; however, these were shown to have similarly large spreads in the critical swirl ratio.

An alternative parameter was developed using representative velocities, obtained through the integration of both the axial and azimuthal velocity profiles with respect to mass flow rate and angular momentum, respectively. The new swirl parameter S_* shows greatly improved universality in the critical swirl ratio prediction. The spread in critical swirl ratios was reduced to $\delta S_* = \pm 0.15$, representing a maximum of 20% variation, including the reprocessed experimental critical swirl ratios from Billant *et al.* (1998). The criterion identified from this data shows that vortex breakdown occurs for

$S_* \gtrsim 1.2$.

Further support for the new parameter S_* was provided when it was applied to another experimental study; Farokhi *et al.* (1989), whose experiments in turbulent swirling jets demonstrated that one type of jet demonstrated breakdown while another (with a different azimuthal velocity profile formulation) did not, despite both having the same swirl ratio, as calculated using the S_f parameter in §2.2.4. Application of the new swirl ratio S_* to these experimental velocity profiles shows that the swirl ratio in the two jets were indeed different. In fact, the jet that did not display breakdown had a swirl ratio $S_* = 1.27$ while the jet with vortex breakdown had $S_* = 1.37$. As the swirl ratio $S_* = 1.27$ lies at the very lower limit of the critical swirl ratios examined in the results in §5.5.5, it is consistent that this jet could not contain a breakdown region. However, a swirl ratio of $S_* = 1.37$ is well within the region shown to include breakdown for a variety of velocity profiles.

Additionally, simulations of increasing swirl ratio in the range $0 \leq S_* \leq S_{*c}$, show that the parameter S_* is constant for all downstream locations. Similar application of the swirl ratio S gives widely varying swirl ratio as a function of downstream distance. The swirl ratio S generally decreased for all downstream distances. Hence the swirl ratio developed here gives a more consistent description of the criticality of a swirling jet, independent of the location of the velocity measurements used to predict vortex breakdown further downstream.

Future research in this area could focus on providing a strong theoretical basis to a swirl parameter based on the use of fully integrated velocity parameters such as angular momentum and mass flow rate. Application of this parameter to a wider range of experimentally observed velocity profiles could also give more insight into such a critical parameter.

7.2 Vortex Breakdown State Selection

The discovery of a conical form of vortex breakdown may be attributed to Khoo *et al.* (1997), whose experiments of a tornado-like flow showed a conical expansion of the swirling jet around the centreline. A more thorough study of a conical form of breakdown was performed by Billant *et al.* (1998), where experiments of a swirling jet showed a steady conical and laminar form of vortex breakdown. Their study also observed the axisymmetric bubble seen in most vortex breakdown scenarios. The cone-type of vortex breakdown co-exists with the bubble form over the Reynolds number range tested. Their study also indicated the cone state as being dependent on the initial conditions or possibly due to azimuthal velocity perturbation, based on experiments where the axial velocity was perturbed causing the cone to disappear, to be replaced only by a bubble for favourable perturbations.

A parameter map was developed based on the procedure of starting the jet at the final Reynolds number and swirl ratio pair, from zero initial conditions. The resulting map shows that at critical swirl ratios and Reynolds numbers below $Re \lesssim 750$, the bubble-type is favoured. For $Re \gtrsim 750$ the cone-type dominates. Within the bubble dominated Reynolds number range, the cone can be observed only with greatly increased swirl ratios. The increase in swirl ratio needed to observe a cone decreased with increasing Reynolds number. Although the experiments did not start their jet at the final swirl ratio and Reynolds number, this approach numerically provided good comparison with critical swirl ratios. Observations of the flow show transience in vortex breakdown at near-critical parameters allowing the flow to fully develop before a vortex breakdown state becomes permanent.

From the parameter map developed as described above, five stable bubble states were selected for testing the transition to the cone state. From the five

bubbles, three paths with increasing swirl ratio and two paths with increasing Reynolds number were chosen such that the parameters crossed into the cone-type dominated region. For four of the tests, slow increases in swirl ratio and Reynolds number produced significant transient perturbations to the bubble, but failed to produce a cone-type breakdown, despite traversing deeply into the cone dominated region. This result shows that the cone state is easily formed in simulations when the jet is impulsively initiated, but more difficult to achieve when attempting to form a cone from a bubble state.

Possibly the formation of a cone at high swirl ratios seen in the parameter map is an artifact of the imposed initial conditions of the jet. Experiments generally observed the cone state at lower swirl ratios than the bubble. Further research in this area should map the Re, S space using ramped increases in the swirl ratio from the pre-breakdown state and also observe the effect of decreasing the swirl ratio from a bubble state. Further research could also document the effect of approaching the bubble state from a cone state.

Bibliography

AKILLI, H. & SAHIN, B. (2003). Control of Vortex Breakdown by a Coaxial Wire. *Physics of Fluids* **14(1)**, 123–133.

ALTHAUS, W., BRÜCKER, C., & M., W. (1995). Breakdown of Slender Vortices *in* Fluid Vortices. Kluwer Academic.

BENJAMIN, B. T. (1962). Theory of the Vortex Breakdown Phenomenon. *Journal of Fluid Mechanics* **14(4)**, 593–629.

BENJAMIN, B. T. (1967). Some Developments in the Theory of Vortex Breakdown. *Journal of Fluid Mechanics* **28(1)**, 65–84.

BERAN, P. (1994). Some Developments in the Theory of Vortex Breakdown. *Computers and Fluids* **23(7)**, 913–937.

BILLANT, P., CHOMAZ, J.-M., & HUERRE, P. (1998). Experimental Study of vortex breakdown in swirling jets. *Journal of Fluid Mechanics* **376**, 183–219.

BLACKBURN, H. (2002). Three-Dimensional Instability and State Selection in an Oscillatory Axisymmetric Swirling Flow. *Physics of Fluids* **14(11)**, 3983–3995.

BLACKBURN, H. & LOPEZ, J. (2002). Modulated Rotating Waves in an Enclosed Swirling Flow. *Journal of Fluid Mechanics* **465**, 33–58.

BOSSEL, H. (1969). Vortex Breakdown Flowfield. *Physics of Fluids* **12(3)**, 498–508.

BRÜCKER, C. (2002). Some Observations of Vortex Breakdown in a Confined Flow with Solid Body Rotation. *Flow, Turbulence and Combustion* **69**, 63–78.

CHAPRA, S. & CANALE, R. (1998). *Numerical Methods for Engineers.* WCB/McGraw Hill.

COGHE, A., SOLERO, G., & SCRIBANO, G. (2004). Recirculation Phenomena in a Natural Gas Swirl Combustor. *Experimental Thermal and Fluid Science* **28**, 709–714.

DARMOFAL, D. (1996). Comparisons of Experimental and Numerical Results for Axisymmetric Vortex Breakdown in Pipes. *Computers and Fluids* **25(4)**, 353–371.

DARMOFAL, D., KHAN, R., GREITZER, E., & TAN, C. (2001). Vortex Core Behaviour in Confined and Unconfined Geometries: a Quasi-one-Dimensional Model. *Journal of Fluid Mechanics* **449**, 61–84.

DENG, Q. & GURSUL, I. (1996). Effect of Leading-Edge Flaps on Vortices and Vortex Breakdown. *Journal of Aircraft* **33(6)**, 1079–1086.

DENG, Q. & GURSUL, I. (1997). Vortex Breakdown Over a Delta Wing with Oscillating Leading Edge Flaps. *Experiments in Fluids* **23**, 347–352.

ESCUDIER, M. (1984). Observations of the Flow Produced in a Cylindrical Container by a Rotating Endwall. *Experiments in Fluids* **2(4)**, 189–196.

FALER, J. & LEIBOVICH, S. (1977). Disrupted States of Vortex Flow and Vortex breakdown. *Physics of Fluids* **20(9)**, 1385–1400.

FALER, J. & LEIBOVICH, S. (1978). An Experimental Map of the Internal Structure of a Vortex Breakdown. *Journal of Fluid Mechanics* **86**, 313–335.

FAROKHI, S., TAGHAVI, R., & RICE, E. (1989). Effect of Initial Swirl Distribution on the Evolution of a Turbulent Jet. *AIAA Journal* **27(6)**, 700–706.

FERNANDEZ-FERIA, R. & ORTEGA-CASSANOVA, J. (1999). Inviscid Vortex Breakdown Models in Pipes. **50**, 698–730.

FRÄNKEL, L. (1967). On Benjamin's Theory of Conjugate Vortex Flows. *Journal of Fluid Mechanics* **28**, 85–96.

FUJIMURA, K., KOYAMA, H., & HYUN, J. (2004). An experimental Study of Vortex Breakdown in a Differentially-Rotating Cylindrical Container. *Experiments in Fluids* **36**, 399–407.

GALLAIRE, F. & CHOMAZ, J.-M. (2004). The Role of Boundary Conditions in a Simple Model of Incipient Vortex Breakdown. *Physics of Fluids* **16(2)**, 274–286.

GALLAIRE, F., ROTT, S., & CHOMAZ, J.-M. (2004). Experimental Study of a Free and Forced Swirling Jet. *Physics of Fluids* **16(8)**, 2907–2917.

GOLDSHTIK, M. & HUSSAIN, F. (1992). Stagnation Zone Theory and Vortex Breakdown. *Bulletin of the American Physics Society* **37(8)**, 1707.

GOLDSHTIK, M. & HUSSAIN, F. (1997). The nature of inviscid vortex breakdown. *Physics of Fluids* **9(2)**, 263–265.

GOLDSHTIK, M. & HUSSAIN, F. (1998a). Analysis of Inviscid Vortex Breakdown in a Semi-Infinite Pipe. *Fluid Dynamics Research* **23**, 189–234.

GOLDSHTIK, M. & HUSSAIN, F. (1998b). Inviscid Separation in Steady Planar Flows. *Fluid Dynamics Research* **23**, 235–266.

GRABOWSKI, W. & BERGER, S. (1976). Solutions of the Navier-Stokes Equations for Vortex Breakdown. *Journal of Fluid Mechanics* **75**, 525–544.

GURSUL, I. & YANG, H. (1995). On Fluctuations of Vortex Breakdown Location. *Physics of Fluids* **7(1)**, 229–231.

HALL, M. (1966). The Structure of Concentrated Vortex Cores. *Progress in Aeronautical Sciences* **7**, 53.

HALL, M. (1972). Vortex Breakdown. *Annual Review of Fluid Mechanics* **4**, 195–218.

HARVEY, J. (1962). Some Observations of the Vortex Breakdown Phenomenon. *Journal of Fluid Mechanics* **14**, 585–592.

HERRADA, M. (2003). Control of Vortex Breakdown by Temperature Gradients. *Physics of Fluids* **14**, 3468–3477.

HOURIGAN, K., GRAHAM, L., & THOMPSON, M. (1995). Spiral Streaklines in Pre-Vortex Breakdown Regions of Azisymmetric Swirling Flows. *Physics of Fluids* **7(12)**, 3126–3128.

HOURIGAN, K., THOMPSON, M., & TAN, B. (2001). Self-Sustained Oscillations in Flows around Long Blunt Plates. *Journal of Fluids Structures* **15**, 387–398.

HSU, C.-H. & LIU, C. (1992). Investigation of Vortex Breakdown on Delta Wings using Navier-Stokes Equations. *Fluid Dynamics Research* **10**, 399–408.

HUSAIN, H., SHTERN, V., & HUSSAIN, F. (2003). Control of Vortex Breakdown by Addition of Near-Axis Swirl. *Physics of Fluids* **15(2)**, 271–279.

KALKHORAN, I., SMART, M., & WANG, F. (1998). Supersonic Vortex Breakdown during VortexCylinder Interaction. *Journal of Fluid Mechanics* **369**, 351–380.

KARNIADAKIS, G., ISRAELI, M., & ORSZAG, S. (1991). High-Order Splitting Methods for Incompressible Navier Stokes Equations. *Journal of Computational Physics* **97**, 414–443.

KARNIADAKIS, G. & SHERWIN, S. (1999). *Spectral/hp Element Methods for CFD*. Oxford University Press.

KELLER, J. (1995). On the Interpretation of Vortex Breakdown. *Physics of Fluids* **7(7)**, 1695–1702.

KELLER, J., EGLI, W., & ALTHAUS, R. (1988). Vortex Breakdown as a Fundamental Element of Vortex Dynamics. *Fluid Dynamics Research* **3**, 31–42.

KHOO, B., YEO, K., LIM, D., & HE, X. (1997). Vortex Breakdown in an Unconfined Vortical Flow. *Journal of Fluid Mechanics* **238**, 1–30.

KRAUSE, E. (1985). A Contribution to the Problem of Vortex Breakdown. *Computers and Fluids* **13(3)**, 375–381.

KRAUSE, E. (1995). Computation of Flows with Vortices *in* Computational Fluid Dynamics Review. John Wiley and Sons, West Sussex, U.K.

KREYSZIG, E. (1993). *Advanced Engineering Mathematics: Seventh Edition.* John Wiley and Sons.

KUROSAKA, M., KIKUCHI, M., HIRANO, K., YUGE, T., & INOUE, H. (2003). Interchangeability of Vortex Breakdown Types. *Experiments in Fluids* **34**, 77–86.

LEIBOVICH, S. (1978). The Structure of Vortex Breakdown. *Annual Review of Fluid Mechanics* **10**, 221–246.

LEIBOVICH, S. (1984). Vortex Stability and Breakdown: Survey and Extension. *AIAA Journal* **22(9)**, 1192–1206.

LEIBOVICH, S. (1990). Large Amplitude Wavetrains and Solitary waves in Vortices. *Journal of Fluid Mechanics* **216**, 459–504.

LIANG, H. & MAXWORTHY, T. (2005). An Experimental Investigation of Swirling Jets.

LOISELEUX, T. & CHOMAZ, J.-M. (2003). Breaking of Rotational Symmetry in a Swirling Jet Experiment. *Physics of Fluids* **15(2)**, 511–523.

LUCCA-NEGRO, O. & O'DOHERTY, T. (2001). Vortex Breakdown: a Review. *Progress in Energy and Combustion Science* **27**, 431–481.

MACDONALD, D. (2003). Vortex Breakdown in a Slowly Varying Tube Impulsively Rotated about its Axis with Constant Angular Velocity. *Physics of Fluids* **15(11)**, 3490–3495.

MAGER, A. (1972). Dissipation and Breakdown of a Wing-Tip Vortex. *Journal of Fluid Mechanics* **55(4)**, 609–628.

Marques, F. & Lopez, J. (2001). Precessing of Vortex Breakdown Mode in an Enclosed Cylinder Flow. *Physics of Fluids* **13(6)**, 1679–1682.

Mary, I. (2003). Large Eddy Simulation of Vortex Breakdown Behind a Delta Wing. *International Journal of Heat and Fluid Flow* **24**, 596–605.

Maxworthy, T. (1988). Waves on Vortex Cores. *Fluid Dynamics Research* **3**, 52–62.

Menke, M. & Gursul, I. (1997). Unsteady Nature of Leading Edge Vortices. *Physics of Fluids* **9(10)**, 2960–2966.

Menke, M., Yang, H., & Gursul, I. (1999). Experiments on the Unsteady Nature of Vortex Breakdown Over Delta Wings. *Experiments in Fluids* **27**, 262–272.

Mitchell, A. & Délery, J. (2001). Research into Vortex Breakdown Control. *Progress in Aeronautical Sciences* **37**, 385–418.

Mununga, L., Hourigan, K., & Thompson, M. (2004a). Confined Flow Vortex Breakdown Control using a Small Rotating Disk. *Physics of Fluids* **16(12)**, 4750–4753.

Mununga, L., Hourigan, K., Thompson, M., & Leweke, T. (2004b). Confined of Vortex Breakdown in a Torsionally Driven Closed Cylinder by Addition of Swirl using a Small Disk. *Proceedings of the 2004 ASME Heat Transfer/Fluids Engineering Summer Conference.*

Ortega-Casanova, J. & Fernández-Feria, R. (1999). Inviscid Evolution of Incompressible Swirling Flows in Pipes: The Dependence of the Flow Structure upon the Inlet Velocity Field. *European Journal of Fluid Mechanics B/Fluids* **18**, 1067–1084.

ÖZGÖREN, M., SAHIN, B., & ROCKWELL, D. (2002). Vortex Structure on a Delta Wing at High Angle of Attack. *AIAA Journal* **40(2)**, 285–292.

PANDA, J. & MCLAUGHLIN, D. (1994). Experiments on the Instabilities of a Swirling Jet. *Physics of Fluids* **6(1)**, 263–276.

RANDALL, J. & LEIBOVICH, S. (1973). The Critical State: A Trapped Wave Model of Vortex Breakdown. *58*.

REVUELTA, A. (2004). On the Axisymmetric Vortex Breakdown of a Swirling Jet Entering a Sudden Expansion Pipe. *Physics of Fluids* **16(9)**, 3495–3498.

REYNA, L. & MENNE, S. (1988). Numerical Prediction of Flow in Slender Vortices. *Computers and Fluids* **16(3)**, 239–256.

RÖSNER, K. (1995). Rotating Flow Systems *in* Computational Fluid Dynamics Review. John Wiley and Sons, West Sussex, U.K.

RUITH, M. R., CHEN, P., & MEIBURG, E. (2004). Development of Boundary Conditions for Direct Numerical Simulations of Three-Dimensional Vortex Breakdown Phenomena in Semi-Infinite Domains. *Computers and Fluids* **33**, 1225–1250.

RUITH, M. R., CHEN, P., MEIBURG, E., & MAXWORTHY, T. (2003). Three-Dimensional Vortex Breakdown in Swirling Jets and Wakes: Direct Numerical Simulation. *Journal of Fluid Mechanics* **486**, 331–378.

RUSAK, Z. & LEE, J. (2002). The Effect of Compressibility on the Critical Swirl of Vortex Flows in Pipes. *Journal of Fluid Mechanics* **461**, 301–319.

Rusak, Z., Wang, S., & Whiting, C. (1998). The Evolution of a perturbed Vortex in a Pipe to Axisymmetric Vortex Breakdown. *Journal of Fluid Mechanics* **366**, 211–237.

Salas, M. & Kuruvila, G. (1989). Vortex Breakdown Simulation: A Circumspect Study of the Steady, Laminar, Axisymmetric Model. *Computers and Fluids* **17(1)**, 247–262.

Sarpkaya, T. (1971). On Stationary and Travelling Vortex Breakdowns. *Journal of Fluid Mechanics* **45(3)**, 545–559.

Sarpkaya, T. (1995). Turbulent Vortex Breakdown. *Physics of Fluids* **7(10)**, 2301–2303.

Schmücker, A. & Gersten, K. (1988). Vortex Breakdown and its Control on Delta Wings. *Fluid Dynamics Research* **3**, 268–272.

Shtern, V., Borissov, A., & Hussain, F. (1997). Vortex Sinks with Axial Flow: Solution and Applications. *Physics of Fluids* **A 5(9)**, 2183–2195.

Shtern, V. & Hussain, F. (1993). Hysteresis in a Swirling Jet as a Model Tornado. *Physics of Fluids* **9(10)**, 2941–2959.

Shtern, V. & Hussain, F. (1999). Collapse, Symmetry Breaking and Hysteresis in Swirling Flows. *Annual Review of Fluid Mechanics* **31**, 537–566.

Shtern, V. & Hussain, F. (2000). New Features of Swirling Jets. *Physics of Fluids* **12(11)**, 2868–2877.

SNYDER, D. & SPALL, R. (2000). Numerical Simulation of Bubble Type Vortex Breakdown within a Tube-and-vane Apparatus. *Physics of Fluids* **12(3)**, 603–608.

SOTIROPOLOUS, F., VENTIKOS, Y., & LACKEY, T. (2001). Šil'nikov's Chaos and the Devil's Staircase. *Journal of Fluid Mechanics* **444**, 257–297.

SOTIROPOLOUS, F., WEBSTER, D., & LACKEY, T. (2002). Experiments on Lagrangian Transport in Steady Vortex-Breakdown Bubbles in a Confined Swirling Flow. *Journal of Fluid Mechanics* **466**, 215–248.

SPALL, R. (1996). Transition from Spiral- to Bubble-Type Vortex Breakdown. *Physics of Fluids* **8(5)**, 1330–1332.

SPALL, R., GATSKI, T., & ASH, R. (1990). The Structure and Dynamics of Bubble-Type Vortex Breakdown. *Proceedings of the Royal Society of London A* **429**, 613–637.

SPALL, R., GATSKI, T., & GROSCH, C. (1987). A Criterion for Vortex Breakdown. *Physics of Fluids* **30(11)**, 3434–3440.

SPOHN, A., MORY, M., & HOPFINGER, E. (1998). Experiments on Vortex Breakdown in a Confined Flow Generated by a Rotating Disk. *Journal of Fluid Mechanics* **370**, 73–99.

THOMPSON, M. & HOURIGAN, K. (2003). The Sensitivity of Steady Vortex Breakdown Bubbles in Confined Cylinder Flows to Rotating Lid Misalignment. *Journal of Fluid Mechanics* **496**, 129–138.

THOMPSON, M., LEWEKE, T., & PROVANSAL, M. (2001). Kinematics and Dynamics of Sphere Wake Transition. *Journal of Fluids Structures* **15**, 575–585.

TOMBOULIDES, A. & ORSZAG, S. (2000). Numerical Inverstigation of Transitional and Weak Turbulent Flow Past a Sphere. *Journal of Fluid Mechanics* **416**, 45–73.

TROMP, J. & BERAN, P. (1997). The Role of Non-Unique Axisymmetric Solutions in 3-D Vortex Breakdown. *Physics of Fluids* **9(5)**, 992–1002.

TSITVERBLIT, N. (1993). Vortex Breakdown in a Cylindrical Container in the Light of Continuation of a Steady Solution. *Fluid Dynamics Research* **11**, 19–35.

TSITVERBLIT, N. & KIT, E. (1998). On the Onset of Unsteadiness in Confined Vortex Flows. *Fluid Dynamics Research* **23**, 125–152.

UMEMURA, A. & TOMITA, K. (2001). Rapid Flame Propagation in a Vortex Tube in Perspective of Vortex Breakdown Phenomena. *Combustion and Flame* **125**, 820–838.

VENTIKOS, Y. (2002). The Effect of Imperfections on the Emergence of three-dimensionality in Stationary Vortex Breakdown Bubbles. *Physics of Fluids* **14(3)**, L13–L16.

WANG, J., LI, Q., & LIU, J. (2003). Effects of a Vectored Trailing Edge Jet on Delta Wing Vortex Breakdown. *Experiments in Fluids* **34**, 651–654.

WANG, S. & RUSAK, Z. (1997a). The Dynamics of a Swirling Flow in a Pipe and Transition to Axisymmetric Vortex Breakdown. *Journal of Fluid Mechanics* **340**, 177–223.

WANG, S. & RUSAK, Z. (1997b). The Effect of Slight Viscosity on a Near-Critical Swirling Flow in a Pipe. *Physics of Fluids* **9(7)**, 1914–1927.